Ultrashort and coherent single-electron pulses for diffraction at ultimate resolutions

Friedrich Oscar Kirchner

München 2013

Ultrashort and coherent single-electron pulses for diffraction at ultimate resolutions

Friedrich Oscar Kirchner

Dissertation
an der Fakultät für Physik
der Ludwig–Maximilians–Universität
München

vorgelegt von
Friedrich Oscar Kirchner
aus Berlin

München, den 18. September 2013

Erstgutachter: Prof. Dr. Ferenc Krausz
Zweitgutachter: Prof. Dr. Wolfgang Zinth
Tag der mündlichen Prüfung: 7. November 2013

Contents

List of Figures

Zusammenfassung

Die zeitaufgelöste Elektronenbeugung ist eine Methode zur Untersuchung struktureller Dynamik mit einer Zeitauflösung im Femtosekunden- und einer Ortsauflösung im Sub-Ångströmbereich. Aufgrund der höheren Streuquerschnitte von Elektronen verglichen mit Röntgenstrahlung eignet sich die Elektronenbeugung besonders zur Untersuchung von dünnen Filmen, Oberflächen oder auch Gasen. Eine der Hauptschwierigkeiten der zeitaufgelösten Elektronenbeugung besteht in der Erzeugung kurzer Elektronenpulse mit hoher transversaler Kohärenz. Im Allgemeinen ist die zeitliche Auflösung der Experimente durch die Elektronenpulsdauer begrenzt, während die transversale Kohärenz die Größe der untersuchbaren Strukturen bestimmt.

Das Ziel dieser Arbeit ist es, die Grenzen der zeitaufgelösten Elektronenbeugung in Richtung einer höheren zeitlichen und räumlichen Auflösung zu verschieben. Unser Ansatz besteht in der Vermeidung aller negativen Auswirkungen der Coulomb-Abstoßung zwischen Elektronen, indem wir die Zahl der Elektronen in einem Puls auf eins reduzieren. In diesem Fall werden die longitudinalen und transversalen Geschwindigkeitsverteilungen der Elektronen allein durch den Photoemissionsprozess bestimmt. Durch die Reduktion der Elektronenquellgröße auf der Photokathode nutzen wir die schmale transversale Geschwindigkeitsverteilung der Elektronen um Elektronenpulse zu erzeugen, deren transversale Kohärenzlänge von 20 nm etwa eine Größenordnung größer ist als die in der Literatur erwähnten Werte vergleichbarer Experimente.

Die Energieverteilung von Einzelelektronenpulsen aus einer Photoemissionsquelle ergibt sich aus dem Unterschied zwischen der Photonenenergie und der Austrittsarbeit des Kathodenmaterials. Diese Überschussenergie lässt sich durch eine Anpassung der Photonenenergie an die Austrittsarbeit reduzieren. Dies demonstrieren wir unter Verwendung einer durchstimmbaren Lichtquelle im ultravioletten Spektralbereich: die erzeugten Elektronenpulse haben eine schmalere Geschwindigkeitsverteilung und folglich eine geringere Dauer.

Die Reduktion der Elektronenpulsdauer durch die Verwendung einer angepassten Photonenenergie oder anderer Methoden erfordert die Entwicklung neuer Charakterisierungstechniken für Elektronenpulse. Basierend auf der Attosekunden-Streaking-Technik entwickelten wir eine neue Methode zur Untersuchung freier Elektronenpulse. Wir analysieren den Laser-Streaking-Effekt sowohl experimentell als auch durch numerische Simulationen und zeigen, dass er sich für die Charakterisierung von Elektronenpulsen mit Dauern bis in den Sub-Femtosekundenbereich eignet. Zudem erlaubt die Methode die Bestimmung der Energiebandbreite sowie des Chirps der Elektronen.

Weiterhin entwickelten wir ein Mikrospektrometer zur Untersuchung von Elektronenbeugungsproben. Diese weisen typischerweise Dicken von einigen zehn Nanometern und Durchmesser im Bereich weniger hundert Mikrometer auf.

Abstract

Ultrafast electron diffraction is a powerful tool for studying structural dynamics with femtosecond temporal and sub-ångström spatial resolutions. It benefits from the high scattering cross-sections of electrons compared to x-rays and allows the examination of thin samples, surfaces and gases. One of the main challenges in ultrafast electron diffraction is the generation of electron pulses with a short duration and a large transverse coherence. The former limits the temporal resolution of the experiment while the latter determines the maximum size of the scattering structures that can be studied.

In this work, we strive to push the limits of electron diffraction towards higher temporal and spatial resolutions. The decisive step in our approach is to eliminate all detrimental effects caused by Coulomb repulsion between the electrons by reducing the number of electrons per pulse to one. In this situation, the electrons' longitudinal and transverse velocity distributions are determined solely by the photoemission process. By reducing the electron source size on the photocathode, we make use of the small transverse velocity spread to produce electron pulses with a transverse coherence length of 20 nm, which is about an order of magnitude larger than the reported values for comparable experiments.

The energy distribution of an ensemble of single-electron pulses from a photoemission source is directly linked to the mismatch between the photon energy and the cathode's work function. This excess energy can be reduced by using a photon energy close to the material's work function. Using a tunable source of ultraviolet pulses, we demonstrate the reduction of the velocity spread of the electrons, resulting in a shorter duration of the electron pulses.

The reduced electron pulse durations achieved by a tunable excitation or by other approaches require new characterization techniques for electron pulses. We developed a novel method for the characterization of electron pulses at energies of tens of keV which extends the attosecond streaking methodology to freely propagating electrons. We study the laser streaking effect in detail both experimentally and by numerical simulations and reveal its potential for characterizing electron pulses with durations down to the sub-femtosecond regime. In addition, the method enables the determination of the energy bandwidth and the chirp of the electrons.

Finally, we developed a microspectrometer for the characterization of samples for ultrafast electron diffraction. These samples have a typical thickness of tens of nanometers and are often only a few hundred micrometers in diameter.

1 Introduction

> Of all the instruments used by the scientist, the microscope is perhaps the one which most aptly symbolizes this profession to the non-scientist.
>
> *(Savile Bradbury, 1967)*

The invisible has always fascinated man. Thus, it is not surprising that looking at the structure of matter, which cannot be discerned by the naked eye, has been and still is a major objective of scientific research. On their way to reaching this goal researchers have made fantastic progress in shedding light onto the ever smaller building blocks of matter. Atoms are no longer the final frontier in this exploratory journey but they still offer a lot of unknown terrain.

1.1 Observing atomic motion as it unfolds

During the last century, scientists have deciphered the atomic structure of increasingly complicated materials. Starting from the first diffraction patterns of sodium chloride [1] over the reconstruction of the structure of DNA [2–4] to even more complicated structures like the membrane protein bacteriorhodopsin [5], x-ray and electron diffraction techniques have been the key to those discoveries. However, all of the mentioned examples are concerned with static structures of material in equilibrium.

Knowledge about the static structure of, for example, a biomolecule is an important first step, but it does not allow to answer the question of how a specific reaction evolves in time. But exactly this is the important question in many systems today [6, 7]. A good understanding of the intricacies of a reaction enables its control. Ultimately, the goal is to be able to design biomolecules with a specific function. This is why it is crucial to understand the dynamics, the how and why, of a transition: Static pictures of the before and after are insufficient.

Spectroscopic techniques have provided great insight into the dynamics of molecules [8, 9], but they are rather indirect. Frequently, minute differences in the conformations of a molecule influence which reaction pathway the molecule follows, and these structures are connected by radiationless transitions inaccessible by spectroscopy [6, 10]. This is why alternative techniques are required to study the transition state of a reaction and to understand how structure influences the path of a reaction and ultimately the function of a molecule. Time-resolved diffraction

techniques are ideally suited for this purpose [6, 11, 12].

A second field of research are condensed matter systems [7]. Here, the study of phase transitions, which are often of technological interest, is particularly intriguing. As in the case of molecules, understanding the structural changes that go along with macroscopic transitions will enable the design of materials with tailored properties for future applications.

The typical time-scales for chemical reactions or phase transitions in condensed matter systems are on the order of 100 fs [7]. Due to the availability of femtosecond laser systems, the required temporal resolution to resolve these processes does not pose a large problem for state-of-the-art spectroscopies, but it is still challenging for time-resolved diffraction techniques. Two complementary approaches exist, which are based on x-ray and electron pulses. Both techniques rely on triggering the dynamics of interest with an ultrashort laser pulse and having a synchronized probe pulse at a certain delay that provides information about the structural state of the sample. By varying the delay between the triggering pump pulse and the probe pulse, the dynamics of interest can be recorded in a stroboscopic fashion.

X-ray diffraction is one of the standard approaches for studying the static structure of complex molecules. It is used in many synchrotron facilities around the world, where high-intensity x-ray radiation is available. Using x-ray techniques, more than 82 000 molecular structures have been resolved to date [13]. However, obtaining time-resolved structural information with sufficient temporal resolution is more difficult (see [14] for a review of different approaches). Third-generation synchrotrons can deliver pulsed x-rays but the pulse duration is limited to 100 ps [11]. Recently, x-ray free electron lasers came into operation enabling single-shot, femtosecond x-ray diffraction studies with sufficient coherence for large biomolecules [15–21]. These large-scale facilities are expected to revolutionize time-resolved x-ray experiments [11]. On a smaller scale, high-power ultrafast laser systems based on chirped-pulse amplification enabled the development of table-top hard x-ray plasma sources suitable for time-resolved diffraction experiments with x-ray pulses as short as 100 fs [22, 23].

Compared with electrons, x-rays have scattering cross-sections that are about five to six orders of magnitude smaller [24], which means that thicker samples can be studied that would be impenetrable for electrons. On the other hand, this necessitates increasing the number of incident x-ray photons in order to obtain a diffraction pattern of good quality. In addition, the number of inelastic scattering events that happen per useful elastic one is more than three times larger for x-rays than for electrons [24]. This is further aggravated by the fact that each inelastic scattering event for x-rays deposits about 400 times as much energy as a corresponding one for electrons [24]. Consequently, sample damage is a major concern in x-ray diffraction: An ultrafast x-ray pulse from a free electron laser will typically destroy the sample, in particular in the case of delicate biomolecules. However, this does not inhibit the recording of a single shot diffraction pattern containing useful structural

information [25]. Furthermore, the small scattering cross-section of x-ray and thus large sample thickness also make it difficult to match the volume that is excited by the triggering laser pulse to the probed volume [7, 26].

Using time-resolved x-ray diffraction a large number of dynamical processes were investigated. These include photochemical reactions in solution [27, 28] and in crystals [29, 30], as well as structural dynamics in solids [22, 23, 31–34].

Electrons are best suited for studying gases, surfaces and thin crystals where their large scattering cross-section is beneficial. The need to avoid secondary scattering, which would complicate the data analysis, also makes thin or dilute samples favorable [35]. A beam of electrons can be steered by means of electric and magnetic fields and a rich selection of electron-optics is available [36]. Since electron pulses can be directly derived from femtosecond laser pulses by photoemission, it is easy to produce synchronized laser and electron pulses. Delivering short electron pulses to the sample, however, is difficult because vacuum is dispersive for electrons and Coulomb repulsion between electrons within a pulse leads to temporal broadening. In addition, the transverse coherence length of electron pulses is limited. Nevertheless, time-resolved electron diffraction is a suitable tool for studying a multitude of dynamics. These range from various chemical reactions in the gas phase [37–41] to ring-closing processes in organic single crystals [42]. In the field of condensed matter physics, research topics addressed by ultrafast electron diffraction include charge density waves in strongly correlated electron-lattice systems [43, 44], the melting dynamics in a variety of materials [45–49], and other phase transformations like insulator-to-metal transitions [50, 51].

Figure 1.1 show a schematic drawing of an ultrafast electron diffraction experiment. A femtosecond laser system provides ultrashort pulses of light. These are used directly to excite the sample and to start the dynamics of interest, but they also produce the electron pulses via photoemission. Since the two pulses, the optical pump pulse and the electron probe pulse, are derived from the same laser pulse by means of a beam splitter, they are inherently synchronized. Their delay can be varied in order to obtain structural information about the sample at various instances in time, thus creating a full characterization of the dynamic process. The electron pulse is accelerated in the static electric field between the photocathode and the anode and its propagation is controlled by electron optics. Finally, the diffracted electron beam is recorded on a detector.

Even though a time-resolution of 100 fs is sufficient to study many interesting processes in chemistry and solid-state physics, electron diffraction has the potential of going beyond the determination of atomic structure. Since an incident electron pulse scatters from electrons within the sample, it is in principle possible to study electron dynamics using ultrafast electron diffraction. Processes that could be studied using this approach include the movement of electron distributions in the breaking of a bond or the displacement of charges in the presence of an external electromagnetic field [52]. Resolving these processes requires a temporal resolution of few femtosec-

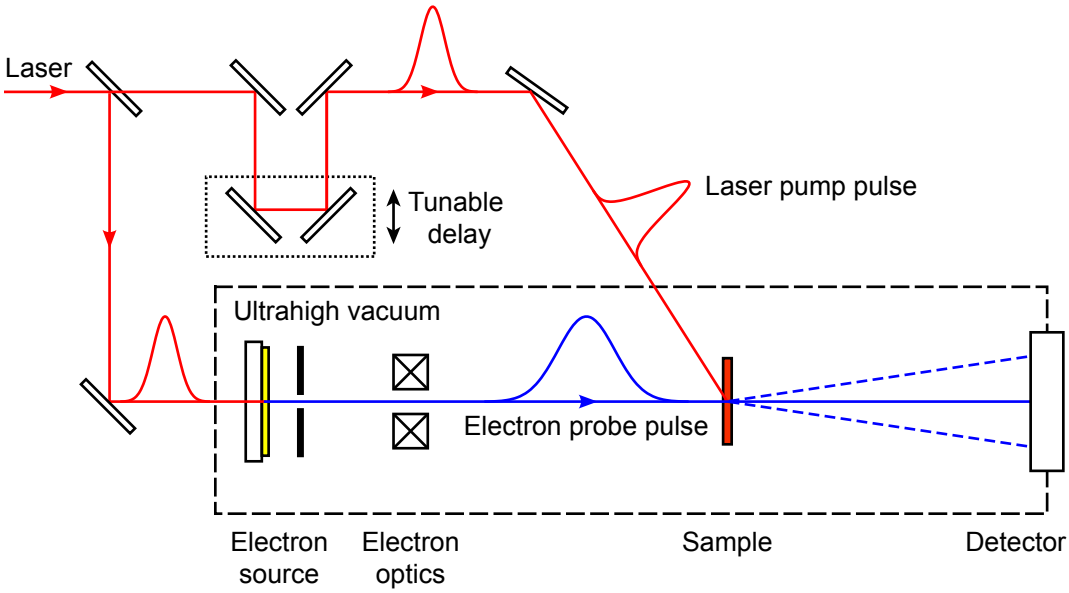

Figure 1.1: Schematic of an ultrafast electron diffraction experiment.

onds or even attoseconds. It is this exciting perspective that motivates the work in our group. Our goal is to advance electron diffraction experiments to the highest possible spatial and temporal resolutions.

1.2 Challenges of ultrafast electron diffraction

Resolving atomic motion in an ultrafast electron diffraction experiment requires a time resolution on the order of 100 fs. Such fast time-scales are routinely accessible by ultrafast lasers with pulse durations as short as few femtoseconds. However, it is not trivial to produce electron pulses of comparable shortness. The reason for this lies in two key differences between electron pulses and laser pulses.

While a laser pulse can propagate through vacuum without changing its temporal profile, vacuum is dispersive for electrons. This means that electrons at higher energies travel faster than electrons at lower energies. Strictly speaking, this is only true for sub-relativistic electrons, but electron pulses with energies of tens of keV, which are the subject of the present work, still fall into this category.

This fact has important consequences for the duration of an electron pulse. Even if an electron pulse is generated via photoemission by an ultrashort laser pulse with a duration of few femtoseconds, it will broaden in time as it propagates towards the sample because of the finite energy distribution of the electrons within the pulse. In fact, the energy bandwidth of the electron pulse is determined by the difference between the laser's photon energy and the work function of the cathode material

and by the energy bandwidth of the generating laser pulse [53], the latter being the broader the shorter the laser pulse is. It is thus in general not favorable to generated electron pulses with the shortest possible laser pulses.

An additional difference between photons and electrons is the fact that electrons are subject to Coulomb forces. Very early in the development of ultrafast electron diffraction it was realized that this can be a major problem for time-resolved experiments [54]. Coulomb forces cause electrons to repel each other and the so-called space-charge effect broadens the electron pulse both spatially and temporally in excess of the broadening caused by the pulse's original energy distribution. This severely limits the number of electrons that can be contained in a pulse with suitable quality for ultrafast electron diffraction.

Since all diffraction experiments are based on the interference of waves scattered from a spatially extended sample, the coherence properties of the scattering wave are of utmost importance. This is a major concern for electron pulses which do not have the large transverse coherence length of their x-ray counterparts generated in free electron lasers [17]. For typical time-resolved electron diffraction experiments, the reported values for the transverse coherence length are in the range of 2.5 to 3 nm for beam radii of 150 to 200 µm [53, 55]. This is sufficient for many applications in condensed-matter systems but will not be large enough for biomolecules that often have dimensions of several nanometers. Thus one of the major challenges ultrafast electron diffraction has to overcome is to increase the transverse coherence of the electron beams.

Furthermore, great care has to be taken to produce electron beams with the required spatial dimensions. Electron diffraction experiments in a transmission geometry require samples with a thickness of only tens of nanometers. In many cases, these samples cannot be produced with arbitrary dimensions and their transverse size is on the order of 100 µm [7]. This puts a constraint on the beam size of the electron beam because the whole beam should be transmitted through the sample in order to contribute to the diffraction pattern.

Finally, the characterization of femtosecond electron pulses remains challenging. Although the ponderomotive scattering technique [56–58] is widely used in the field, it requires amplified laser systems with µJ pulse energies. More importantly, it makes use of the intensity profile of a laser pulse and thus cannot be advanced easily to the envisioned electron pulse durations in the few-femtosecond or even attosecond regime.

1.3 Towards the highest spatial and temporal resolutions

The goal of this work is to advance electron diffraction towards the highest spatial and temporal resolutions. In the following a brief overview about our approach to doing so is given. Most of the topics of this section are discussed in more detail in the later chapters of this work.

As mentioned above, the Coulomb repulsion between electrons in an electron pulse has severe negative effects on the quality of the electron pulse. It broadens the temporal and spatial profile of the pulse and also worsens its transverse coherence [59]. Consequently, it is crucial to find ways to circumvent this detrimental factor. Our approach is to reduce the number of electrons in a pulse to one. This avoids any kind of space-charge effect. Of course, the overall electron flux is reduced significantly but this can be compensated for by increasing the repetition rate of the experiment, provided that the dynamics of interest are fully reversible and can be triggered a sufficiently large number of times before damage to the sample occurs.

In the single-electron regime, successive electrons will by no means have identical properties. They are still subject to statistical fluctuations in the generation process and will therefore have varying energies and trajectories. Consequently, the properties of the electron pulse, like its duration or its spatial width, can only be defined as the statistical distribution for a large number of single electrons. For example, terms like the duration of single-electron pulses do not refer to the temporal profile of an individual electron but characterize the distribution of arrival times of single electrons at a specific location.

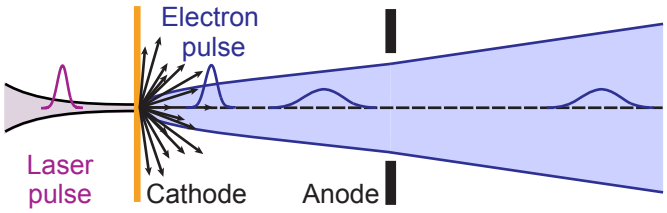

Figure 1.2: Broadening of single-electron pulses. Even without any space-charge effects, single-electron pulses broaden spatially and temporally as they propagate away from the photocathode. The broadening is caused by the electrons' initial energy and momentum spread, and it is strongest in the cathode–anode region.

In the absence of space charge, electron pulses are still subject to broadening due to their initial energy and momentum distributions [53]. This broadening mechanism is illustrated in Fig. 1.2 and has the most severe effect right after photoemission when the electrons have a low velocity and their relative velocity spread is large. This

is why we chose to use the highest possible extraction fields in our electron source and accelerate the electrons to their final velocity as quickly as possible. High-voltage vacuum breakdown is the major concern here, which is avoided by using electropolished electrodes.

In addition, it is possible to reduce the width of the energy distribution of the electrons as it is directly influenced by the mismatch between the photon energy and the work function of the cathode material during photoemission. This can be achieved by using laser pulses at a tunable wavelength matched to the photocathode's work function. At this point, the energy bandwidth of the laser pulse becomes critical, because it translates into an energy bandwidth of the electrons. At the same time, the laser pulse duration determines the initial electron pulse duration. Since laser pulse duration and bandwidth are inversely related, it is necessary to find a trade-off between the initial electron pulse duration and energy bandwidth [53]. For an accelerating field of $10\,\mathrm{kV\,mm^{-1}}$, the shortest achievable electron pulse duration is calculated to be approximately 70 fs (full width a half maximum).

As mentioned above, the sample size for many samples in transmission electron diffraction is limited to diameters of approximately 100 µm. The electron beam needs to be matched to these dimensions for maximum diffraction efficiency. Even in the absence of space-charge effects, this is not an easy feat. In the present experiment we improve the electron beam's focusability by reducing the source size on the photocathode to few micrometers.

As will be discussed below, this reduction of the source size together with the absence of space-charge in the single-electron regime results in an extraordinary coherence of the electron beam. An improvement of about an order of magnitude over the previously reported values was achieved. This makes a whole new class of (bio)molecules available for time-resolved electron diffraction studies.

As already mentioned above, the electron pulse duration from a static-field electron source cannot become arbitrarily short. Even if space-charge effects are avoided and the electron energy bandwidth is reduced, the achievable electron pulse duration is limited to approximately 100 fs. In order to reach beyond this limit our group uses an electron pulse compression technique based on time-varying electric fields. Since these experiments[1] are not the focus of the present work, they will only be briefly summarized here.

The concept of electron pulse compression is shown in Fig. 1.3. As an electron pulse propagates through vacuum, it develops a linear relationship between the relative positions of electrons within the pulse and their velocity: The fastest electrons are found at the head of the pulse while the slowest ones accumulate at its tail [54]. When the electron pulse propagates through a suitably designed time-varying electric field, this position-velocity relationship can be reversed. The leading electrons get decelerated and the trailing ones are accelerated. In the experiment,

[1] Alexander Gliserin and Matthew Walbran work on the electron pulse compression project.

an omega-shaped microwave cavity operating in the TM_{010} mode is used to provide the longitudinal electric fields that reverse the position-velocity correlations within the electron pulse. Upon further propagation, the trailing electrons, which now have a higher velocity, will catch up with the leading ones creating a temporal focus at a certain distance from the cavity. Depending on the electric fields applied in the cavity, the energy bandwidth of the electron pulse can be enlarged during the propagation through the cavity. This is the reason why a microwave cavity, in contrast to static compression approaches like reflectrons [60, 61] and magnetic chicanes [62], can be used to compress the electron pulses below their initial pulse duration determined by the generating laser pulse [63].

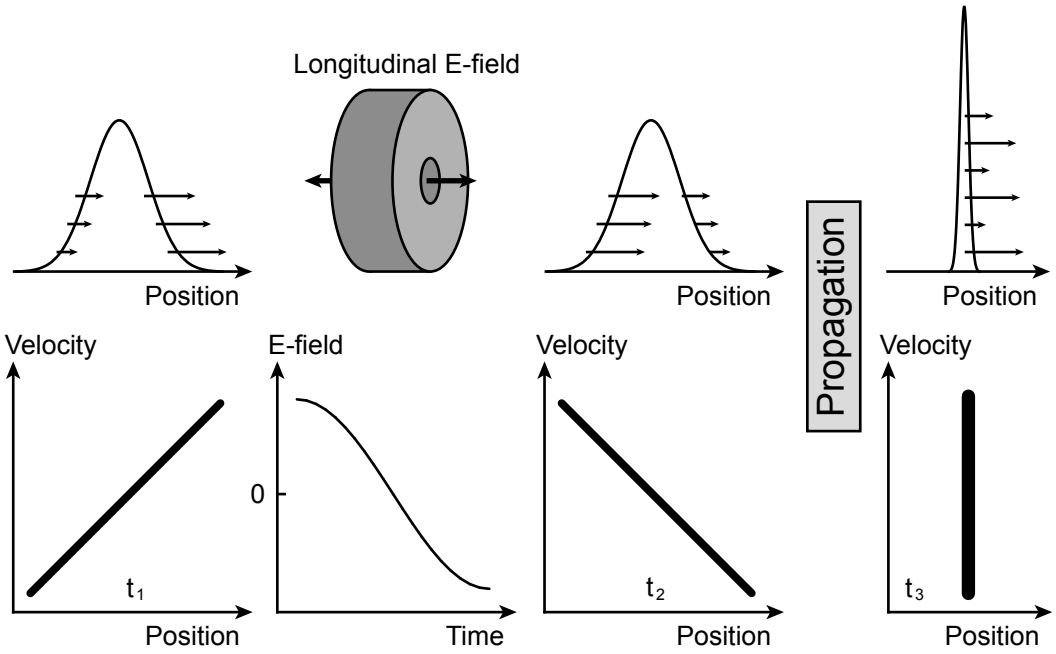

Figure 1.3: Schematic of electron pulse compression. After propagating through free space (t_1), electrons have a linear relationship between their velocity and their position within the pulse. This relationship is reversed after transmission through the time-varying, longitudinal electric field of the microwave cavity (t_2). Subsequent propagation of the pulse leads to its compression in time (t_3).

Simulations suggest that microwave compression techniques offer the potential of achieving pulse durations in the few-femtosecond to even sub-femtosecond regime [64, 65]. However, these extreme pulse durations can only be obtained with single-electron pulses. The corresponding temporal resolution may be spoiled if the electron pulses are not properly synchronized with the triggering laser pulses in a pump-probe setup. This is why, the synchronization between laser and microwave cavity

has recently become a central part of the work in our group [66].

With electron pulse compression efforts under way in laboratories around the world [63, 67–69] the characterization of electron pulses becomes increasingly important. A widely used technique relies on the ponderomotive force generated by a laser pulse [56, 57]. By using a standing wave geometry this approach has been implemented with laser pulses in the µJ-range coming from amplified laser systems [58]. The ponderomotive scattering characterization has allowed to study the spatio-temporal profile of electron pulses in great detail [68, 70] but being based on the intensity profile of a laser pulse, its time resolution is intrinsically limited to the pulse duration of the laser pulse.

In the present work, a new method for the characterization of femtosecond electron pulses is presented. It is based on the principles of attosecond streaking [71] and makes use of the acceleration of electrons by the electric field of a laser pulse. By abruptly leaving the laser's electric field during the interaction the electron gets imprinted with an energy shift corresponding to its moment of disappearance from the field. This allows the characterization of electron pulses with sub-laser cycle resolution and provides the basis for the reduction of the electron pulse duration to the sub-femtosecond regime of electron dynamics in solids.

2 Experimental setup and characterization

In this chapter, details of the setup used for ultrafast electron diffraction experiments are presented. A central aspect is the choice of a suitable wavelength of the laser light used for electron generation. In addition, procedures for the characterization of the electron beam, for finding the spatial and temporal overlap and for compensating the mismatch between electron and laser velocity are discussed.

2.1 Laser system

For electron diffraction experiments with single electrons, the low number of electrons per pulse has to be compensated by an increased experimental repetition rate. Approximately 10^6 to 10^7 electrons are required to produce a diffraction pattern of good quality. Therefore, a repetition rate in the range of few megahertz is desirable to record a diffraction image in a few seconds.

The temporal resolution required for studying structural dynamics in molecules and condensed matter systems is approximately 100 fs [7]. Producing electron pulses of this duration poses a significant challenge but does not benefit from laser pulses in the few femtosecond range. On the contrary, as discussed in Sect. 2.3, laser pulses that are too short can increase the achievable electron pulse duration because of their energy bandwidth. The laser pulse triggering the dynamics of interest is also not required to be orders of magnitude shorter than the electron pulse because it cannot improve the temporal resolution of the experiment beyond the electron pulse duration. This is why a laser pulse duration of tens of femtoseconds is sufficient for many time-resolved electron diffraction experiments.

Some dynamical processes may require a higher temporal resolution. In this case, the duration of the electron pulses can be reduced by using a microwave cavity [64], and the laser pulses for pumping the sample can be compressed by means of photonic crystal fibers [72].

2.1.1 Long-cavity laser oscillator

The laser used for all the experiments described in this work is a long-cavity titanium:sapphire oscillator (Femtosource XL, Femtolasers GmbH). The setup of the laser is shown in Fig. 2.1. It has a repetition rate of 5.1 MHz corresponding to a round-trip resonator length of approx. 60 m. This is achieved by using a Herriot cell [73] with 12 reflections per mirror. The laser operates in the positive dispersion regime and mode-locking is realized through a combination of Kerr-lensing and a

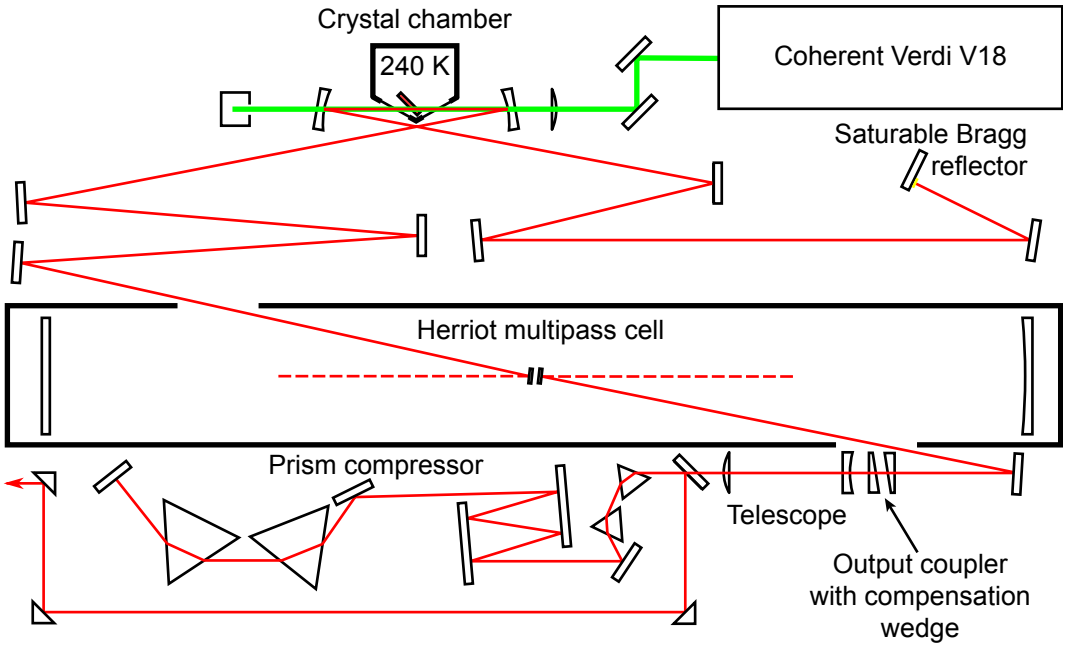

Figure 2.1: Schematic of Femtosource XL long-cavity titanium:sapphire oscillator. The long optical path length of the resonator required for a repetition rate of 5.1 MHz is achieved by means of a Herriot multipass cell [73]. The laser operates in the positive dispersion regime and the mode-locking mechanism is a combination of Kerr-lensing and a saturable Bragg reflector. The laser pulses are compressed in a prism-compressor.

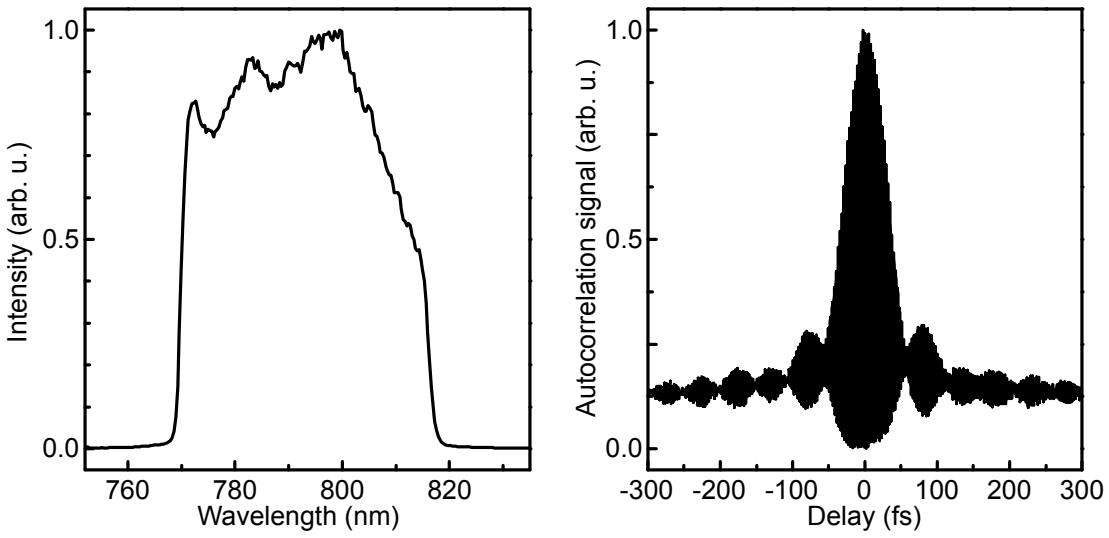

(a) Spectrum **(b)** Autocorrelation

Figure 2.2: Properties of laser pulses from Femtosource XL. The spectrum of the pulses spans a wavelength range from about 770 to 820 nm. The pulse duration is approximately 50 fs as evidenced by the autocorrelation trace. The autocorrelation shows a small amount of uncompensated third-order dispersion, originating from the prism compressor.

saturable Bragg reflector [74]. After compression in a prism compressor, the laser pulses have an energy of about 500 nJ and a duration of approximately 50 fs. The laser spectrum ranges from approximately 770 nm to 820 nm (Fig. 2.2).

2.1.2 Alignment system

Due to the long laser beam paths in the laboratory a beam stabilization system was installed (Aligna 4D, TEM Messtechnik GmbH). The position and the direction of the laser beam are monitored with two position sensitive detectors, and fluctuations are compensated using a pair of motorized mirror mounts with additional piezo actuators for fast feedback.

2.1.3 Control of the experimental repetition rate

As stated above, an experimental repetition rate in the megahertz range is desirable for electron diffraction experiments with single electrons. Unfortunately, repetition rates this high may not be feasible due to additional experimental constraints. The most important one is sample damage caused by the laser pump pulses. While investigating suitable sample materials for the experiments discussed in Chapt. 5

we found that the various metal films we studied were destroyed by the average energy deposited in the film and not by the energy contained in an individual laser pulse. For the experiments discussed below as well as many time-resolved diffraction studies, one would like the pulse energy of the triggering laser pulses to be as high as possible in order to maximize the effect in the sample. Consequently, the average deposited energy has to be reduced while maintaining the pulse energy. This can only be achieved by reducing the repetition rate of the laser. The reduction in electron flux has to be compensated for by increasing the acquisition time of a diffraction pattern or by increasing the number of electrons per pulse. The latter is of course not an option when the highest possible time resolutions are required.

The second reason for reducing the experimental repetition rate is the relaxation time of the sample. When studying structural dynamics in the multi-shot regime, i. e. accumulating many electron pulses to form a diffraction pattern, it has to be ensured that the experimental conditions for each pump-probe cycle are identical. In particular, the sample has to relax back to its ground state before the arrival of the next laser pulse. Depending on the sample and the dynamics under investigation, a reduction of the experimental repetition rate below the megahertz level may thus be required.

In order to reduce the repetition rate of our laser, a pulse picker was implemented. It consists of an RTP Pockels cell (RTP-5-20-AR650-1000, Leysop Ltd.) and driver electronics from Bergmann Meßgeräte Entwicklung KG. For maximum flexibility in the choice of repetition rates the pulse picker can operate at repetition rates up to 2.6 MHz corresponding to picking every second pulse from the laser pulse train. The typical suppression ratio between the suppressed and transmitted laser pulses is approximately 1 : 50. This determines the lowest usable repetition rate. At a repetition rate of approximately 100 kHz, the average power contained in the suppressed pulses is equal to the average power of the desired pulses. Lower repetition rates can still be used, particularly if the undesired pulses are further suppressed by a nonlinear optical process. In fact, this situation is often realized because a photoelectron cannot be generated from our gold cathodes by a single laser photon at 800 nm and because the diffraction samples are frequently excited by the second harmonic of the laser.

2.2 Electron diffraction apparatus

2.2.1 Overview

The electron diffraction apparatus consists of three parts, the electron source, the main experimental chamber and the electron detection system. All parts operate under ultrahigh vacuum conditions at pressures down to 10^{-9} mbar. A pressure this low is not required for the generation of electrons, but it is beneficial for the stability

of the electron source. In addition, a low pressure reduces the number of detrimental overlayers that accumulate on the surface of the diffraction sample. The electron source chamber and the main experimental chamber are equipped with turbomolecular pumps (Pfeiffer Vacuum GmbH), the detector chamber is pumped through the main chamber. The three parts of the experiment are connected by vacuum gate valves (Trinos Vakuum-Systeme GmbH) and can thus be vented individually, for example when the sample needs to be exchanged in the main experimental chamber. The main chamber has a semispherical shape with a diameter of approximately 45 cm. The other parts of the experiment are considerably smaller. The whole apparatus is made from stainless steel.

The electron diffraction apparatus described below was conceived, designed and built by Peter Baum, Alexander Gliserin, Friedrich Kirchner and Stefan Lahme. Friedrich Kirchner was responsible for the optical design of the experiment, and Stefan Lahme contributed most significantly to the current design of the electron source with an improved high voltage stability and a water-cooled magnetic lens with deflection coils.

2.2.2 Electron source

The electron source consists of a cathode assembly holding the photocathode and an opposing anode with a hole. The generated electrons are accelerated towards the anode and propagate through the anode hole. They then enter a magnetic solenoid lens which is used to collimate or focus the beam. Two pairs of smaller coils are located after the magnetic lens. They can be used to steer the electron beam which propagates towards the sample region and the detector.

Mechanics and electric field distribution

A cut through the cathode and anode construction is shown in Fig. 2.3. The laser enters from the left and is focused onto the photocathode mounted at the right side of the cathode assembly. The photocathode itself is a transparent sapphire or quartz substrate (thickness 1 mm, diameter 12.7 mm) coated with few nanometers of chromium for adhesion and some 20 nanometers of gold for the generation of electrons. It is glued into a cylindrical holder by means of conducting silver paste which also provides the electrical contact. The cylindrical part also contains the focusing lens and is screwed into the base of the cathode assembly. It can be conveniently removed from the vacuum chamber by opening a single 40CF flange. Thus, a routine procedure like exchanging the photocathode does not require the electron source to be dismantled completely, reducing the service time from hours to minutes.

The anode is a disk with a central hole (diameter 2 mm) which is parallel to the cathode surface. The cathode assembly and the anode are made of oxygen-free copper for compatibility with ultra-high vacuum. The anode and the cathode assembly

are connected by spacers made from glass ceramics (Vitronit, Vitron Spezialwerkstoffe GmbH). By using spacers of different lengths the distance between cathode and anode can be varied. This allows the accelerating field to be adjusted.

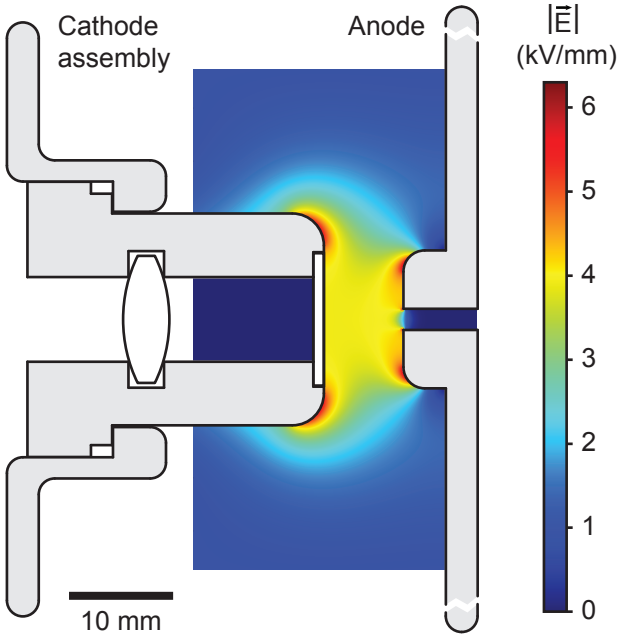

Figure 2.3: Cut through the electron gun. It consists of a cathode assembly with focusing lens and photocathode and the opposing anode. The electric field distribution is plotted for a cathode–anode spacing of 8 mm and an acceleration voltage of 30 kV.

In addition to the mechanical construction, Fig. 2.3 shows the electric field distribution in the cathode–anode region. It was calculated for a distance of 8 mm separating cathode and anode and an accelerating voltage of 30 kV. The anode is grounded and the cathode is connected to a highly-stable high voltage power supply (PNChp+60000–1neg, Heinzinger electronic GmbH). Along the central axis of the cathode–anode region, the accelerating field is very homogeneous. The reduction of the field at the anode hole is discussed in detail in Sect. 2.4.1.

In order to reach the shortest electron pulse durations the accelerating field has to be maximized [7]. This reduces the effect of the electron energy distribution on the pulse duration, because the time of a high relative velocity spread is shortened. A practical limit for the maximum static electric field strength that can be achieved without vacuum breakdown is approximately $10\,\mathrm{kV\,mm^{-1}}$ [7]. In order to reach this value the cathode–anode distance was reduced to 6 mm for an accelerating voltage of 60 kV. In the first stages of the experiments this configuration led to massive problems with arcing. These problems were overcome by electropolishing the copper

parts of cathode and anode and by replacing the glass ceramics spacers by ones made from polyimide (Tecasint 2011, Ensinger GmbH). In addition, the detrimental effects of strong vacuum breakdowns were reduced by placing a 2 GΩ-resistor (Heinzinger electronic GmbH), which limits the electric current flowing during the breakdown, in-line between power supply and cathode. After these improvements, it was possible to operate the electron source at 55 kV for extended periods of time without vacuum breakdowns.

Optics

Many samples of interest for time-resolved electron diffraction experiments can only be produced with very limited sizes [7]. Diameters of 100 µm are common. For optimal diffraction efficiency, the electron beam must not be larger than the sample size. Thus, an electron beam with a diameter of about 100 µm at the sample has to be produced. In the present experimental setup, a magnetic solenoid lens is used to focus the electron beam. Because of the random nature of the emission process at the photocathode, i. e. no correlation between the location of the photoemission within the focal spot of the laser and the electron momentum, the achievable spot size of the focused electron beam depends on the size of the source. Consequently, the source size of the electron beam and thus the focus diameter of the laser has to be reduced. As will be discussed in Chapt. 4 a small source size is also beneficial for the transverse coherence length of the electron beam.

In order to produce a small focus on the photocathode, a large numerical aperture is required. This can be realized by using a lens with a large diameter (and a correspondingly large beam) outside of the vacuum chamber. Due to tight spatial constraints, a different approach is taken in the present work. A lens with a diameter of 12 mm and a focal length of 20 mm is placed within the vacuum system directly in front of the photocathode (Fig. 2.3). Thus, a beam with a diameter of few millimeters can be sent into the vacuum chamber.

Since the lens position is fixed within the cathode assembly, it cannot be adjusted to compensate for changes in the incident beam's wavelength or divergence, both of which shift the focus position. For this reason, an additional lens was added outside of the vacuum chamber (Fig. 2.4). By shifting this lens it is possible to optimize the focus on the photocathode. Figure 2.5 shows the calculated beam waist on the photocathode for the situation depicted in Fig. 2.4 for two different laser wavelengths and a variable distance d_1 between the two lenses. The calculation assumes a collimated Gaussian beam with a beam waist of 1.5 mm incident on lens 1 ($f_1 = 400\,\mathrm{mm}$) and focused onto the photocathode by lens 2 ($f_2 = 20\,\mathrm{mm}$). It takes into account the wavelength-dependent refractive indices of the fused silica lenses and the sapphire substrate of the photocathode. By changing the position of the first lens, it is possible to optimize the focus on the photocathode for different wavelengths. Similarly, changes in the incident beam's divergence can be compen-

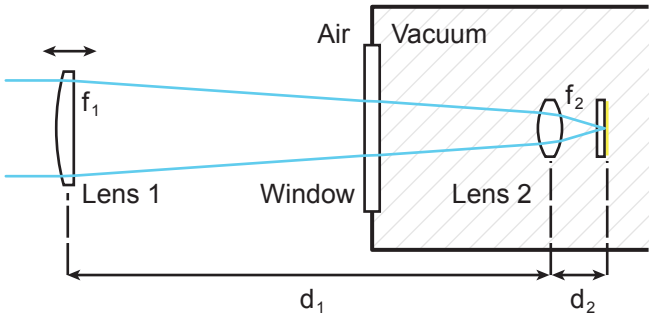

Figure 2.4: Focusing on the photocathode. In order to obtain a tight focus on the photocathode, a lens with a short focal length is placed at a fixed location within the vacuum system close to the cathode. Fine-tuning of the focus position can be achieved by translating a second lens outside of the vacuum chamber.

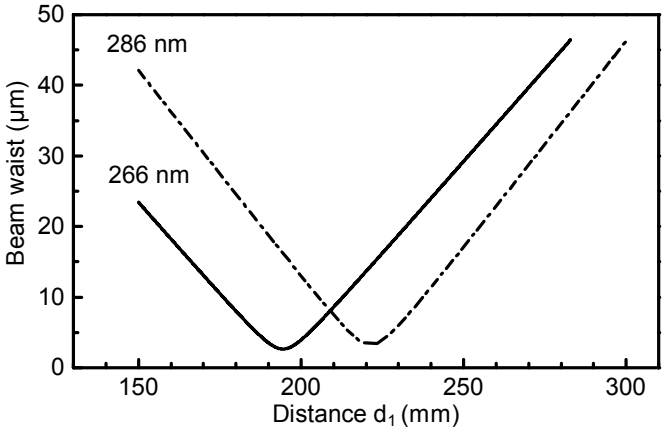

Figure 2.5: Focus optimization on the photocathode. Calculated beam waist on the photocathode for two different laser wavelengths as a function of the distance d_1 between lens 1 ($f_1 = 400\,\mathrm{mm}$) and lens 2 ($f_2 = 20\,\mathrm{mm}$).

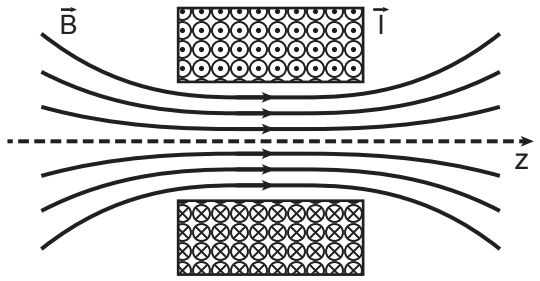

Figure 2.6:
Schematic drawing of the magnetic field of a solenoid. As long as the electron propagates parallel to the magnetic field lines it does not experience a Lorentz force. However, in the entrance and the exit regions of the solenoid, the radial magnetic field components accelerate the electron azimuthally. This azimuthal velocity component is responsible for the focussing effect of the solenoid lens.

sated. The calculated minimum beam waists on the photocathode are 2.7 µm for $\lambda = 266\,\text{nm}$ and 3.3 µm for $\lambda = 286\,\text{nm}$. In summary, using the depicted optical design a tight focus well below 10 µm can be obtained for realistic incident beams.

Magnetic lens and deflection coils

The electron beam coming from the photocathode is divergent and expands to a diameter of several millimeters on the detector. This, of course, makes it impossible to obtain a reasonable diffraction pattern because the Bragg spots will severely overlap. In addition, the electron beam also has a typical diameter of approximately 2 mm at the sample position. Most samples, however, cannot be produced in such sizes. Because of these two reasons it is necessary to collimate or even focus the electron beam after the acceleration region.

A solenoid magnetic lens within the vacuum chamber is used for this purpose. It consists of a solenoid centered around the design axis of the electron diffraction apparatus. When an electric current flows through the windings of the magnetic lens, the rotationally symmetric magnetic field shown schematically in Fig. 2.6 focuses the electron beam.

An electron with charge $-e$ and velocity $\vec{v}$ interacts with the magnetic field $\vec{B}$ through the Lorentz force

$$\vec{F} = (-e)\vec{v} \times \vec{B}. \tag{2.1}$$

As it travels along the symmetry axis of the solenoid, the electron does not experience any force because its velocity vector $\vec{v}$ is parallel to the magnetic field $\vec{B}$. However, when the electron is only slightly off-center it experiences a force in the entrance and exit regions of the solenoid where the radial components of the magnetic field lead to an azimuthal acceleration of the electron. This azimuthal velocity component together with the axial component of the magnetic field then causes the electron to be accelerated towards the symmetry axis of the solenoid, creating the focusing effect.

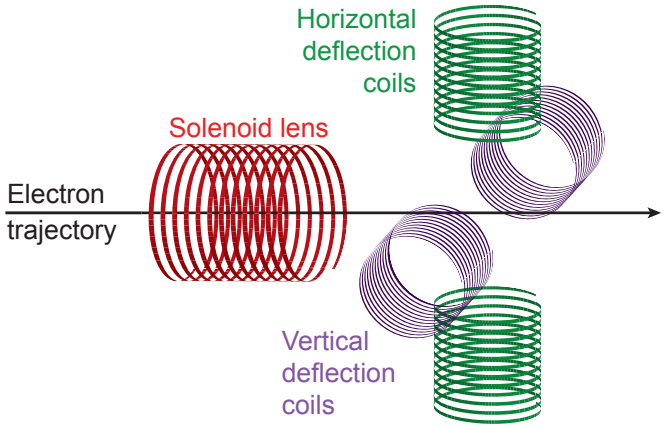

Figure 2.7: Magnetic lens and deflection coils. The electron beam passes through the solenoid lens (red) and can be steered by two pairs of magnetic coils in a Helmholtz-like configuration (green and purple).

The focal length of a solenoid lens in the thin lens approximation, i. e. when the lens thickness is much smaller than the focal length of the lens, for electrons propagating in the vicinity of the central axis is

$$f = \frac{4}{\int \mathrm{d}z \left(eB_z/mv_l\right)^2} = \frac{8mU}{e\int B_z^2 \mathrm{d}z}. \tag{2.2}$$

Here, v_l is the longitudinal velocity of the electron caused by the acceleration voltage U [75, 76]. B_z is the longitudinal component of the magnetic field on the axis of the solenoid. The integration of B_z in Eq. (2.2) in principle goes from negative to positive infinity, but the magnetic field outside of the lens vanishes quickly. The exact calculation of the magnetic field for the realistic solenoid requires the summation over all the wire loops forming the solenoid [77, 78], but the magnetic field is always proportional to the current I flowing through the wire. Thus, the focal length of the lens can be adjusted easily by varying I.

Downstream of the magnetic solenoid lens, two pairs of smaller solenoids were installed in a Helmholtz-like geometry. The magnetic fields produced by these coils can be used to steer the electron beam horizontally and vertically. This can be useful during alignment procedures, e. g. to align the unfocused and the focused electron beams with respect to each other. The magnetic lens assembly including the deflecting coil pairs is shown in Fig. 2.7.

Due to resistive heating in the wire of the magnetic lens the mechanical construction heats up significantly. In the first design of the magnetic lens this caused a shift in the lens position due to thermal expansion of the supporting mechanical parts. In the current design, the magnetic lens assembly is water-cooled and thermal drifts are no longer an issue.

2.2.3 Sample manipulation

In order to obtain a diffraction pattern from a crystalline material, the sample has to be properly oriented with respect to the incident electron beam. Thus, the possibility of rotating the sample around a horizontal and a vertical axis has to be provided. In addition, the sample has to be positioned in the electron beam. This requires linear translations along the three Cartesian axes. These five translations are provided by a five-axis positioning system (Huber Diffraktionstechnik GmbH & Co. KG) within the vacuum system. It consists of a horizontal XY linear translation stage with a range of ±25 mm, a vertical Z linear translation stage with a range of 25 mm, a goniometer stage with a range of ±10° and finally a rotation stage. All stages are equipped with step motors and can be controlled by a computer program.

The sample holder containing the sample is connected to the positioning system by means of home-built connector allowing precise repositioning and easy installation and removal. In order to exchange the sample the vacuum in the chamber has to be broken. The sample can then be removed and installed through a 100CF viewport.

2.2.4 Sample excitation

The sample under investigation is located in the center of the hemispherical vacuum chamber. In order to deliver the laser pulses triggering the dynamics of interest to the sample the setup depicted in Fig. 2.8 is used. The laser beam, which can be the fundamental or the second harmonic of the titanium:sapphire laser, is enlarged by a Galilean telescope (focal lengths −75 mm and 400 mm) and focused into the vacuum chamber by a lens with a diameter of 50.8 mm and a focal length of 500 mm. Despite the large distance to the sample, this provides a focal spot of approximately 25 µm (full width at half maximum) on the sample, which can be matched to the electron beam size by defocusing. Within the vacuum chamber the laser beam follows a z-shaped path and is reflected onto the sample by a broadband dielectric mirror. The part of the laser beam that is not blocked by the sample leaves the vacuum chamber after reflection on a second mirror. It can be used for various diagnostic tasks, e. g. the alignment of the laser on the sample. The location of the laser focus on the longitudinal axis can be adjusted by translating the last lens before the vacuum system. Its transverse position can be controlled by the last mirror before the vacuum chamber. Access to the beam-steering mirrors within the vacuum chamber is not required.

2.2.5 Sample observation

Having visual access to the inside of the vacuum chamber proved very valuable during our experiments. For reasons of practicability and laser safety, a camera-based system was developed to view the sample region. This camera system had

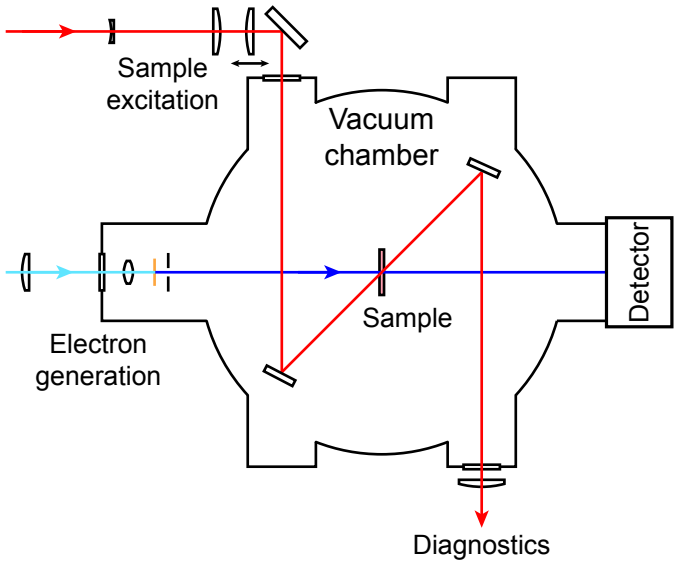

Figure 2.8: Schematic of laser beam path for sample excitation (top view). The exciting laser runs through a telescope to widen the beam and is focused onto the sample by a lens outside of the vacuum system. It follows a z-shaped path through the vacuum chamber. The transmitted part of the beam can be used for diagnostics.

to be outside of the vacuum chamber and had to use the available viewports. The following features were desired:

1. coarse overview over the top part of the sample positioning system in order to position the sample,
2. close-up view of the sample with high resolution,
3. variable aperture and exposure time,
4. continuous image acquisition (video),
5. ability to save images.

These requirements are satisfied by a combination of two cameras and lenses. We use a monochrome CCD camera to image the sample and its surroundings. It is equipped with a C-mount lens (Soligor TV lens 25 mm F/1.4 with extension ring for close focus capability) and delivers an analog video signal which we digitize with a conventional video capture card. This camera is positioned such that it views the sample region from a 45° angle above and towards the electron beam direction.

In order to obtain the desired close-up image of the sample we use a dedicated macro lens (Tamron SP AF 180 mm F/3.5 Di LD (IF) Macro 1:1, model: B01N). This lens was chosen because of its large working distance[1] of 25 cm at a magnifi-

[1]The working distance is the distance between the object and the front of the lens at maximum magnification.

cation of 1:1. In addition, it is designed to illuminate the full frame ($36 \times 24\,\mathrm{mm}^2$) of a digital photo camera such that we only use the central part of the projected image which has the highest quality. The Nikon-mount version of this lens has the added benefit of a manually adjustable aperture. The lens was combined with a high-resolution color C-mount camera (Daheng DHHV3151UC-ML) with a sensor size of approximately $6.4 \times 4.8\,\mathrm{mm}^2$ and a resolution of 2048×1536 pixels. The lens and the camera are joined by a commercial adapter (HAMA article no. 31602) which we modified such that it can hold filters with a diameter of 25.4 mm. The camera and lens are located at a 45° angle above the electron beam looking along the beam path. In order to obtain the maximum magnification the lens is operated close to its minimum focus distance. This makes it necessary to place the lens in a special ultrahigh vacuum tube with a 40CF viewport intruding into the vacuum chamber. Both cameras are equipped with custom-made LED ring-lights located along the edge of the 40CF viewports and providing an even white-light illumination of the inside of the chamber.

The close-up camera system is capable of imaging an area on the sample of about $6.4 \times 4.8\,\mathrm{mm}^2$ and can resolve features with a size of approximately 10 µm. It is used to find the overlap between electron and laser beams. We also used it successfully to optimize the laser overlap with the sample by maximizing the fluorescence from the sample. Here, a filter inserted in the adapter between lens and camera that blocked the laser light but transmitted the fluorescence proved useful.

2.2.6 Electron detector

The detector used in the electron diffraction apparatus is a CMOS camera equipped with a scintillator (TemCam-F416, Tietz Video and Image Processing Systems GmbH). The scintillator is coated onto a fiber optic plate which connects directly to the CMOS chip. It is equipped with a coating to protect it from stray light in the vacuum chamber.

The electron detector has a field of view of $64 \times 64\,\mathrm{mm}^2$ which allows a large number of diffraction peaks to be recorded simultaneously. The pixel size is $15.6 \times 15.6\,\mu\mathrm{m}^2$ and the detector has a resolution of 4096×4096 pixels. Furthermore, the detector provides single-electron sensitivity. It is capable of exposure times from 100 ms to 30 s and is fully integrated in the computer program which is used to control the time-resolved experiments and to acquire the experimental data.

Point spread function

The experiments presented in this work frequently require the determination of an electron beam radius. Electron beam profile data can be obtained directly from the CMOS detector. However, there may be discrepancies between the measured profile and the actual beam profile of the electron beam. This is because a single electron

impinging on the scintillator does not produce a response in just a single pixel of the detector. Instead, several pixels record some counts. The count distribution across neighboring pixels for a single incident electron is called point spread function. It is shown in Fig. 2.9 for an electron energy of 40 keV. The point spread function is fitted

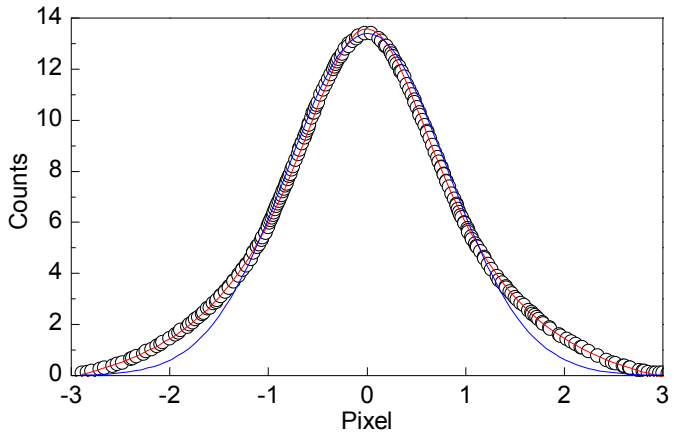

Figure 2.9: Point spread function of the CMOS detector for an electron energy of 40 keV. The data is fitted using a Gaussian function (blue) and a Lorentzian function (red). Data provided by Tietz Video and Image Processing Systems GmbH.

using a Gaussian function. This results in a width of $\sigma_{PSF} = (0.806 \pm 0.004)$ pixel (standard deviation). However, the data is not well described by a Gaussian function (see Fig. 2.9). Instead, it can be fitted much better with a Lorentzian function of the form

$$counts(x) = c_{offset} + (2A/\pi) \cdot (w/(4x^2 + w^2)), \tag{2.3}$$

where the offset $c_{offset} = -1.56 \pm 0.02$, $w = 1.990 \pm 0.006$, and $A = 47.3 \pm 0.2$. We set $counts = 0$ where it would be negative according to the formula and obtain a very good agreement between data and fit.

In the experiments, we routinely perform Gaussian fits in order to characterize the electron beam profile. To eliminate the effect of the point spread function we would like to deconvolve the data using the simple formula for the deconvolution of two Gaussians,

$$\sigma_{real} = \sqrt{\sigma^2_{measured} - \sigma^2_{PSF}}. \tag{2.4}$$

Considering that the point spread function is not Gaussian in the present case, this formula leads to erroneous results. In order to estimate the size of the error caused by using Eq. (2.4) with the value of σ_{PSF} determined above, we calculate the broadening of Gaussian profiles of various widths by convolving them with the point spread function according to Eq. (2.3). This data corresponds to what is measured

in the experiment. It is thus fitted using a Gaussian function, and an estimate for the width of the original distribution is calculated using Eq. (2.4). We then calculate the relative error of the retrieved width with respect to the real width that was chosen originally. The result is shown in Fig. 2.10. The relative error between the real and

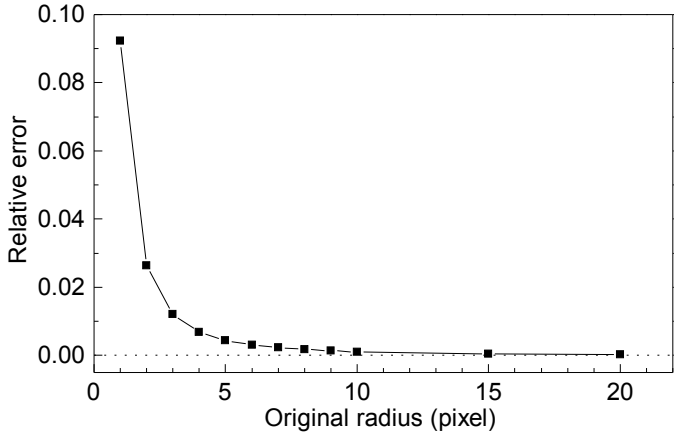

Figure 2.10: Deconvolution error, point spread function

the retrieved widths drops from 9% at a real radius of 1 pixel to 1% at a radius of 3 pixel. Above a radius of 10 pixel, the relative error drops below 0.1%. Since the beam radii measured in the experiments are typically above 3 pixel, the error of 1% or less is acceptable. It is thus suitable to use Eq. (2.4) with $\sigma_{PSF} = 0.806$ pixel in order to eliminate the effect of the point spread function of the detector. Although the point spread function of the detector most likely depends on the electron energy, we do not expect any major differences between 40 keV and 30 keV, which is a typical electron energy for the experiments discussed in the present work.

2.3 Generation of electron pulses: influence of the photon energy[2]

The generation of electron pulses in the presented experiments is based on the familiar photoeffect. A laser photon may emit an electron from the photocathode, if the laser photon energy is above the work function of the cathode material. The process of photoemission from a metal cathode can be described in a three-step model [80]: In the first step, a photon is absorbed by an electron within the cathode. In the second step, the excited electron migrates towards the surface of the metal undergoing elastic and inelastic scattering on its way. Finally, in the third step,

[2]The experiments discussed in this section were performed as part of the Bachelor's thesis of Monika Aidelsburger [79].

those electrons that still have an energy above the work function of the material may escape into vacuum.

Metal photocathodes typically have work functions of several electronvolts. This means that a single photon at a wavelength of 800 nm is insufficient for producing a photoelectron. Consequently, electrons have to be generated by either a multiphoton process or by photons with higher energy. Experiments supporting this view have been performed on gold photocathodes with the fundamental, the second and the third harmonic of femtosecond laser pulses from a titanium:sapphire laser [81].

Using laser pulses with a multiple of the original photon energy in order to exceed the work function of the material may leave a large discrepancy between the two involved energies. This energy mismatch, the so-called excess energy, is imprinted in the electron as a kinetic energy. Due to the scattering that occurs as the electron propagates towards the surface of the photocathode prior to its emission, the electron pulses have a broad energy and momentum distribution rather than a distinct energy and direction. The width of the distribution is determined by the excess energy.

The longitudinal momentum distribution of the electrons within an electron pulse results in a temporal broadening of the pulse as it propagates towards the sample. The transverse momentum distribution causes a spatial broadening of the pulse. In addition to this spatial effect, the transverse momentum spread of an electron beam is inversely proportional to the transverse coherence length of the beam. This is discussed in more detail in Chapt. 4. Because of these two reasons, electron pulse duration and transverse coherence, it is important to reduce the excess energy of the electrons in the photoelectric generation process. This can be achieved by using laser pulses with a photon energy matched to the work function of the cathode material. The latter is typically in the few-electronvolt range, so ultraviolet light is required.

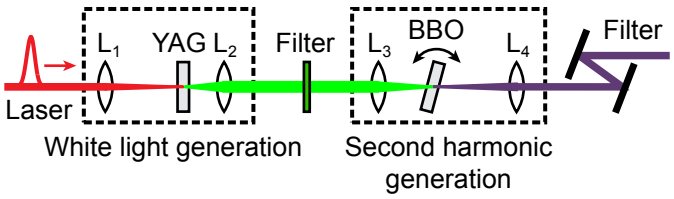

Figure 2.11: Generation of tunable ultraviolet laser pulses. Femtosecond laser pulses at a wavelength of 800 nm are focused into a YAG crystal. The resulting white light is selectively frequency doubled in a BBO crystal. The wavelength of the produced ultraviolet radiation can be tuned by tilting the BBO crystal. Filters are used to remove undesired spectral components.

In order to produce tunable laser pulses in the ultraviolet spectral range, the setup depicted in Fig. 2.11 is used. Approximately a quarter of the power of our laser oscillator (see Sect. 2.1) is focused into an yttrium/aluminum garnet (YAG) crystal

for broadband continuum generation [82]. The remaining laser power is available for pumping the sample in a pump-probe experiment. The generated white light extends to below 480 nm (Fig. 2.12, top panel). Since we are only interested in the wavelength range up to about 700 nm, we use a filter to block the fundamental light at 800 nm. The transmitted light is focused into a β-barium-borate (BBO) crystal for second harmonic generation. The thickness of the BBO crystal is 100 µm. This is too large to support the entire bandwidth of the light but it allows to tune the output of the second harmonic generation in the range from 240 to 350 nm by tilting the BBO crystal in the range of $\pm 10°$. Some of the obtained spectra in the ultraviolet

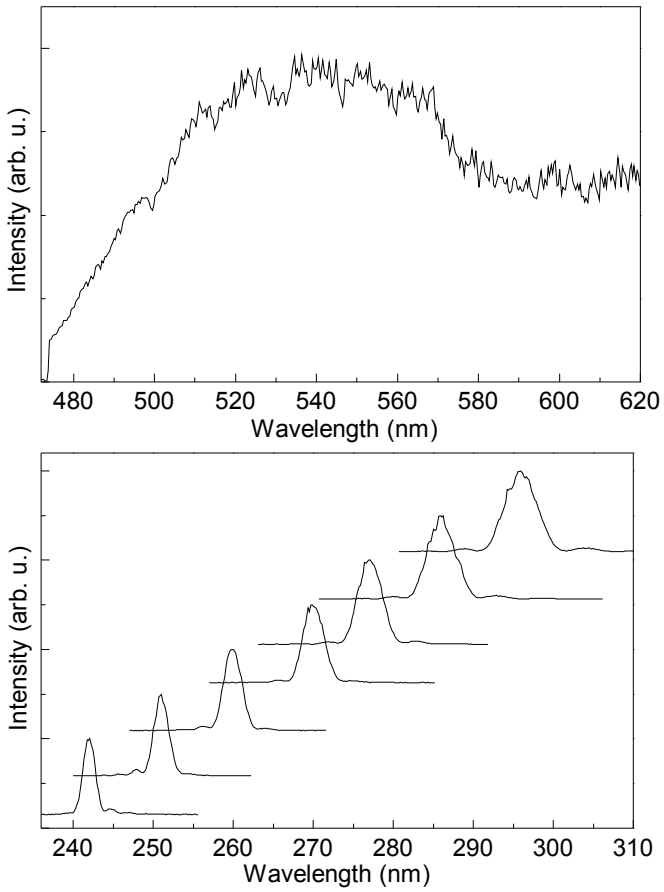

Figure 2.12: Tunable laser pulses in the ultraviolet spectral range. The white light spectrum generated in the YAG crystal (top) is selectively frequency doubled in a BBO crystal (bottom, spectra offset for clarity). Adapted from [53].

range are shown in Fig. 2.12 (bottom panel). They support pulse durations of approximately 25 fs. The ultraviolet pulses are filtered to remove undesired spectral components before being focused on a gold photocathode. Pulse energies on the

order of 1 pJ are achieved which is sufficient for working in the single electron regime. In the present experiment, the ultraviolet laser pulses are not temporally compressed. However, this does not affect the validity of the obtained results, because no temporal measurements are performed.

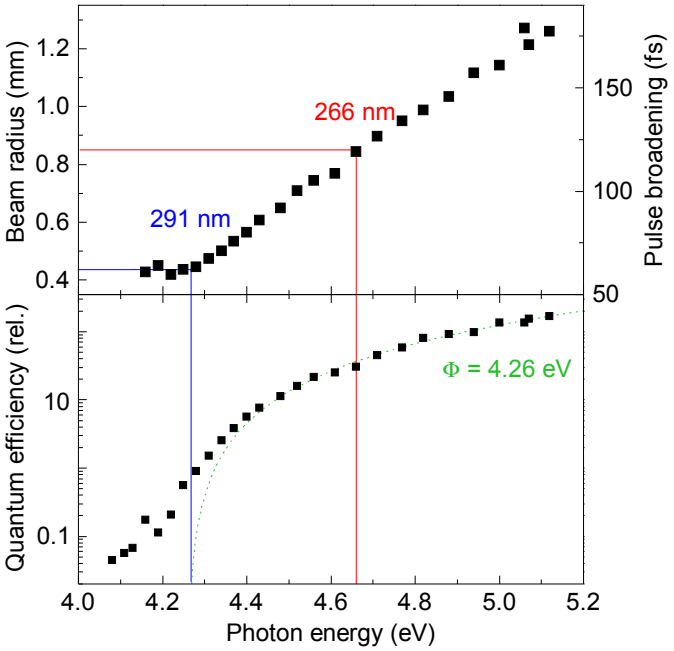

Figure 2.13: Electron generation with tunable ultraviolet pulses. Reducing the photon energy of the incident radiation results in a narrowing of the transverse momentum distribution as evidenced by the decreasing electron beam radius. At the same time, the quantum efficiency of the generation process is reduced. Adapted from [53].

Figure 2.13 shows the experimental results obtained for the generation of electron pulses by a tunable photon energy. In the absence of space-charge, the electron beam radius on the detector after free propagation provides a measure of the transverse velocity spread of the electron pulse [81]. From the determined values of the transverse velocity spread, the pulse broadening is calculated for an acceleration field of $10\,\mathrm{kV\,mm^{-1}}$ under the assumption that the transverse velocity spread equals the longitudinal velocity spread [53].

The measurement indicates that the reduction of the laser photon energy results in a reduction of the transverse velocity spread of the electrons as is expected for a lowered excess energy. At the same time, the quantum efficiency of the electron emission process is reduced because scattering losses in the cathode material prior to photoemission increase. The green curve is a fit to the data using a quadratic relationship between quantum efficiency and excess energy [80]. The effective work

function for the gold photocathode used here is found to be $\Phi = (4.26 \pm 0.05)\,\mathrm{eV}$. This corresponds to a cutoff wavelength of 291 nm and is in good agreement with previously reported values [83]. The quantum efficiency does not drop to zero at the cutoff, because our ultraviolet laser pulses contain spectral components below the cutoff wavelength, even if the central wavelength is above the cutoff (see Fig. 2.12).

Figure 2.13 shows that the transverse velocity spread of the electron pulses can be reduced to half when an excitation wavelength of 291 nm is used instead of 266 nm (third harmonic of the titanium:sapphire laser system). At the same time, the pulse broadening is reduced from about 120 to 60 fs. This shows the great potential of matching the photon energy to the work function.

The total electron pulse duration $\tau_{electron}$ is not determined by the temporal broadening alone. Instead, it is the convolution between broadening caused by the longitudinal momentum distribution $\tau_{broadening}$ and the pulse duration of the generating laser pulse τ_{laser}:

$$\tau_{electron} = \sqrt{\tau_{broadening}^2 + \tau_{laser}^2}. \tag{2.5}$$

When the laser's central wavelength is matched to the work function, the energy bandwidth of the laser pulse determines the momentum spread of the electron pulse. Since the laser's bandwidth and its transform-limited pulse duration are inversely proportional, two opposing effects have to be balanced: On the one hand, a shorter laser pulse reduces the total electron pulse duration. But on the other hand, its increased bandwidth enlarges the momentum spread of the electrons and thus lengthens the electron pulse due to broadening. A trade-off between these two contributions can be found and an optimum laser pulse duration for a given acceleration field can be determined. For example, for an accelerating field strength of $10\,\mathrm{kV\,mm^{-1}}$, the optimum laser pulse duration is approximately $\tau_{laser} \approx 40\,\mathrm{fs}$. This results in an electron pulse duration of about $\tau_{electron} \approx 70\,\mathrm{fs}$ [53].

The discussion above demonstrates how the pulse duration for single-electron pulses can be reduced to below 100 fs by matching the laser wavelength to the work function of the cathode material and by choosing a suitable laser pulse duration. The pulse energy of the ultraviolet laser pulses produced by white light generation and subsequent selective frequency-doubling is sufficient to work in the single-electron regime.

Despite these clear advantages, we chose to work with the third harmonic of our laser pulses for generating electrons in the experiments described below. The reason for this is mainly convenience. Frequently, it is practical to work with more than one electron per pulse, for example during alignment procedures. This is possible with laser pulses from third harmonic generation because of the higher efficiency of the frequency conversion process compared to the tunable ultraviolet source.

In addition, some of the experiments, in particular those discussed in Chapt. 5, benefit from having the highest possible pulse energy available to pump the sample. Here again, we profit from the higher conversion efficiency of the third harmonic

generation process. Last but not least, the white light generation within the tunable ultraviolet source is somewhat susceptible to pulse length fluctuations of the incident laser pulses, particularly since it is working at the lower end of its operational range. This has sometimes been a problem during long-time measurements that lasted several hours.

2.4 Characterization of the electron beam

2.4.1 Electron beam propagation

In order to fully understand the imaging and diffraction properties of our electron diffraction apparatus we need to be able to calculate the behavior of the electron beam as it propagates from its source to the detector. The physical tools required to do so will be reviewed on the following pages. A more detailed discussion of the topic can be found in the textbook by Hintersberger [84].

Since our diffraction apparatus contains only very few electron optical elements (as compared to e. g. an electron microscope or an accelerator beamline) the discussion will be limited to the following parts:

- electron source (photocathode),
- acceleration region,
- anode hole,
- propagation,
- solenoid lens.

In our experimental setup, the electron pulses propagate almost along a straight line, with only small angular deviations from the design axis around which all electron optical components are centered. It is therefore reasonable to treat the electron like a paraxial ray in optics and describe it by two parameters, its distance x from the design axis of the experiment and the derivative $x' = \frac{\mathrm{d}x}{\mathrm{d}z}$ which denotes the (small) angle between the electron trajectory and the design axis along the z-direction. The propagation of the electron can then be modeled using the ABCD-matrices familiar from optics. The position and angle of an electron after the propagation through an electron-optical system, described by the matrix M_{system}, can be calculated as

$$\begin{pmatrix} x \\ x' \end{pmatrix}_{final} = M_{system} \begin{pmatrix} x \\ x' \end{pmatrix}_{initial} . \tag{2.6}$$

The propagation of an electron through a distance l, measured along the design axis of the system, is described by the matrix

$$M_{prop} = \begin{pmatrix} 1 & l \\ 0 & 1 \end{pmatrix} . \tag{2.7}$$

The effect of a thin lens with focal length f is represented by a matrix

$$M_{lens} = \begin{pmatrix} 1 & 0 \\ -\frac{1}{f} & 1 \end{pmatrix}. \tag{2.8}$$

The matrix of an electron-optical system consisting of several different elements can be calculated as the product of the matrices of the individual components.

Although it is often useful to be able to mathematically propagate a single electron through an electron-optical system, most of the time, we are interested in the properties of the electron beam formed by many individual electrons. Assuming an approximately Gaussian spatial and angular distribution for the ensemble of electrons forming the electron beam, we can conveniently describe the electron beam by a symmetric (2×2)-matrix $\boldsymbol{\sigma}$ with a positive determinant:

$$\boldsymbol{\sigma} = \begin{pmatrix} \sigma_{11} & \sigma_{12} \\ \sigma_{12} & \sigma_{22} \end{pmatrix}. \tag{2.9}$$

The determinant of this matrix is related to the emittance E:

$$E = \pi\sqrt{\det \boldsymbol{\sigma}} = \pi\sqrt{\sigma_{11}\sigma_{22} - \sigma_{12}^2}, \tag{2.10}$$

which is a measure for the focusability of the electron beam. The diagonal elements of the matrix $\boldsymbol{\sigma}$ are connected to experimentally accessible beam parameters, σ_{11} is the square of the standard deviation of the beam's spatial distribution with respect to its center of mass, σ_{22} is the standard deviation of the beams angular distribution. The off-diagonal element σ_{12} describes the correlation between the position and the transverse momentum of the particles, $\sigma_{12} > 0$ means the beam is diverging, $\sigma_{12} < 0$ means the beam is converging, and $\sigma_{12} = 0$ describes a beam at its waist.

The beam's matrix after propagation through a system described by a matrix M_{system} is calculated as

$$\boldsymbol{\sigma}_{final} = M_{system}\boldsymbol{\sigma}_{initial}M_{system}^{\mathrm{T}}. \tag{2.11}$$

Thus, we can calculate how the electron beam propagates through our electron-optical system provided that we know the beam parameters at the source. Note that the previous discussion assumed cylindrical symmetry for the electron beam. This assumption is not always satisfied in our experimental conditions. In this case, however, the discussion can be easily extended to consider the horizontal x- and the vertical y-plane and the respective angles independently [75].

Electron source

In our experiments, it is difficult to determine the electron beam matrix at the source $\boldsymbol{\sigma}_{source}$ directly, because our electron detector is located many centimeters

downstream from the source. Nevertheless, we can make some educated assumptions on the shape of the matrix $\boldsymbol{\sigma}_{source}$. The source's area must be related to the size of the optical focus on the photocathode. Thus, the matrix element σ_{11} can be estimated from optical considerations. The matrix element σ_{22} describes the angular distribution of the electrons directly after photoemission. It is dependent on the excess energy of the electrons liberated from the metal surface as well as on the microscopic structure (roughness) of the photocathode's surface [53]. Neglecting any inhomogeneities of the roughness over the size of the optically excited area, there will be no correlation between the emitted electron's position and its transverse velocity. Thus, we can set the off-diagonal elements of $\boldsymbol{\sigma}_{source}$ to zero.

Acceleration region[3]

The region between the photocathode and the anode in our electron gun basically resembles a plate capacitor. In a plate capacitor an electron of charge $-e$ and mass m experiences a force of magnitude $F = -eE$ accelerating it towards the anode. The electric field $E = U/d$ is homogeneous and depends on the applied acceleration voltage U and the distance d between cathode and anode. If we neglect the initial longitudinal velocity of the electron, which is very small compared to its final velocity in our experiments, the electron will reach the anode after a time

$$t_{anode} = \sqrt{\frac{2md}{eE}} \tag{2.12}$$

with a longitudinal velocity

$$v_{l,anode} = \sqrt{\frac{2edE}{m}}. \tag{2.13}$$

Note that if the electron had traveled at its final velocity $v_{l,anode}$ for the time t_{anode}, it would have covered the distance $2d$. Since the acceleration is solely in the forward direction, the transverse velocity of the electron does not change during the propagation to the anode $v_{t,anode} = v_{t,cathode} = v_t$. The transverse position of the electron relative to its origin $x_{cathode}$ changes to $x_{anode} = x_{cathode} + t_{anode} v_t$. We can now write down the electron's parameters at the anode:

$$\begin{pmatrix} x \\ x' \end{pmatrix}_{anode} = \begin{pmatrix} x_{cathode} + t_{anode} v_t \\ \frac{v_t}{v_{l,anode}} \end{pmatrix} = \begin{pmatrix} x_{cathode} + 2d\frac{v_t}{v_{l,anode}} \\ \frac{v_t}{v_{l,anode}} \end{pmatrix} = \begin{pmatrix} 1 & 2d \\ 0 & 1 \end{pmatrix} \begin{pmatrix} x_{cathode} \\ \frac{v_t}{v_{l,anode}} \end{pmatrix}. \tag{2.14}$$

This means that we can calculate the state of an electron after the propagation through the acceleration region by a simple, unaccelerated propagation matrix over

[3] We assume non-relativistic electron energies, which is suitable for the typical acceleration voltages of few tens of kilovolts in our experiments.

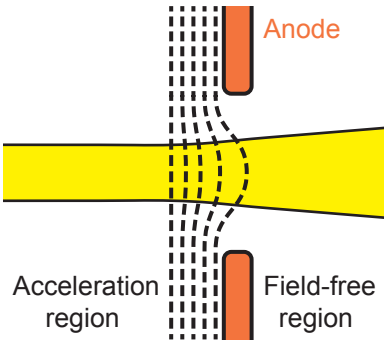

Figure 2.14:
Schematic drawing of the defocusing effect of the anode hole: The equipotential lines (dashed) in the acceleration region are bent towards the anode hole. This causes a defocusing lens effect for the electron beam (yellow) propagating through the hole.

twice the distance between the cathode and the anode provided that we assume the electron has its final velocity already at the cathode. Since the electron's final velocity $v_{l,anode} = \sqrt{2eU/m}$ is determined by the acceleration voltage U, again neglecting the electron's small initial velocity, this does not pose any difficulties and allows us to start the modeling of the electron beam right at the source.

Anode hole

A hole in the anode allows the electron beam to leave the acceleration region and to propagate towards the sample and the detector. It thus separates a region of electric field from a field-free region. Such an assembly forms an electrostatic aperture lens [75]. In the region of the anode hole the electric field lines are bent towards the edges of the hole. As a consequence, the equipotential lines are bulged towards the hole forming a defocusing lens (see Fig. 2.14 for an illustration). The focal length of an electrostatic aperture lens is $f \approx 2mv_{l,anode}/\left(-e\left(E_2 - E_1\right)\right)$, where E_1 and E_2 are the axial electric fields upstream and downstream of the hole, respectively. Since the E_2 vanishes in our case, we can simplify with the use of Eq. (2.13):

$$f \approx -4d. \tag{2.15}$$

The anode hole will thus behave as a thin lens with a negative focal length of four times the distance d between cathode and anode, independent of the acceleration voltage.

Solenoid lens

The electron beam is our experimental setup is focused by a solenoid lens as described in Sect. 2.2.2. The focal length f of such a lens for an electron is

$$f = \frac{4}{\int \mathrm{d}z \left(eB_z/mv_l\right)^2} = \frac{8mU}{e\int B_z^2 \mathrm{d}z}, \tag{2.16}$$

where v_l is the longitudinal velocity of the electron caused by the acceleration voltage U [75, 76].

2.4.2 Emittance measurement

Introduction

The objective of the electron gun design discussed above is to create an electron source with a small source size and a small velocity spread of the emitted electrons, i. e. a small emittance. In order to verify whether this was successful, the electron source needs to be characterized experimentally.

Emittance measurements of charged-particle beams are a standard task in the accelerator physics community [85]. Frequently, so-called quadrupole scan techniques are applied [86, 87]. In their simplest form, the strength of one or several magnetic quadrupole lenses is varied and the beam profile at a detector downstream of the lenses is recorded. Based on the calculated beam propagation the source's parameters can be fitted.

Implementation

In the present experiment, a variation of this approach is employed which makes use of the adjustable focal length of the solenoid lens of our setup. As detailed in Sect. 2.2.2, the focal length of a solenoid lens is inversely proportional to the current run through its wire providing an easy experimental parameter to adjust. For each setting of the magnetic lens current in the range from 0.0 to 2.2 A an image of the electron beam on the detector is recorded.

Data evaluation

For the subsequent analysis one needs to retrieve the beam radius from the acquired images. In principle, a weighted root mean square (RMS) deviation of the beam with respect to its center would be a good measure for this. However, it is non-trivial to calculate this value for real experimental data because of the noisy, non-zero data points outside of the beam. Even if great care is taken to subtract a good-quality background image, it was found that calculating the center of mass (COM) and the weighted RMS deviation of the beam according to

$$x_{COM} = \sum_{ROI} x_i I(x_i, y_j) \Big/ \sum_{ROI} I(x_i, y_j), \tag{2.17a}$$

$$y_{COM} = \sum_{ROI} y_j I(x_i, y_j) \Big/ \sum_{ROI} I(x_i, y_j), \tag{2.17b}$$

$$RMS = \sqrt{\sum_{ROI} \left((x_i - x_{COM})^2 + (y_j - y_{COM})^2 \right) I(x_i, y_j) \Big/ \sum_{ROI} I(x_i, y_j)}, \tag{2.17c}$$

where the summation goes over all pixels (x_i, y_j) in the region of interest (ROI), yields significantly varying results depending on the size and shape of the region of interest.

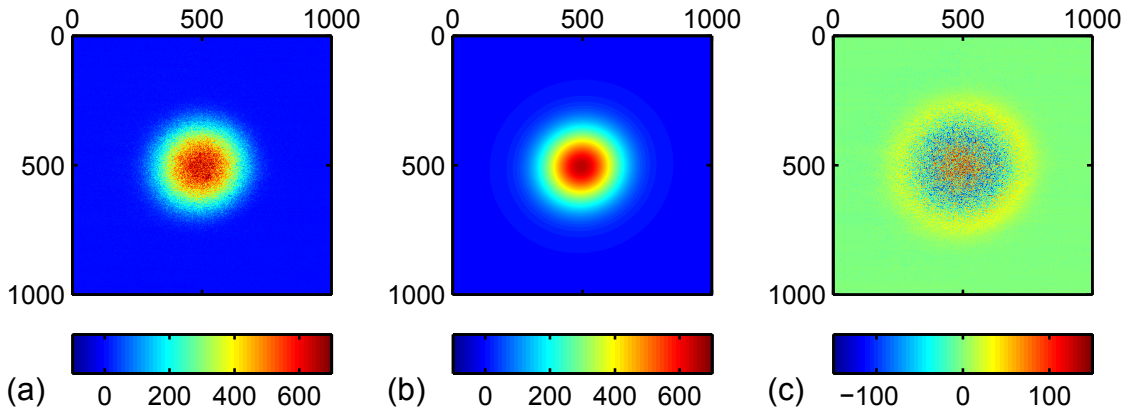

Figure 2.15: Example of an electron beam profile at the detector for a magnetic lens current of 1.0 A. The measured profile (a) is approximately Gaussian but shows a slight ellipticity. It was therefore fitted with an elliptical Gaussian (b), resulting in values of 1.635 mm and 1.488 mm for major and minor half-axes, respectively. Panel (c) shows the difference between the fitted and the original beam profile. The units of the plots' horizontal and vertical axes are pixels (pixel size: $15.6 \times 15.6\,\mu\text{m}^2$). The counts on a given pixel are color-coded.

In order to circumvent this problem we make use of the fact that our electron beams have an almost Gaussian profile and apply a fitting technique which is robust against background and noise issues. Since the electron beams are slightly elliptical the two-dimensional fit function is chosen to be an elliptical Gaussian with major and minor axes as well as the rotation angle as the main fit parameters.

Figure 2.15 shows an example of a fitted electron beam profile on the detector for a certain value of the magnetic lens current. The fitted beam radii are corrected for the point spread function of the detector (see Sect. 2.2.6 for details) in order to retrieve the actual width of the electron beam.

By varying the focal length of the magnetic lens, the focusing behavior of the electron beam can be studied. For each setting of the magnetic lens, the electron beam profile at the detector is fitted. The resulting beam parameters as functions of the magnetic lens current are shown in Fig. 2.16. This data was obtained with single-electron pulses generated by laser pulses at a wavelength of 266 nm.

The link between the electron beam matrices at the source $\boldsymbol{\sigma}_{initial}$ and at the detector $\boldsymbol{\sigma}_{final}$ is made by Eq. (2.11):

$$\boldsymbol{\sigma}_{final} = M_{system}\boldsymbol{\sigma}_{initial}M_{system}^{\mathrm{T}}.$$

Due to the off-diagonal elements in the system's matrix M_{system}, the matrix element $\sigma_{11,\,final}$, which describes the beam's size at the detector, is affected by both the size

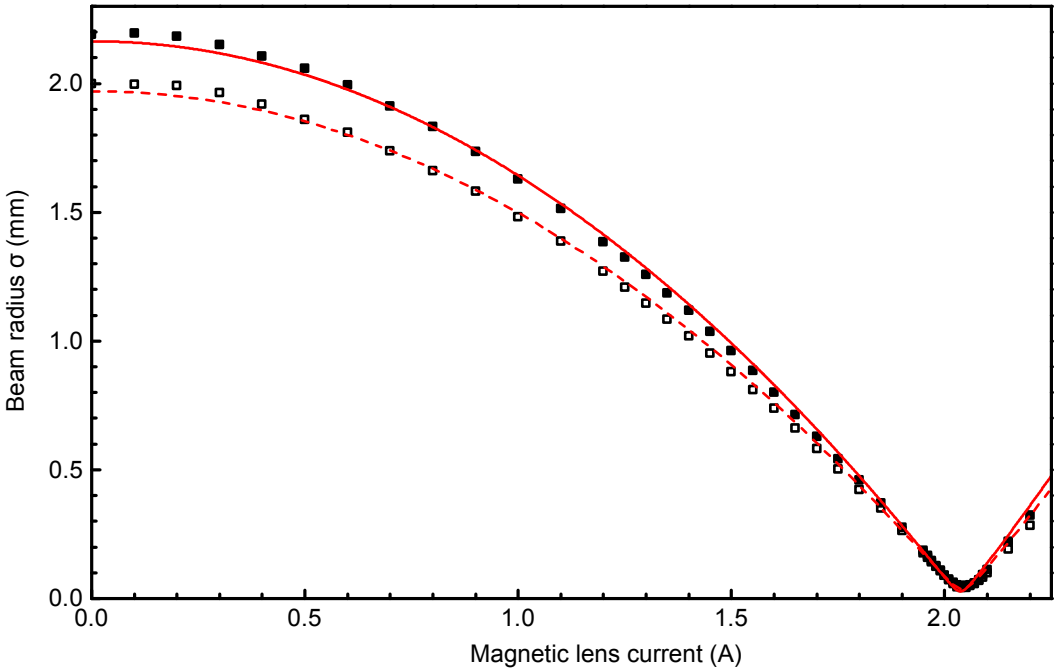

Figure 2.16: Magnetic lens scan of the electron beam. Major and minor beam radii of the elliptical beam profile are plotted as a function of the magnetic lens current (squares). The beam radii were corrected for the point spread function of the detector. The red lines are least-square fits based on the matrix method for electron beam propagation.

and the divergence of the beam at the source. Consequently, a fit of the beam radius at the detector as a function of the magnetic lens current can be used to determine the beam parameters at the source. In this situation, the system's matrix M_{system} can be determined from the dimensions of the experimental setup. Knowledge of the exact focal length of the magnetic lens is not required. It is sufficient to know that it is inversely proportional to the current through the lens because an additional fit parameter can be introduced that connects the focal length to the current.

The red lines in Fig. 2.16 show the results of least-square fits to the experimental data. The following parameters are retrieved (standard deviations).

	Source radius σ_r (µm)	Transverse velocity spread σ_{v_t} ($\mathrm{km\,s^{-1}}$)
Major axis	3.6	137
Minor axis	2.8	151

The small electron source sizes determined by the magnetic lens scan are in good agreement with the discussion in Sect. 2.2.2. This indicates the effectiveness of the focusing lens within the vacuum system. The ellipticity of the source spot can be attributed to the slightly elliptical profile of our laser beam. The variation in the transverse velocity spread might be due to inhomogeneities in the cathode surface or in the acceleration region.

2.5 Spatial and temporal overlap

In order to perform a successful time-resolved electron diffraction experiment, it is crucial to overlap the laser pulse and the electron pulse on the sample spatially and temporally. In the following, the procedures for finding the spatial and temporal overlap are outlined.

As a first step, the path of the electron beam has to be determined as it cannot be influenced as easily as the laser beam. Since the electron beam is invisible, one has to rely on the image produced on the electron detector. For a rough alignment the unfocused (or only slightly focused) electron beam can be used to produce a shadow image of the sample holder. It has proven beneficial to use a prominent feature like a sharp corner of the sample holder to block the electron beam. Ideally, this feature is located next to the actual sample of the experiment, so that errors while shifting from alignment target to sample are reduced. The procedure is repeated with the focused electron beam. Depending on the exact focusing conditions, a real shadow image might not be detectable. In this case, one can use the integrated counts on the detector to find the sample position where the blocking feature of the sample holder is in the center of the electron beam.

In the second step the laser beam is overlapped with the fixed alignment feature. This can be done conveniently using the sample observation camera (see Sect. 2.2.5).

The laser beam is observable on the sample holder and can thus be steered to the alignment feature using the last mirror in the beam path before the vacuum chamber. The laser focus can be adjusted by shifting the focusing lens outside of the vacuum chamber along the beam direction. It is convenient to observe the laser light transmitted through the vacuum chamber. When the laser beam is not focused on the sample, a shadow image of the alignment feature will be produced. In contrast, when the laser is focused on the target, the transmitted light will be generally attenuated but no distinct features are visible. Since both the electron beam and the laser beam are now overlapped with the alignment feature, they are overlapped with each other.

The positions of the laser beam and the electron beam in the sample plane can be verified by knife-edge measurements [88] using the sample holder. Since the two beams are not collinear and since the sample holder has a certain thickness, one has to check that the beams are blocked by the same edge of the sample holder. This may also be a problem for the alignment procedure described above.

The temporal overlap, the so-called time zero, is more difficult to find. It requires the effective path lengths (that take into account the velocities of laser and electron pulses) of the eletron beam and the laser beam starting from the beam splitter to be matched precisely. Assuming pulse durations in the range of hundreds of femtoseconds, the path lengths have to be determined with an accuracy of tens of micrometers, which is far beyond the measurement uncertainties that can be achieved while measuring the beam paths. Consequently, one has to make use of an interaction between the laser pulses and the electron pulses, which can be detected easily. Ideally, the effect is long-lived, i. e. it lasts longer than the actual cross-correlation time. This avoids having to vary the delay between the two pulses in small steps which would make the procedure very time-consuming.

In order to find the temporal overlap, we use photoelectrons that are generated when the laser hits the sample holder. We found this to work best when the laser is focused on a sharp edge of the sample holder or the sample. This behavior is attributed to the fact that a multiphoton process is required to generate the photoelectrons. This process is enhanced at sharp edges of the sample because of field enhancement. If the timing is correct, the emitted photoelectrons deflect electrons from the electron beam resulting in a redistribution of electrons in the beam profile recorded at the detector.

Figure 2.17 shows a typical time-zero scan. The delay between laser pulse and electron pulse is varied and the electron beam profile is recorded. In order to make changes in the beam profile visible, a reference image at a delay line position of $t_{ref} = 0\,\mathrm{ps}$ is subtracted. The image at 90 ps shows clear signs of a redistribution of electrons within the beam. In order to not rely on the images of the beam profile alone, the changes in the beam profile are summarized in a single quantity which

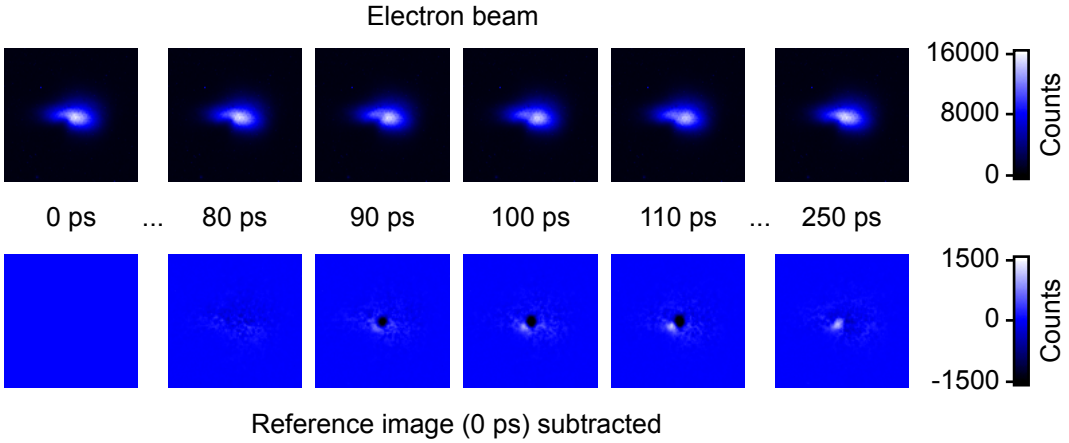

Figure 2.17: Determination of spatial and temporal overlap between laser pulse and electron pulse. The laser beam is focused on a sharp corner of the sample holder (bottom left of the images). The generated photoelectrons deflect electrons from the electron beam resulting in a change of the electron beam profile on the detector, which is clearly visible in the difference images.

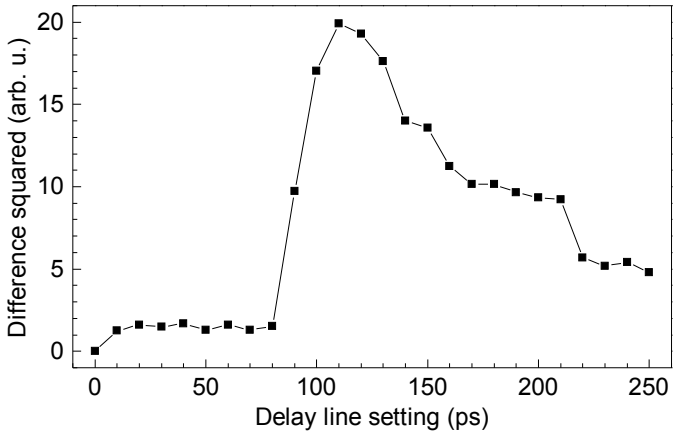

Figure 2.18: Determination of temporal overlap. The summation of the squares of the pixel values in the difference images in Fig. 2.17 results in a single number characterizing the changes in the electron beam profile. This analysis allows time zero to be determined with higher precision than possible by looking at the difference images.

we call *difference squared*:

$$\Delta C(t) = \sum_{i,j} \left[c_{ij}(t) - c_{ij}(t_{ref})\right]^2 , \tag{2.18}$$

where c_{ij} are the pixel values of the electron beam images. This analysis results in Fig. 2.18.

The deflection of electrons from the beam lasts for a few hundred picoseconds. It is thus suitable to perform a fast and coarse scan as shown above. From this data, we conclude that the temporal overlap takes place for a delay line position between 80 and 90 ps. In a second scan with a smaller step size, time zero can be determined with an accuracy of about 1 ps. Once the temporal overlap is found with this precision, the actual sample of interest can be moved to the intersection point between laser and electron beam and the time-resolved experiment can begin.

The procedure described above is sufficient for finding a good starting point from where time-resolved experiments with femtosecond resolution become possible. Due to its low temporal resolution it does not provide a precise reference point from which time delays could be measured with femtosecond precision. Quite often this is not required in a time-resolved experiment because one is mainly interested in the rate of change of a certain parameter. In this case, time zero can be defined as the onset of the observed dynamics, which is assumed to start immediately after laser excitation. If, however, one is interested in an exact timing of a process with respect to the triggering laser pulse, time zero has to be determined with femtosecond precision. The most precise way of doing so is the cross-correlation experiment described in Chapt. 5.

2.6 Velocity matching

In an ultrafast electron diffraction experiment with a solid sample, a spatially extended laser beam and a spatially extended electron beam are incident on a planar sample surface. In order to avoid detrimental effects on the temporal resolution of the experiment, the two beams have to be oriented carefully with respect to each other and to the sample. It has to be ensured that every point of the sample surface experiences the same delay between the laser pulse and the probing electron pulse. In the simplest geometry that fulfills this requirement, the electron beam and the laser beam are collinear. Unfortunately, this is difficult to realize in practice.

In the present work, a different approach is employed that makes use of the fact that the electron travels at only a fraction of the speed of the laser pulse. It is related to an early work on the velocity mismatch in gas-phase electron diffraction experiments [89].

Figure 2.19 shows the experimental geometry. The angles α and β have to be chosen such that the laser pulse and the electron pulse sweep across the surface of

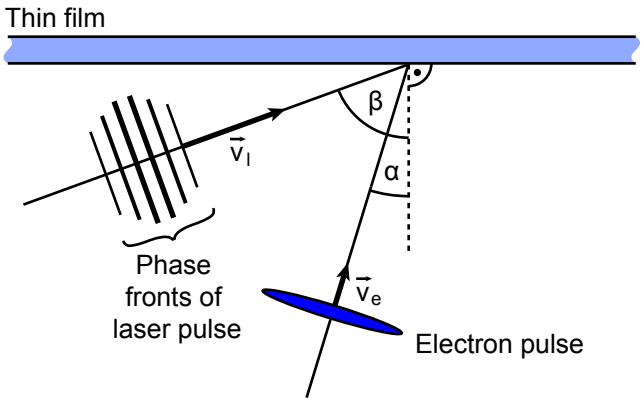

Figure 2.19: Velocity matching between laser pulse and electron pulse.

the sample with the same velocity. Consequently the following equation has to be satisfied:

$$\frac{v_e}{\sin\alpha} = \frac{v_l}{\sin\beta}. \tag{2.19}$$

Here, v_e is the velocity of the electron pulse and v_l is either the group velocity of the laser pulse, as is the case for a conventional pump-probe experiment, where the dynamics are triggered by the intensity profile of the laser pulse, or its phase velocity, like in the case of the experiment discussed in Chapt. 5, where the field of the laser pulse is relevant. In fact, group and phase velocity are usually equal in practice, because the experiments take place in vacuum. Equation (2.19) does not determine the angles α and β completely, but leaves some freedom in choosing the angles.

As an example, the experimental situation for the streaking experiments discussed in Chapt. 5 is considered. Electrons at an energy of 25 keV have a velocity of $v_e = 0.30\,c$, where c is the speed of light in vacuum. The laser pulse travels with a phase velocity $v_l = c$. In order to satisfy Eq. (2.19), $\sin\alpha/\sin\beta$ must be equal to $v_e/v_l = 0.30$. This is achieved for the angles chosen in the experiment: $\alpha = 17°$ and $\beta = 77°$. Thus, by selecting appropriate incident angles for the laser and the electron beam the velocity mismatch between laser and electron pulse can be compensated and a reduction of the temporal resolution of the experiment can be avoided.

As mentioned above, there is some flexibility in choosing the incident angles for velocity matching. However, in an electron diffraction experiment with a single-crystalline sample, there is an additional constraint. The crystal structure of the sample has to be oriented with respect to the electron beam in order to obtain a proper diffraction pattern. Since the sample surface usually cannot be prepared with an arbitrary crystallographic orientation, this determines the angle of incidence for the electron beam. In this case, it might not be possible the satisfy Eq. (2.19) in a

practical way.

With this situation in mind, another approach for circumventing the velocity mismatch between laser and electron pulse was developed [90]. It is based an tilted optical pulses, i. e. laser pulses where the plane of highest intensity forms a non-normal angle with the propagation direction of the pulse. Since the phase fronts of the pulses are still normal to the propagation direction, this type of velocity matching is only applicable in situations where the intensity profile of the laser pulse is important. Tilted pulses can be generated using a diffraction grating which is imaged onto the sample, but one has to take care of the orientation of the grating in order to avoid temporal distortions across the beam profile, which would reduce the time resolution in the experiment [91].

3 Transmission spectrometer for 200-µm sized samples

3.1 Introduction

Electrons at energies of 30 to 60 keV have a large scattering cross-section compared to x-rays. While this is often considered an advantage (see page 2 for an extended discussion), it also poses strong requirements on the samples one can study. In particular, experiments in a transmission geometry become challenging, since sample thicknesses in the range of tens of nanometers are required. These samples can be produced by different techniques depending on the material of interest [7]. Many metals, for example, can be evaporated conveniently onto a substrate from which they are then separated to produce freestanding films of the desired thickness. However, evaporation processes will most often result in poly-crystalline samples. Frequently, one is interested in single-crystalline specimens which produce clear and distinct diffraction spots in a diffraction experiment. In this case, the first challenge arises in growing a single crystal of the material. Even if this succeeds, thin films still have to be produced. In our group we have established the technique of ultramicrotomy [92, 93]. Here, slices with thicknesses down to tens of nanometers are sheered off of crystals with a diameter of up to 500 µm. Cutting samples with larger diameters becomes more and more difficult at the required small thicknesses. More often than not, the sample diameters are in the range of 100 to 200 µm, because larger single crystals are not available or because they cannot be cut at the desired thickness. Thus, the typical samples for ultrafast electron diffraction in a transmission geometry have a thickness of tens of nanometers and a diameter of few hundred microns.

In a time-resolved diffraction experiment the dynamics of interest are usually triggered by a short laser pulse. This pulse can start some chemical reaction [37], a phase transition [50] or a heating process [46]. In all cases it is important to know the absorption properties of the sample, in order to determine how much incident pulse energy is required to achieve the desired effect. For example, if a chemical reaction is supposed to be triggered it is crucial to provide enough laser photons at the correct photon energy to make a sufficient number of molecules react. On the other hand, it is important to avoid that too much laser energy is deposited in the sample such that it may be destroyed by thermal or other effects. Knowing the absorption properties of the sample also allows to match the laser-excited volume of the sample to the volume probed by the electrons. In short, in order to perform a successful time-resolved diffraction experiment, it is crucial to know the optical absorption properties of the sample.

The absorption characteristics of a material are directly related to the imaginary part of its complex index of refraction, which can be deduced from transmission measurements. This is why a transmission spectrometer was developed that is adapted to the requirements of ultrafast electron diffraction experiments and fulfills the following design criteria:

- spot size of 200 µm,
- large spectral range,
- high sensitivity,
- easy alignment.

The device, referred to as *microspectrometer* in the following, is based on a design from Prof. Eberhard Riedle's group at the LMU, which was improved in several aspects.

3.2 Design of the microspectrometer

The microspectrometer is depicted in Fig. 3.1. The light source for the spectrally resolved absorption measurement is a deuterium tungsten halogen lamp (Ocean Optics, Inc., DH-2000-BAL) covering a spectral range from the ultraviolet to the infrared. The detector for the light transmitted through the sample is a miniature spectrometer (Ocean Optics, Inc., USB2000XR-1+ES) with a wavelength range from 200 to 1030 nm and an optical resolution of 2.0 nm (full width at half maximum, FWHM). Both the light source and the detector are connected to the actual microspectrometer device by means of optical fibers with a core diameter of 200 µm (Ocean Optics, Inc., QP200-1-SR-BX). The microspectrometer consists of four 90° off-axis parabolic mirrors with an effective focal length of 80 mm (Kugler GmbH). These mirrors have an outer diameter of 49.5 mm and the diamond turned optical surface is coated with protected aluminum. The effective focal length and the diameter of the parabolic mirrors are matched to the numerical aperture of the optical fibers, $NA = 0.22$, corresponding to an opening angle of the emitted light of $\pm 12.7°$, such that all the light from the light source is collected. The aperture of the optical fiber coming from the light source is located at the focus of the first parabolic mirror. Thus, a collimated beam is created upon reflection. This beam is then focused by the second parabolic mirror. The sample is located at its focal point and the transmitted light is collected by the third parabolic mirror. Again a collimated beam results which is finally focused onto the entrance aperture of the optical fiber leading to the spectrometer.

The optical components are mounted in an optical cage system (Thorlabs GmbH, 60 mm rail separation). This simplifies the critical alignment of the off-axis parabolic mirrors by providing mounting plates that are intrinsically parallel. The remaining degree of freedom of the parabolic mirrors, the rotation about the optical axis, is fixed by alignment pins in the rear surface of the mirrors and corresponding holes

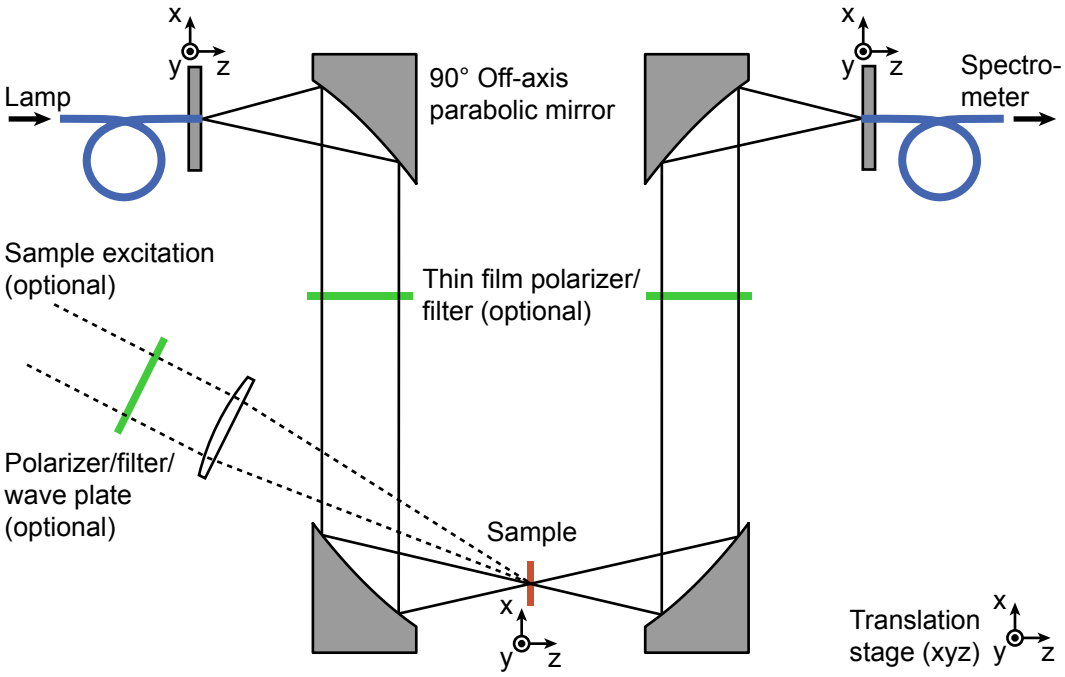

Figure 3.1: Schematic of the microspectrometer. Light from a deuterium tungsten halogen lamp is sent through an optical fiber, the aperture of which is imaged onto the sample by a pair of 90° off-axis parabolic mirrors. The light transmitted through the sample is collected and focused onto the entrance aperture of another optical fiber. A spectrometer enables spectrally resolved measurements of the transmission properties of the sample.

in the mounting plates. These holes can easily be produced with sufficient accuracy. Thus, each pair of mirrors forms a fixed unit that does not need to be adjusted after the initial alignment. The separation between the illuminating and the collecting mirror pairs can be adjusted in order to compensate for optical path length changes in thick samples.

The remaining alignment work deals with the positioning of the exit and entrance apertures of the optical fibers coming from the light source and going to the spectrometer, respectively. XY translators allow the precise positioning of the end of the optical fiber. The movement along the light's propagation direction is achieved by sliding the XY translators along the rails of the optical cage system. Although this adjustment is not as precise as the sideways movements, the alignment does not pose any difficulties. Once prealigned, the system can easily be optimized by maximizing the signal in the spectrometer.

Between the second and the third parabolic mirror, there are 89 mm of clear space. This is where the sample is located. For convenience in adjusting, the sample is mounted on an XYZ linear translation stage such that it can be adjusted precisely with respect to the focal spot of the light. The positioning of the sample can be monitored on a PC screen with a CMOS camera equipped with a C-mount macro lens positioned at a 45° angle above the incident beam.

3.3 Characterization of the microspectrometer

Figure 3.2 shows the spectrum of the deuterium tungsten halogen lamp as measured through the microspectrometer setup. It represents the usable spectral range of the device and spans a wavelength interval from 215 to 1030 nm. When the microspectrometer is properly aligned and no sample is inserted, the exposure time of the spectrometer must not be longer than 1 ms which is the smallest possible setting. For any longer exposure time, the detector will saturate. This demonstrates the excellent light throughput of the microspectrometer setup and allows to make ideal use of the sensitivity of the spectrometer, such that measurement times are minimized and even samples with high optical densities can be studied.

In order to verify the proper alignment and the focusing performance of the microspectrometer, a beam camera was placed at the location of the sample. By translating it along the beam axis while monitoring the beam profile, the location of the smallest beam diameter can be found. The beam profile at this position is shown in Fig. 3.3. The profile is roughly circular and has a flat-top profile reflecting the intensity distribution at the exit aperture of the optical fiber coming from the lamp. The spot diameter is slightly below 200 µm (FWHM) as expected for a fiber core diameter of 200 µm and the 1:1 imaging system present here. The beam camera used to record the data shown in Fig. 3.3 is sensitive over a wide spectral range (190 to 1100 nm). Hence the resulting beam profile is spectrally integrated and provides

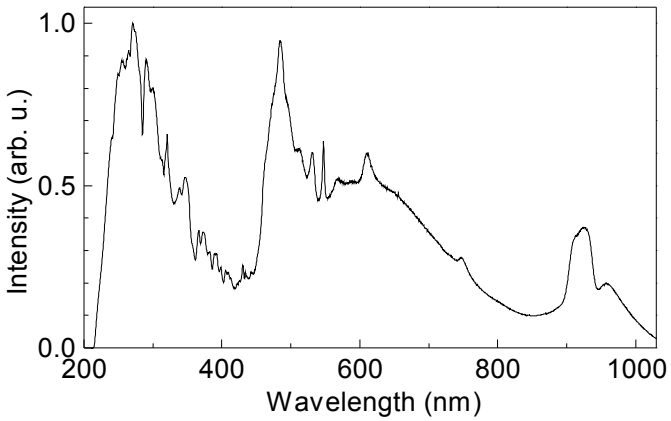

Figure 3.2: Spectrum of the deuterium tungsten halogen lamp as recorded through the microspectrometer.

no chromatic information about the focal spot.

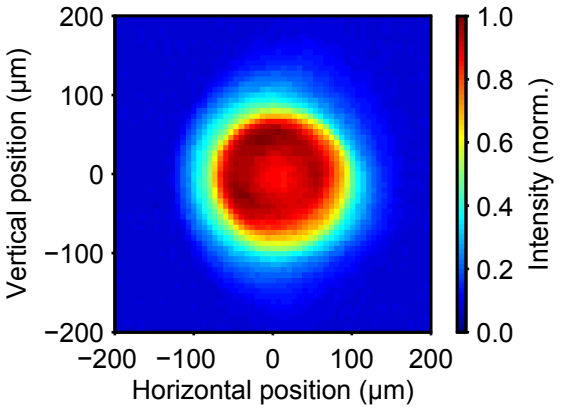

Figure 3.3: Focal spot of the microspectrometer. The beam profile at the location of the sample was recorded with a spectrally integrating beam camera.

To obtain spectrally resolved information about the quality of the focal spot, knife-edge measurements [88] were performed. A razor blade was mounted at the location of the sample. It was then scanned across the focal spot by means of a linear translation stage, and for each position of the blade a transmission spectrum was recorded. If the beam's intensity profile at the plane of the traveling knife-edge is denoted by $I_\lambda(x, y)$ for a given wavelength λ, then the recorded power at the detector can be written as

$$P(x, \lambda) = \int_{x}^{\infty} \mathrm{d}x' \int_{-\infty}^{\infty} \mathrm{d}y'\, I_\lambda(x', y'), \tag{3.1}$$

where x indicates the position of the knife-edge. This neglects diffraction effects at the edge of the blade and assumes that the blade is moved through the beam along the positive x-direction. As can be seen from Eq. (3.1), the knife-edge technique only provides information about the beam profile along one direction. This is why two sets of knife-edge measurements were performed to characterize the focal spot of the microspectrometer, one in the horizontal and one in the vertical direction.

The results of the knife-edge measurements are shown in Fig. 3.4. Here, a numerical differentiation was applied to the recorded data in order to visualize the beam profile. In addition, a 9-point running average along the position axis was used to smooth the data and to be less susceptible to statistical fluctuations in the subsequent analysis. For each wavelength, the positions were determined where the intensity drops to half its maximum value (black lines in Fig. 3.4). From these numbers the full width at half maximum of the beam was calculated resulting in values of (131 ± 3) µm in the horizontal direction and (193 ± 4) µm in the vertical direction. The center positions, half way between the half maximum points, fluctuated only by ± 1 µm and ± 2 µm in the horizontal and vertical directions, respectively. Here, all uncertainty values are standard deviations. The knife-edge measurements demonstrate that the focal spot is very homogeneous with respect to the wavelength: no significant shift of the focal spot with wavelength is observed. As expected from the spectrally integrated measurement above, the beam diameters are below 200 µm. The deviations from the beam camera measurement can be attributed to a slightly different position along the beam.

In summary, the presented design of a microspectrometer device combines 200 µm spatial resolution over a spectral range from 215 to 1030 nm with a very high sensitivity. The mechanical construction requires little to no day-to-day alignment and forms a practical base for transmission as well as other spectroscopic measurements.

In the following we discuss the theory of light transmission through a thin film that is necessary to understand and analyze experimental results obtained with the microspectrometer.

3.4 Light transmission through a thin film

The transmission through a thin film is determined not only by the absorption properties of the material. It is influenced significantly by the low thickness of the film which gives rise to multiple reflections between the surfaces of the film resulting in interference fringes in the transmission spectrum. In order to calculate the total transmission through the film, one needs to add all the transmitted parts that have undergone different numbers of reflections. This is illustrated in Fig. 3.5.

Consider a plane wave with a given (vacuum) wave-vector k incident under a 90° angle on a thin film of thickness d with a complex refractive index[1] $N = n(1+i\kappa)$. In

[1]This is the notation used in [94]; a notation of the form $N = n + i\kappa$ is also used frequently.

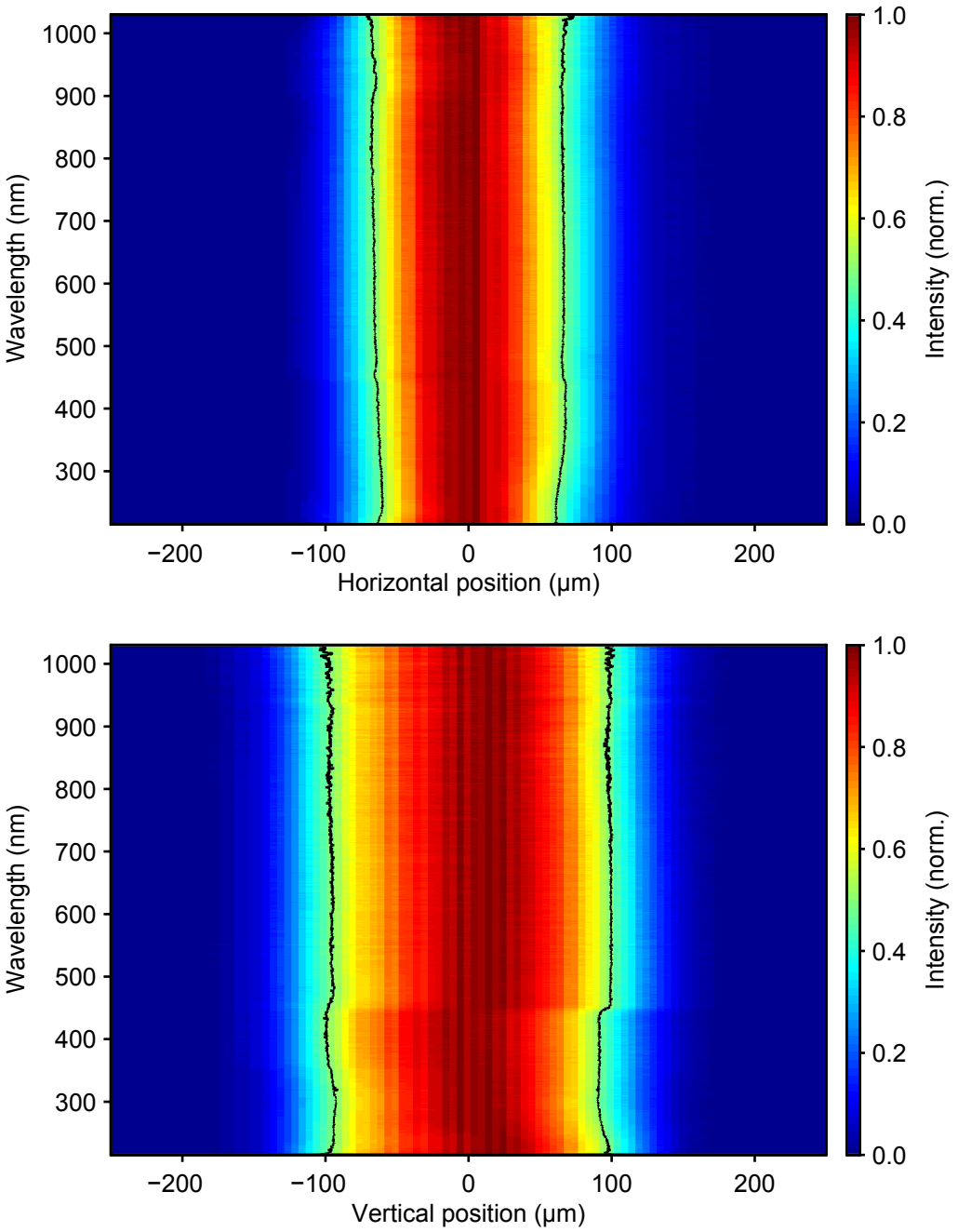

Figure 3.4: Knife-edge characterization of the focal spot. A knife-edge was translated through the focal spot and the transmission spectra were recorded. The data was numerically differentiated to retrieve the intensity profile. The black lines indicate the positions at which an intensity of half the maximum value is reached.

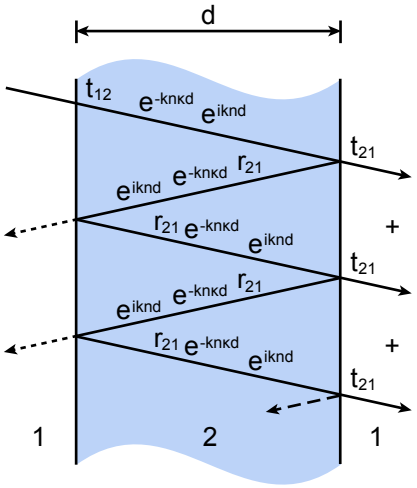

Figure 3.5:
Interference effects at a thin film. When light is incident on a thin film it is partially transmitted and reflected at each surface. Passing through the film's material, it experiences an amplitude and phase change due to the complex refractive index $N = n(1+i\kappa)$ of the material. The total transmitted light is the sum of the different parts undergoing multiple reflections in the film. (The rays are drawn under a non-normal angle of incidence for clarity only.)

general, the wave will be partially reflected and transmitted at each interface. The (complex) quantity t_{12} describes the amplitude and phase change of the wave upon transmission through the interface between medium 1 and medium 2. As the wave propagates from the front to the rear side of the film, two things happen. Firstly, the amplitude of the wave will be decreased by a factor $\exp(-kn\kappa d)$ because of the absorption of the film. Secondly, the wave will acquire a phase shift due to the index of refraction of the material, which can be conveniently expressed as $\exp(ikd)$. At the rear surface of the film, the wave will again be partially transmitted (t_{21}). The reflected part of the wave experiences an amplitude and phase change characterized by r_{21}. This back-reflected wave will propagate to the front surface of the film where it is again partially reflected. During each propagation through the film and during each reflection at the interfaces, the wave will pick up an additional amplitude and phase shift as described above. In order to calculate the total transmission through the film, one needs to add all the contributions transmitted through the rear surface of the film:

$$\begin{aligned} t_{total} &= t_{12}\exp(-kn\kappa d)\exp(ikd)t_{21}\sum_{j=0}^{\infty}\left[(r_{21})^2\exp(-2kn\kappa d)\exp(2ikd)\right]^j \\ &= \frac{\exp(-kn\kappa d+ikd)t_{12}t_{21}}{1-(r_{21})^2\exp(-2kn\kappa d+2ikd)}. \end{aligned}$$

In this equation the implicit assumption is made that the field components add coherently. This is the case when the coherence length of the light is larger than the optical path difference of the various components contributing to the sum. For the typical coherence lengths of many micrometers for the light coming from the lamp [94, 95] and typical film thicknesses of tens to hundreds of nanometers this is usually true. In the experiment, the spectrometer measures the intensity of the

light. Thus, the fraction of the light intensity transmitted through the film can be calculated as

$$T = |t_{total}|^2. \tag{3.2}$$

The amplitude and phase changes upon transmission or reflection at the surfaces of the film can be determined using the Fresnel equations for absorbing media. This is discussed in detail in Sect. 5.3. In the case of normal incidence, the Fresnel formulas have the following, simple form:

$$t_{12} = \frac{2}{1 + n(1 + i\kappa)}, \tag{3.3}$$

$$t_{21} = \frac{2n(1 + i\kappa)}{n(1 + i\kappa) + 1}, \tag{3.4}$$

$$r_{21} = \frac{n(1 + i\kappa) - 1}{n(1 + i\kappa) + 1}. \tag{3.5}$$

3.5 Transmission spectroscopy

Obtaining values for the complex refractive index $N(\lambda) = n(\lambda)(1 + i\kappa(\lambda))$ from thin film measurements is non-trivial. Without any prior knowledge of the quantities $n(\lambda)$ and $\kappa(\lambda)$, it is impossible to retrieve them from a single transmission measurement $T(\lambda)$. At least two independent measurements on the material are necessary. Traditionally, a normal incidence transmission measurement is combined with a near-normal incidence reflectance measurement in the so-called (R, T) method [96]. An alternative technique uses transmission measurements from films of different thicknesses [97]. Under the assumption of a certain model for the optical properties of the thin film, the required number of measurements can be reduced and it is even possible to calculate $n(\lambda)$ and $\kappa(\lambda)$ from a single transmission measurement. The algorithms involved in this kind of analysis are sophisticated and commercial computer programs exist for this purpose. For a detailed review of the determination of optical constants from thin film measurements, one may refer to [98].

In the following, a simplified analysis is presented, which illustrates the potential of the microspectrometer to retrieve the optical properties of thin films. It is based on transmission data from several films[2] of various thicknesses ranging from approximately 30 to 250 nm, that is fitted under the assumption of simplified models for $n(\lambda)$ and $\kappa(\lambda)$. The sample material is an epoxy resin (Araldite CY212) used for embedding samples prior to cutting them in the ultramicrotome. The thin films were mounted on transmission electron microscopy meshes with 2000 lines per inch. Because of the low transmission of these meshes (approx. 37 %), the transmission data for the resin films was obtained by recording a transmission spectrum of the

[2]The samples were prepared by Stefan Lahme.

resin on the mesh and dividing this data by the transmission spectrum of the naked mesh. Figure 3.6 shows a selection of the normalized transmission spectra. The data for the different film thicknesses is fitted using Eq. (3.2). For each transmission spectrum the thickness of the film as well as an offset compensating for inaccuracies in the normalization process and for scattering losses are determined in the least-square fitting routine. In addition, the real part of the refractive index of the film is modeled by a Sellmeier equation with two free parameters:

$$n(\lambda) = \sqrt{1 + \frac{c_1 \lambda^2}{\lambda^2 - c_2}}. \tag{3.6}$$

For the imaginary part of the refractive index a constant value is fitted such that

$$n\kappa(\lambda) = \text{const.} \tag{3.7}$$

This is reasonable because the resin does not show any significant absorption features in the wavelength range under investigation. The results of the least-square fit are marked as red lines in Fig. 3.6. The retrieved parameters in the Sellmeier equation (3.6) for the real part of the refractive index are $c_1 = 1.1880$ and $c_2 = 0.0170\,\mu\text{m}^2$. The imaginary part of the refractive index is determined to be $n\kappa = 6.5158 \cdot 10^{-20}$. Using these results, the refractive index of the resin is plotted in Fig. 3.7. The fitted transmission curves are in good agreement with the experimental data, showing that even this simplified analysis provides good information about the optical properties of the thin film. A more sophisticated analysis is possible but beyond the scope of the present demonstration of the microspectrometer device. As mentioned above a wealth of analysis techniques exists and commercial software packages are available for this purpose [98].

3.6 Additional applications

3.6.1 Fluorometry

In addition to the transmission measurements described above, the microspectrometer can be used for other applications. One such application is fluorometry: The sample is excited by light at a certain wavelength and emits light at longer wavelengths. This fluorescence can be detected efficiently because of the good detection efficiency of the microspectrometer for any light originating from the focal spot between the second and third mirror.

The mechanical construction of the device offers many possibilities for the illumination of the sample. Figure 3.1 shows one option. The exciting light can be excluded from being measured by using suitable filters or by choosing a normal angle between excitation and detection directions. The polarization of the incident

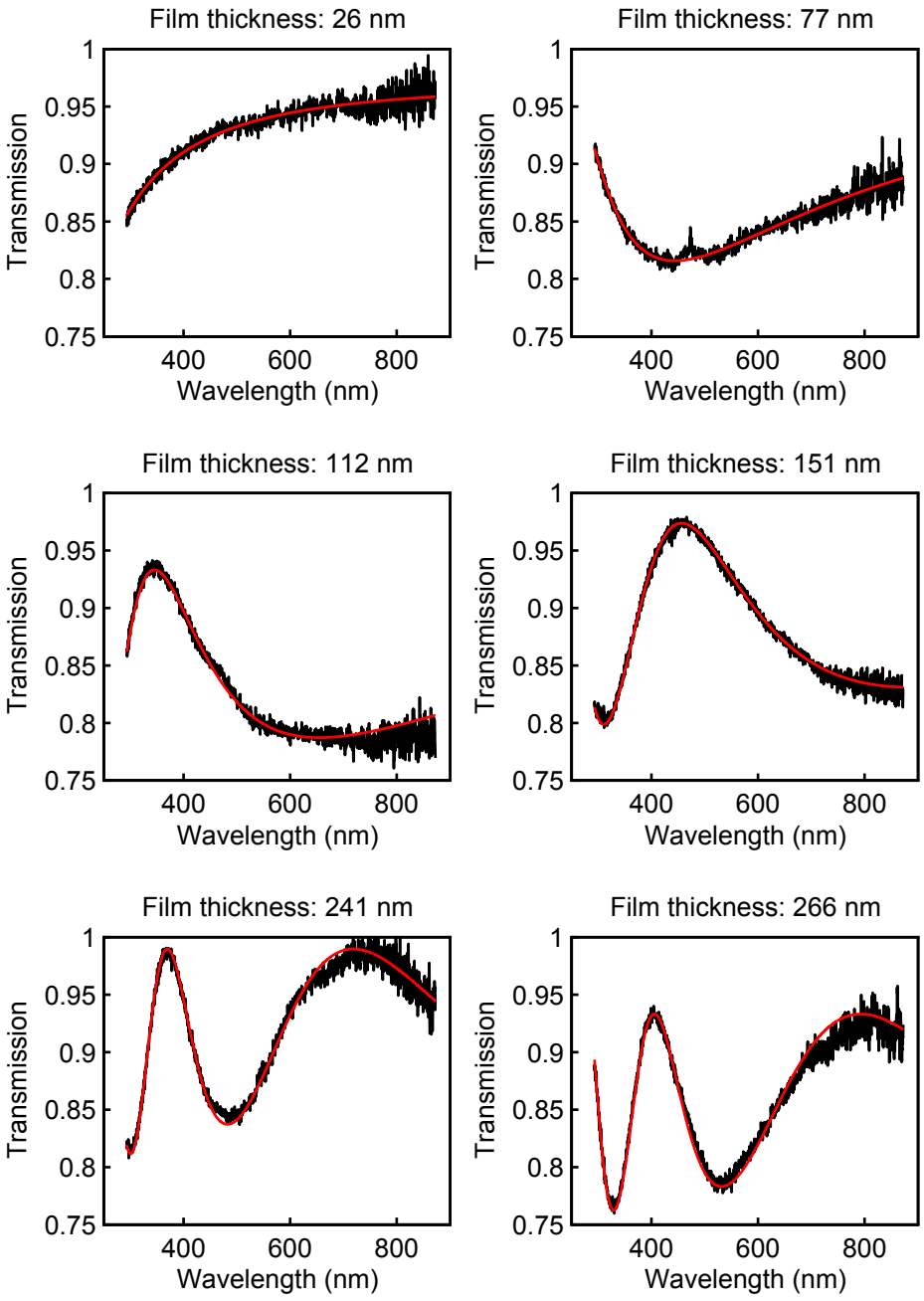

Figure 3.6: Transmission spectra of resin thin films. The red line indicates a least-square fit to the data using a simplified model for the complex refractive index of the material. The thickness values are also the result of the fit.

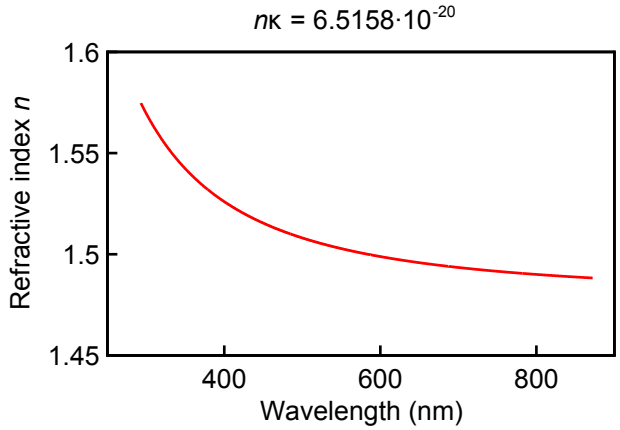

Figure 3.7: Fitted refractive index of resin.

light can be varied by means of a polarizer and/or a wave plate. Likewise, the polarization properties of the fluorescence can be analyzed using a thin film polarizer in the detection path.

Figure 3.8 shows an example of a fluorescence spectrum recorded with the microspectrometer as part of the Bachelor's thesis of Marina Hoheneder [99]. The sample, a single crystal of N-(triphenylmethyl)-salicylidenimine [100], was prepared as a thin film[3] with a thickness of 50 nm and a diameter of approximately 200 µm and was mounted at the focal point of the third mirror. It was excited by the second harmonic of the titanium:sapphire laser system in the laboratory: 800 µW of pulsed laser light at a central wavelength of 400 nm were focused onto the sample. The exciting radiation was blocked by a long pass filter (Chroma Technology HQ465LP) suppressing light below 465 nm and the fluorescence peaking at approximately 520 nm could be recorded.

3.6.2 Reflectance measurements

The microspectrometer is also suitable for reflectance measurements. This is of particular importance as it allows the investigation of nontransparent samples. In addition, a reflectance measurement in combination with a transmission measurement is required for the determination of optical properties using the (R, T) method [96,98]. The main challenge here is to separate the incident light from the reflected light. This can be conveniently achieved by using a bifurcated optical fiber assembly in which two optical fibers are combined such that their cores lie next to each other at the end of the y-shaped assembly. One of the arms of the fiber can be connected to the light source, the other one to the spectrometer. Since the two fiber cores are directly adjacent, it takes only a small deviation from normal incidence on the

[3]The sample was prepared by Stefan Lahme.

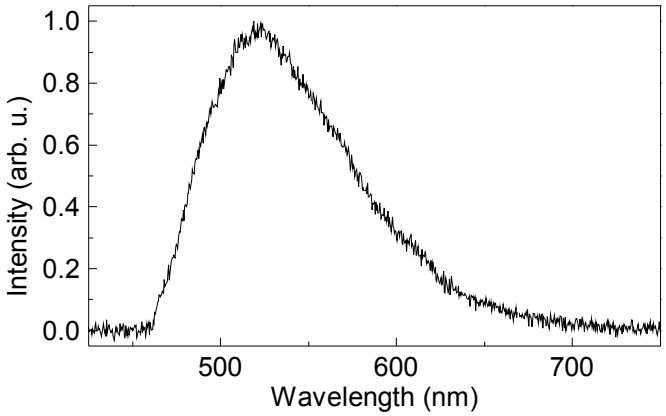

Figure 3.8: Fluorescence spectrum of N-(triphenylmethyl)-salicylidenimine recorded with the microspectrometer. The sample, a thin film with a thickness of 50 nm and diameter of 200 µm, was excited by laser pulses centered at 400 nm, and fluorescence was recorded after transmission through a long-pass filter cutting light below 465 nm.

sample to hit the fiber going to the spectrometer with the reflected light. For this technique, a reference sample, e. g. a mirror of known reflectivity has to be used to calibrate the measurement. Because of the difficulty in positioning the sample at the same location as the reference, care has to be taken to obtain precise quantitative information from this measurement.

3.7 Summary and conclusions

A microspectrometer was developed for the characterization of samples used in ultrafast electron diffraction experiments. These samples typically have thicknesses of tens of nanometers and diameters of few hundreds of micrometers. A spot size below 200 µm at the sample is achieved by imaging the exit aperture of the fiber coming from the light source onto the sample and by collecting the transmitted light in a symmetric setup. In principle, the spot size can be reduced even further by using optical fibers with a smaller core diameter. The focal spot of the device was analyzed with beam camera and spectrally resolved knife-edge measurements, and no significant dependence of the focus-size and position on the wavelength was detected. In its current form, the microspectrometer has a usable wavelength range from 215 to 1030 nm but this can adapted by use of a different spectrometer and/or light source as long as the reflectivity of the protected aluminum mirrors is taken into account. The optical losses in the microspectrometer are reduced by using parabolic mirrors that are matched to the numerical aperture of the optical fibers,

resulting in an excellent detection efficiency.

The device requires very little day-to-day alignment and provides an easily adaptable experimental basis of spectroscopic measurements. In addition to the originally envisioned applications, the microspectrometer can be utilized to perform spectroscopic measurements on small crystallites even before the tedious process of sample preparation for electron diffraction has begun. It was also used successfully to record fluorescence spectra from thin films. Furthermore, it can be adapted for reflectance measurements. Last but not least, the microspectrometer can serve as a general purpose transmission spectrometer, e. g. for the characterization of optical filters in the laboratory.

4 Coherence of single-electron pulses

4.1 Introduction

In any diffraction experiment, two main requirements have to be fulfilled in order to obtain diffraction patterns of high quality. Firstly, the wavelength, which can be either a real wavelength in the case of electromagnetic radiation or a de Broglie wavelength in the case of matter wave diffraction, has to be small enough to resolve the structure of interest. Secondly, the transverse coherence length of the diffracting beam, describing the ability of laterally separated parts of the beam to interfere, must be large enough to cover the unit cell of the structure under investigation.

The first requirement is easily fulfilled in a time-resolved electron diffraction experiment. Electrons at the typical energies of 30 to 300 keV have de Broglie wavelengths of 0.07 to 0.02 Å, well below the typical interatomic distances. The second requirement, however, is more difficult to satisfy, in particular if one is interested in molecular systems in biochemistry which often haves sizes of many nanometers. This is because the small de Broglie wavelength makes it difficult to obtain a large transverse coherence ([101] and Eq. (4.1) below). In addition, in femtosecond electron pulses containing many electrons, the fermionic nature of the electrons as well as the Coulomb repulsion between them limit the transverse coherence [7, 59, 101].

In an electron microscope the transverse coherence length at the sample is routinely enlarged by inserting apertures which clip the beam [102]. This, however, is not an option for electron diffraction experiments at the ultimate temporal resolutions because it will either reduce the electron flux or negatively affect the temporal resolution if the loss in electron flux is compensated by resorting to an increased number of electrons per pulse resulting in Coulomb broadening.

In conventional femtosecond electron diffraction experiments, where no clipping apertures are used, the values for the transverse coherence length reported so far were 2.5 nm and 3 nm for beam radii of 150 µm and 200 µm, respectively [53, 55]. This is insufficient for functional systems relevant to biology.

In the following, an experiment with femtosecond single-electron pulses is presented which demonstrates the ability of these pulses to achieve a transverse coherence length of 20 nm in a beam with a radius below 100 µm.

4.2 Experimental setup

Figure 4.1 shows the essential stages of the experiment. Laser pulses from a long-cavity titanium:sapphire oscillator [74] providing 60-fs pulses at a central wavelength of 800 nm are frequency-tripled for the generation of electrons. The repetition rate

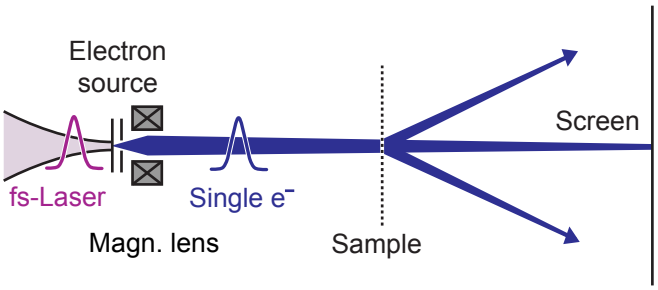

Figure 4.1: Experimental setup of the coherence experiment. Single-electron pulses are generated in a laser-triggered electron gun and are focused through the sample onto the detector screen.

of the laser is reduced from 5.12 MHz to 2.56 MHz by means of a pulse picker. The laser pulses at a wavelength of 266 nm are focused tightly onto a photocathode by using a lens with a focal length of $f = 20$ mm within the vacuum system. The photocathode consists of a sapphire substrate coated with 1 nm of chromium for adhesion and 20 nm of gold for photoemission. The exact location of the focus can be adjusted by an external lens. Assuming Gaussian beam propagation, the radius of the focal spot on the photocathode was calculated to be approximately 1 µm. This was verified with a beam camera showing an upper value for the radius of the focus of 4 µm limited by the pixel size of the detector. The laser power on the photocathode was chosen such that, on average, one tenth of an electron was emitted per laser pulse. We thus have a very low probability of producing two of more electrons with one laser pulse and stay well in the single electron regime.

The emitted electrons are accelerated in a static electric field of approximately 3.5 kV mm^{-1} to an energy of 30 keV. At this energy, the electrons have a de Broglie wavelength of 0.07 Å. The anode hole has a diameter of 2 mm and does not clip the beam. A magnetic solenoid lens is placed at a distance of 47 mm from the anode. The sample is located 456 mm after the anode. The electrons are detected with a phosphor screen and a CMOS camera with 4096 × 4096 pixels (Tietz Video and Image Processing Systems GmbH) located 474 mm after the sample. The entire electron diffraction experiment is enclosed by three coil pairs that actively compensate external magnetic distortions (Müller-BBM GmbH).

4.3 Analysis of the coherence properties

The transverse coherence length of an electron beam can be defined in analogy to optics, where it is set to be the separation of a double slit for which a diffraction pattern with a visibility of 88 percent is obtained [94, 103]. This definition is related to the van Cittert-Zernike theorem under the assumption of an incoherent source

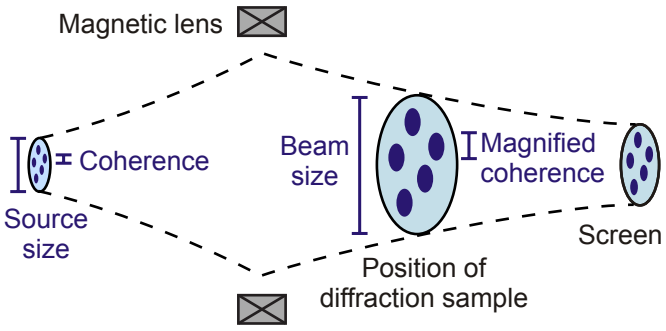

Figure 4.2: Global degree of coherence. The ratio between transverse coherence length and transverse beam size is conserved as the electron beam propagates through the electron-optical system.

[94, 103]. Accordingly, the transverse coherence width at a beam waist is defined as

$$\xi = \frac{\lambda}{2\pi\sigma_\theta}, \tag{4.1}$$

where λ is the de Broglie wavelength of the electrons [7, 55, 59, 67], $\sigma_\theta = \sigma_{v_\perp}/v_0$ is the uncorrelated angular spread (half-angle divergence) with $\sigma_{v_\perp}$ the uncorrelated transverse velocity spread and v_0 the longitudinal velocity. The transverse coherence length can be express in terms of the transverse velocity spread:

$$\xi = \frac{\hbar}{m_e\sigma_{v_\perp}}, \tag{4.2}$$

where m_e is the electron mass [53, 104]. Note that one can find differing definitions in the literature (e. g. in [103]), but the 88 % criterion expressed in Eq. (4.1) is widely accepted in the field of ultrafast electron diffraction [7, 53, 55, 104] and was applied in the case of the transverse coherence values reported above [53, 55].

Using the equations (4.1) and (4.2), one can conveniently calculate the transverse coherence length at the electron source. However, the quality of a diffraction pattern is determined by the transverse coherence length at the sample. In order to determine the coherence properties at the sample, one can make use of the global degree of coherence, the ratio between transverse coherence length and macroscopic beam size [105, 106]. This ratio is conserved as the electron beam propagates through the electron-optical system (Fig. 4.2). Knowing the transverse coherence length at the source and the beam radius at the source and at the sample we can thus calculate the transverse coherence length at the sample.

In order to determine the transverse coherence length experimentally we need to gain access to the transverse velocity spread of the electron beam at the source. To do so, we vary the current through the magnetic lens and record the electron beam

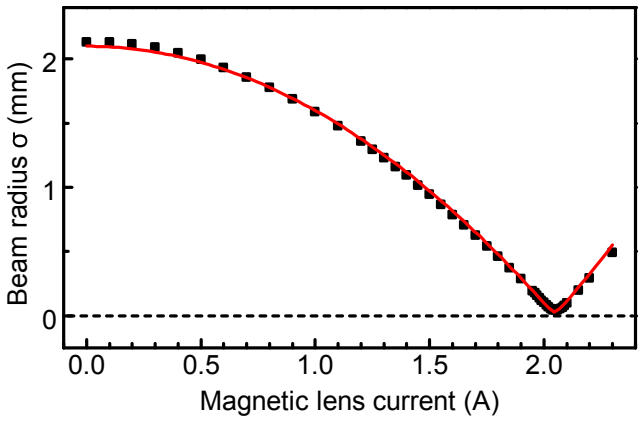

Figure 4.3: Beam radius σ on the detector as a function of the magnetic lens current. The measurement data (squares) is fitted using the transfer matrix technique yielding values for the beam radius and the transverse velocity spread at the source.

size at the detector. As detailed Sect. 2.4, we can use a least-square fit to calculate the properties of the electron beam at the source (Fig. 4.3). This analysis provides a source radius of $\sigma_{source} = (3.1 \pm 1.1)\,\mu\text{m}$, which is in good agreement with the estimates for the focal spot size given in the previous section. The transverse velocity spread at the source is determined to be $\sigma_{v_\perp} = (143.2 \pm 0.5)\,\text{km}\,\text{s}^{-1}$. These values as well as those that follow are standard deviations. The measurement uncertainties reflect the statistical errors of the fit. Systematic errors are not analyzed in detail because of the good quality of the fit. In addition, a significant increase in the uncertainty of the transverse coherence length at the sample due to systematic errors is not to be expected because this value is already dominated by the accuracy of the source radius.

Using the properties at the source of the electron beam, one can calculate the propagation of the electron beam through the electron optical system. This is shown in Fig. 4.4 for three different values of the magnetic lens current. The calculated propagation of the electron beam is verified by comparison with knife-edge measurements at the sample location and with the size of the beam on the detector.

Using Eq. (4.2), the transverse coherence length at the source is calculated to be

$$\xi_{source} = (0.792 \pm 0.003)\,\text{nm}. \tag{4.3}$$

This results in a global degree of coherence of

$$\frac{\xi_{source}}{\sigma_{source}} = (2.6 \pm 0.9) \cdot 10^{-4}. \tag{4.4}$$

The calculated beam radius at the sample for a magnetic lens current of 2.04 A is

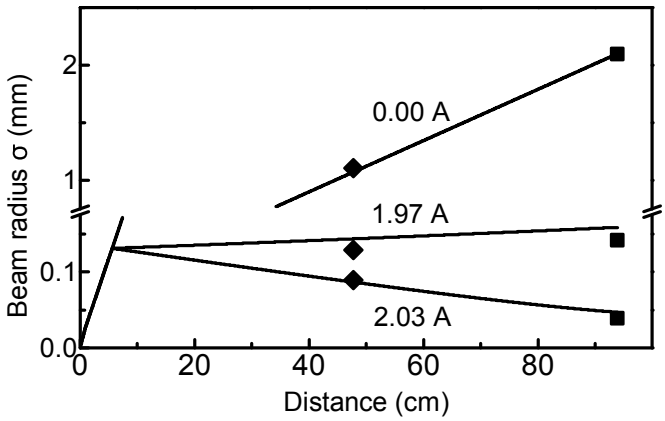

Figure 4.4: Electron beam shapes for different strengths of the magnetic lens, calculated from the fitted source parameters. For comparison, the results of knife-edge measurements at the sample position (diamonds) and the measured beam radii at the screen (squares) are shown.

$\sigma_{sample} = (77 \pm 3)\,\mu\text{m}$. Thus, we deduce a transverse coherence length of

$$\xi_{sample} = \sigma_{sample} \cdot \left(\frac{\xi_{source}}{\sigma_{source}} \right) = (20 \pm 7)\,\text{nm} \tag{4.5}$$

at the sample.

This result is about an order of magnitude larger than the values previously reported in the literature for comparable experiments. It is made possible by two main improvements, both of which are tightly linked to the single-electron regime characteristic of our experiment. First, the transverse velocity spread of the electron beam is remarkably low. This is a direct consequence of the absence of Coulomb repulsion from our electron pulses, which would normally increase the transverse velocity spread [107]. According to Eq. (4.2) this increases the transverse coherence length at the source. Second, the small source radius of the electron beam effectively increases the global degree of coherence (Eq. (4.4)). This minimization of the emission area is not possible for electron pulses containing larger numbers of electrons because image charge effects pull them back into the emission surface [26, 104].

It is noteworthy that the transverse coherence length can have arbitrarily large values if the electron beam size is enlarged accordingly. This is the idea behind the clipping apertures in an electron microscope. However, even without actual apertures in the beam path the electron flux contributing to a diffraction image will be reduced if the electron beam becomes larger than the sample. For many materials of interest the achievable dimensions of samples prepared for an electron diffraction experiment are limited. Thus, a discussion of the transverse coherence length without a mention of the beam diameter is incomplete. The decisive parameter for

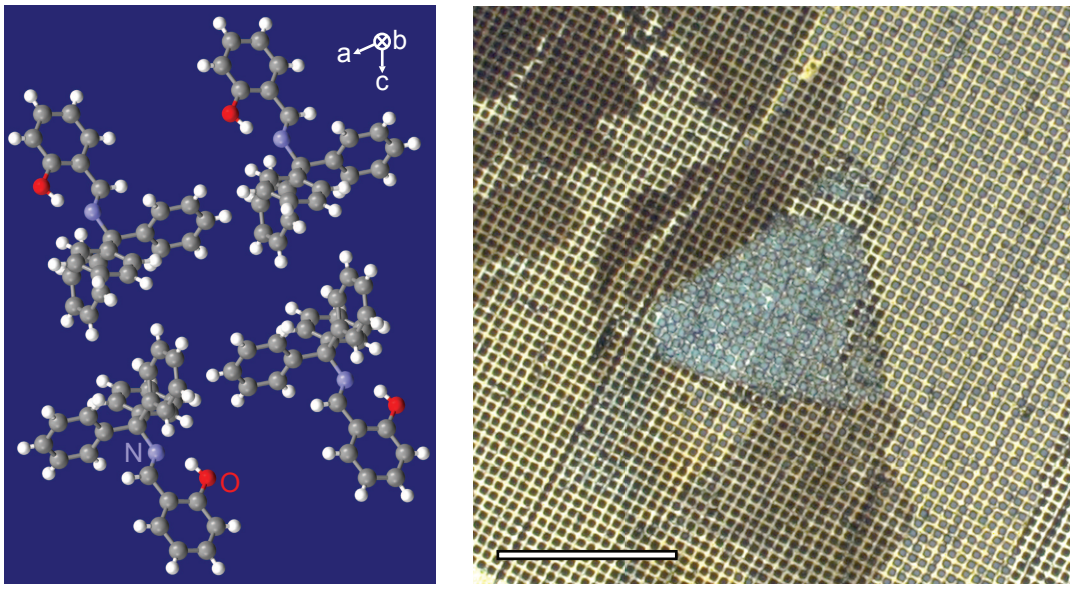

(a) **(b)**

Figure 4.5: Sample for the diffraction experiment: N-(triphenylmethyl)-salicylidenimine. (a) Molecular structure. (b) Free-standing film with a thickness of 50 nm supported by a gold mesh (scale bar: 200 µm).

practical experiments is in fact the global degree of coherence.

4.4 Diffraction images of a complex molecular crystal

In the previous section, the coherence properties of the electron beam in the presented ultrafast electron diffraction experiment were calculated from the electron beam parameters. This well established but rather indirect approach led to a transverse coherence length of $\xi_{sample} = (20 \pm 7)$ nm at the sample for a beam radius of (77 ± 3) µm. In order to verify this number, a diffraction experiment is performed using N-(triphenylmethyl)-salicylidenimine [100] (Fig. 4.5a) as the sample. From a single crystal of this material, which is embedded in epoxy resin, 50 nm thick films are produced by ultramicrotomy[1]. These free-standing and entirely single-crystalline films are supported by gold transmission electron microscopy meshes with 2000 lines per inch and are slightly larger than the electron beam (Fig. 4.5b). N-(triphenylmethyl)-salicylidenimine has a triclinic crystal structure with lattice parameters of $a = 0.902$ nm, $b = 1.090$ nm and $c = 1.107$ nm, as well as $\alpha = 77.33°$, $\beta = 68.14°$ and $\gamma = 87.08°$.

[1]The single crystal and corresponding x-ray data were provided by Aleksandra Lewanowicz from Wrocław University of Technology, and ultramicrotomy was performed by Stefan Lahme.

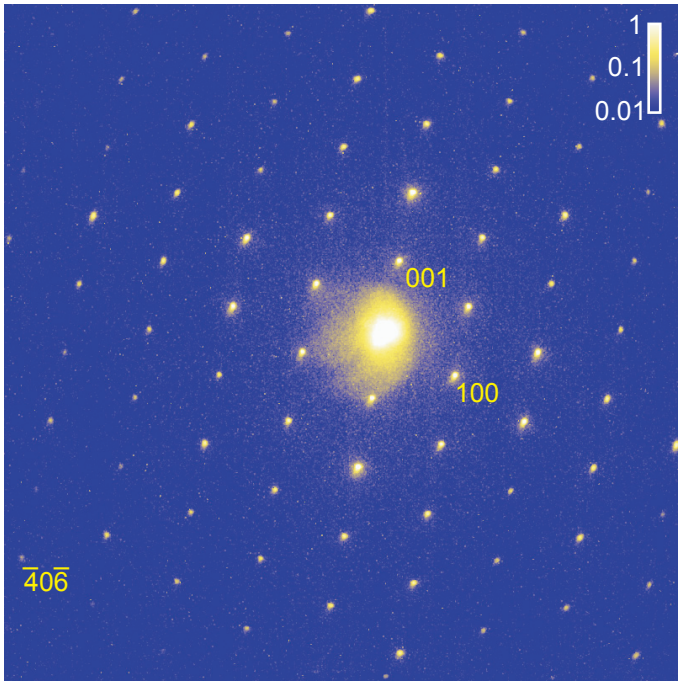

Figure 4.6: Diffraction image from N-(triphenylmethyl)-salicylidenimine recorded with a sequence of single-electron pulses. The sharpness of the spots evidences the high transverse coherence of the electron beam.

Figure 4.6 shows a diffraction pattern acquired from N-(triphenylmethyl)-salicylidenimine by integrating over approximately 10^9 laser shots (approximately 10^8 incident electrons) over a period of 5 min. 85 Bragg spots can be identified with intensities spanning two orders of magnitude. The sharpness of the diffraction spots, i. e. the ratio between their width and their separation, indicates that scattering from a significant number of adjacent unit cells must have contributed coherently to the diffraction pattern [94, 106]. For 50 Bragg spots, the σ-widths in the [001] and [100] directions were evaluated. All spots, including the central one, have comparable widths with average values of $\sigma_{001} = (76 \pm 13)\,\mu\text{m}$ and $\sigma_{100} = (68 \pm 10)\,\mu\text{m}$. The separation between the neighboring spots in the [001] and [100] directions is $s_{001} = (3226 \pm 6)\,\mu\text{m}$ and $s_{100} = (3841 \pm 3)\,\mu\text{m}$, respectively. These numbers can be compared with diffraction patterns calculated from the theory of multi-slit interference [94]. Sharpness values similar to the measured ones are obtained for 15 ± 3 and 21 ± 3 coherently illuminated slits in the [001] and [100] directions, respectively. Taking into account the spacings of the lattice planes of the crystal, $d_{(001)} = 1.00\,\text{nm}$ and $d_{(100)} = 0.84\,\text{nm}$, this leads to the conclusion that the transverse coherence of the electron beam producing the diffraction pattern spans $(15 \pm 3)\,\text{nm}$ and $(18 \pm 3)\,\text{nm}$, respectively.

It is noteworthy, that the central spot and the Bragg reflections through the molecular crystal are about 40 percent larger than the direct beam without the sample. This suggests that the sharpness of the diffraction spots is determined by the coherence of the electron beam and not by its focused spot size on the detector. Alternatively, the Bragg spots might also have been broadened by inelastic scattering, inhomogeneities of the sample or vibrations during the measurement. Therefore, the values of the transverse coherence estimated from the diffraction pattern, $(15 \pm 3)\,\text{nm}$ and $(18 \pm 3)\,\text{nm}$, represent lower limits.

4.5 Discussion and outlook

The transverse coherence length of single-electron pulses was investigated by two independent methods, the analysis of the electron beam's parameters and the sharpness of a diffraction pattern. Both measurements yielded comparable results approximately one order of magnitude larger than what had been reported in the literature for laser-triggered extended photocathode sources.

The additional optimization of the experimental setup promises a further improvement of the transverse coherence length. In the presented experiment, photoelectrons are generated by irradiation of a gold photocathode with the third harmonic of a titanium:sapphire laser. The laser's photon energy is not matched to the work function of the photocathode's material which results in photoelectrons with excess energy. This excess energy causes a broadening of the transverse velocity distribution and thus reduces the transverse coherence length of the electron pulses.

The excess energy of photoelectrons generated at metal photocathodes can be reduced by chosing a photon energy closer to the work function of the metal, e. g. by using white light generated in an yttrium/aluminum garnet (YAG) crystal with selective frequency-doubling [53]. In addition, the source size of the electron beam can be reduced further. This is possible in the single-electron regime, where no troublesome image-charge effects occur. Consequently, the global degree of coherence of the electron beam can be increased, which leads to a larger transverse coherence at the sample if an unchanged beam diameter at the sample is assumed. Using these optimizations electron beams with transverse coherence length of 100 nm for a beam diameter of 100 µm come into reach allowing the study of an even larger class of biochemical molecules.

In the described experiment, the coherence properties of the electron beam are derived from the transverse velocity spread of the beam (Eq. (4.2)). Although this technique is well established in the literature, it might lead to an underestimation of the transverse coherence of the electron pulses forming the beam. This would be the case if the beam's divergence was not caused exclusively by the inherent transverse velocity spread of the single-electron pulses but rather resulted from an inhomogeneous broadening of the emission directions on an uneven surface [108, 109]. For instance, Cho *et al.* [110] reported on field emitter sources with a transverse coherence exceeding the predictions from the beam propagation. They suggested that this was related to the delocalization of the initial electronic states in the material which were preserved during tunneling in field emission. Similarly, photoelectric emission was reported to directly promote the initial electronic states into vacuum [111, 112]. Taking into account these two observations, it seems plausible that photo-emitted electron pulses could have a higher transverse coherence than determined from beam parameter measurements, depending on the purity, temperature and morphology of the cathode material. A detailed study of this suggestion will, however, require tools that are more sophisticated than the analysis of crystalline diffraction patterns. These techniques could, for example, be based on electron interferometry [110, 113].

Recently, alternative sources of highly coherent electron pulses were investigated. One unconventional approach for the generation for high coherence electron bunches is the use of a cold atom source [104, 114]. In a magneto-optical trap, neutral rubidium-85 atoms are laser-cooled to milli-kelvin temperatures, i. e. very low kinetic energies. The trap is then switched off, and the atoms are excited by a near-infrared laser and subsequently ionized by a laser pulse in the visible spectral range. This results in a source temperature of few kelvins, corresponding to a very low transverse velocity spread and thus a large transverse coherence. Transverse coherence lengths at the source of up to 10 nm have been reported [115, 116]. However, the source size is comparably large in these experiments (tens of microns) because their goal is to produce electron pulses for single-shot diffraction experiments. Thus, for these high electron numbers image-charge effects at the source must be avoided. An extended beam size with lower electron density is also favored in order to avoid distortions of

the electron pulses by Coulomb repulsion [117]. Using cold atom electron sources, a transverse global degree of coherence of $2 \cdot 10^{-4}$ was demonstrated [117].

The biggest drawback of cold atom electron sources is the duration of the produced electron pulses. Typically, microsecond and nanosecond laser pulses are applied for excitation and ionization of the cold atoms, respectively, and some efforts have been undertaken to reduce the electron pulse duration [118] but the picosecond regime was not easily accessible. Only recently, the use of femtosecond lasers enabled the generation of electron pulses with estimated durations down to 25 ps [119, 120]. The temporal profile of the produced electron pulses is determined by the extended spatial region in which atoms are ionized. This leads to a longitudinal energy spread due to the acceleration field. In addition, the potential caused by the rubidium ions left behind after photoionization broadens the electron pulse [120]. It is envisioned that the longitudinal and transverse broadening of the electron pulses can be reversed by microwave compression techniques [64, 65, 67], particularly if one makes use of properly shaped emission areas that support such compression [121–123]. Due to the extended source sizes this becomes easily possible by using a spatial light modulator [115]. Because the magneto-optical trap has to be reloaded after every electron pulse, the repetition rate of cold atom electron sources is limited, a typical repetition rate being 10 Hz [119]. However, this is not overly critical for the envisioned single-shot experiments. At the present stage, cold atom electron sources represent a promising new technique for the generation of electron pulses for time-resolved diffraction experiments. Electron pulses from cold atom sources provide a remarkable transverse coherence at the level of what has been presented in the present work but at the same time comprise orders of magnitude more electrons. So far, however, the temporal resolution is very limited and pulse compression remains to be demonstrated. In addition, the experimental complexity is high because experimental techniques from different fields, cold atom and accelerator physics, are combined.

A different method for producing highly coherent and ultrafast electron pulses is based on metallic nanotips [124, 125]. Upon irradiation by a pulsed laser, these tips can produce ultrashort electron pulses from emission areas down to few square nanometers [126–128]. In addition to profiting from these very small source sizes, nanotip sources operating in the field emission regime, thus producing DC electron beams, were reported to have a transverse coherence length in the range of 5 to 35 nm [110][2]. In the case of metal covered single-atom emitters they can even produce fully coherent beams [129]. This gives rise to the expectation that similar coherences can be achieved in laser-triggered sources. Despite these apparent advantages, the application of nanotip sources in a diffraction experiment at keV energies remains challenging. The strong curvature of the emission area causes a large divergence of the electron beam and the inhomogeneous acceleration field

[2]Note that in [110] a different visibility criterion is used in the definition of the coherence length. This makes the comparison with the experiment presented in this work difficult.

at the tip deteriorates the electron pulse duration. Consequently, a sophisticated electron-optical design is necessary to deliver femtosecond electron pulses from nanotip sources to the diffraction sample [125]. These experimental difficulties related to nanotip electron sources are intrinsically absent from the flat, extended emitters used in the present work.

In conclusion, femtosecond electron pulses from a flat metal photocathode with a transverse coherence length of approximately 20 nm at a beam radius of 77 µm were demonstrated experimentally. The decisive steps in this improvement were the reduction of the transverse velocity spread of the electrons at the source and the minimization of the source area, both of which are enabled by the reduction of the number of electrons per pulse to one. The further optimization of the mentioned parameters suggests that transverse coherence lengths in the range of 100 nm can be realized in electron beams with realistic dimensions. Our experimental results show that femtosecond electron diffraction with single-electron pulses is a suitable technique for the investigation of biochemical samples.

5 Streaking of keV femtosecond electron pulses

5.1 Introduction

Mapping temporal information into energy information, so-called streaking, has been a fundamental technique in the study of fast and ultrafast processes (for examples, see [130–134]). Typically, quickly varying electric fields with known temporal characteristics are used to gain information about the temporal properties of an electron pulse. The temporal resolution of the streaking technique is determined, inter alia, by the rate of change of the electric field that accelerates the electrons. In recent years, the electric field of an ultrashort laser pulse has been used for this purpose, thus advancing the streaking technique to a new regime. Apart from the generation of sub-femtosecond light pulses in the extreme ultraviolet spectral range by high-harmonic generation [135–138], the attosecond streak camera [71, 139] has been the enabling technology for the new field of attosecond physics.

In an attosecond streak camera, attosecond photon pulses are used to release a bound electron from a sample. The presence of an additional, controlled laser field at the moment of photoemission leads to an energy gain or loss of the emitted electron depending on the instantaneous phase of the laser field at the time of emission. This mechanism hence maps temporal information into energy shifts with attosecond resolution. Attosecond streaking has been used to characterize the shortest pulses of light in great detail [140, 141]. Additionally, the emitted electrons contain valuable information about their origin and deep insight into the electronic properties of atoms as well as the physics of the photoemission process [139, 142, 143] was gained by attosecond streaking experiments. The electron energy in these experiments was on the order of 130 eV. Here, the extension of the laser streaking concept to free electron pulses at energies of 25 keV is presented, demonstrating field-resolved laser-electron interaction at 100-times higher energies than before.

In the attosecond streak camera, the electron is released abruptly from a bound state into the electric field of the laser pulse where it is subsequently accelerated. Streaking of free electrons builds on the same principle, but uses a different mechanism to ensure that the electron quasi-instantaneously enters the laser field: The freely-propagating electron pulse and the laser pulse are overlapped at the surface of a thin metal film that acts as a mirror for the laser light but (partially) transmits the electron pulse. Because of the high reflectivity of the metal film and the corresponding low penetration depth of the light field into the metal, the transition between field-free and field-penetrated areas is very rapid. In the experiment, a geometry is chosen where the laser and the electron pulse approach the metal film from the same

side. In this situation the electron pulse leaves the laser field abruptly. This does not change the physics of the process but ensures that the laser interacts with the unaltered, incident electron pulse instead of the attenuated one that is transmitted through the film.

5.2 Classical description of the streaking effect

In the original literature on the streaking of attosecond pulses [136], a classical, non-relativistic analysis of the streaking effect leads to a formula describing the electron's energy gain due to the interaction with a laser field of the form $E(t) = E_{laser}(t) \cdot \cos(\omega_{laser} t + \varphi)$, where $E_{laser}(t)$ is the envelope of the electric field of the laser pulse, ω_{laser} is its angular frequency and φ is its phase. Here, only the dominant contribution to the energy gain is taken into account. The field-induced energy change ΔW of an electron after streaking is given by

$$\Delta W = W_{final} - W_{initial} = \sqrt{8 \cdot W_{initial} \cdot U_p(t_d)} \cdot \cos\theta \cdot \sin(\omega_{laser} t_d + \varphi), \qquad (5.1)$$

where $W_{initial}$ and W_{final} are the electron's initial and final energy, respectively, and θ is the angle between the laser polarization and the final momentum of the electron.

$$U_p(t) = \frac{e^2 \cdot E_{laser}^2(t)}{4 \cdot m_e \cdot \omega_{laser}^2} \qquad (5.2)$$

is the so-called ponderomotive energy, the cycle-averaged quiver energy of the electron in the electric field of the laser, and e and m_e are the elementary charge and the electron's mass, respectively. t_d is the relative delay between the laser and the electron pulse.

To adapt this formula to the situation in the present experiment, two aspects are taken into account. Firstly, in the conventional attosecond streaking experiment, the electron interacts with a freely propagating laser pulse. This is not the case in the presence of a metal film reflecting the laser light. Here, the electron interacts with both the incident and the reflected fields[1]. The reflection of the incident laser pulse from the metal film results in interference between the incident and the reflected light, thus causing a change in the maximum field strength on the surface of the metal. The exact change depends on the reflectivity of the metal and the phase-shift of the light wave upon reflection, both of which depend on the angle of incidence of the light and on the optical properties of the metal.

Secondly, the electron is subject to the Lorentz force $F = -e \cdot (\vec{E} + \vec{v} \times \vec{B})$. In the conventional attosecond streaking experiment, the velocity $\vec{v}$ of the electron is

[1] To be precise, the electron also interacts with the field penetrating into the metal, but this field is much weaker than the incident field and decays rapidly. This is why the basic assumption of the analysis, the instantaneous ending of the interaction of the electron with the light, is still valid.

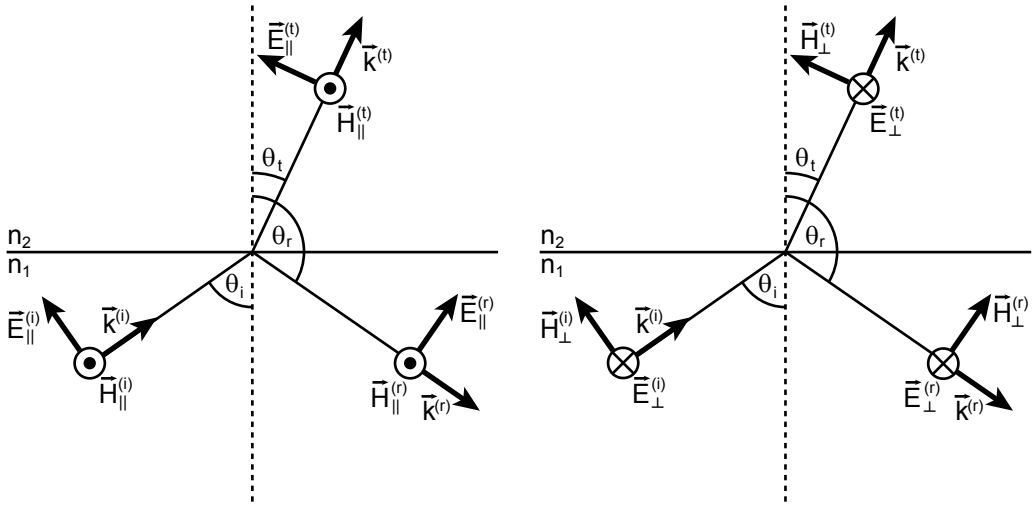

(a) p-Polarization **(b)** s-Polarization

Figure 5.1: Orientation of $\vec{E}$-, $\vec{H}$- and $\vec{k}$-vectors at an interface. The superscripts (i), (r) and (t) label the incident, reflected and transmitted waves, respectively.

small compared to the velocity of light. At 25 keV electrons travel at approximately 0.3 times the speed of light. Thus, the contribution of the magnetic field through the flux density $\vec{B}$ in the Lorentz force is no longer negligible. Therefore, it is useful to define an effective accelerating field $\vec{E}_{eff} = \vec{E} + \vec{v} \times \vec{B}$, which can be used in Eq. (5.1) to calculate the energy gain of the electron due to the interaction with the laser pulse.

5.3 Light at interfaces

As mentioned in the previous section, a detailed, quantitative understanding of the behavior of light at a planar metal surface is required to model the streaking effect for free electrons. This becomes even more important in the numerical simulation of the interaction between an electron and a laser pulse at a metal surface, which is discussed in the subsequent section. The following derivations are adapted from the textbooks by Born and Wolf [94] and by Fowles [144].

5.3.1 Plane wave at an interface

When a plane wave hits an interface between two non-absorbing materials, it is partially reflected and partially transmitted into the second medium (Fig. 5.1). The

space-time dependence of these three waves can be described as follows:

$$\text{(incident wave)} \quad \exp[i(\vec{k}^{(i)}\vec{r} - \omega t)], \tag{5.3}$$

$$\text{(reflected wave)} \quad \exp[i(\vec{k}^{(r)}\vec{r} - \omega t)], \tag{5.4}$$

$$\text{(transmitted wave)} \quad \exp[i(\vec{k}^{(t)}\vec{r} - \omega t)]. \tag{5.5}$$

It is necessary to maintain a constant relationship between these quantities for all points $\vec{r}$ at the interface and for all times t:

$$\vec{k}^{(i)}\vec{r} - \omega t = \vec{k}^{(r)}\vec{r} - \omega t = \vec{k}^{(t)}\vec{r} - \omega t. \tag{5.6}$$

The common time-dependence is fulfilled, leaving

$$\vec{k}^{(i)}\vec{r} = \vec{k}^{(r)}\vec{r} = \vec{k}^{(t)}\vec{r} \tag{5.7}$$

for all $\vec{r}$ in the boundary. This can only be fulfilled, if $\vec{k}^{(i)}$, $\vec{k}^{(r)}$ and $\vec{k}^{(t)}$ are in the same plane (plane of incidence).

$$k^{(i)} \sin\theta_i = k^{(r)} \sin\theta_r = k^{(t)} \sin\theta_t \tag{5.8}$$

Since $k^{(i)} = wn_1/c = k^{(r)}$ (same medium), the angle of incidence equals the angle of reflection:

$$\theta_r = \pi - \theta_i \quad \text{(law of reflection)}. \tag{5.9}$$

Using a similar argument for the transmitted wave, the following equation can be obtained:

$$n_1 \sin\theta_i = n_2 \sin\theta_t \quad \text{(Snell's law)}. \tag{5.10}$$

5.3.2 Amplitudes of reflected and transmitted waves

After these general discussions, the amplitudes of an electromagnetic wave at the interface between two non-magnetic media are considered. From Maxwell's equations one can derive boundary conditions for the components of the electric and magnetic fields at the interface. When no surface current is present, the tangential components of the electric field $\vec{E}$ and the magnetic field $\vec{H}$ are continuous. Using the relation $\vec{H} = (1/(\mu_0\omega))\vec{k} \times \vec{E}$ and thus $H = (1/\mu_0)(n/c)E$, the conditions of continuity can be expressed in terms of the amplitudes of the electric fields. For p-polarization,

$$E_{\parallel}^{(i)} \cos\theta_i + E_{\parallel}^{(r)} \cos\theta_r = E_{\parallel}^{(t)} \cos\theta_t, \tag{5.11a}$$

$$n_1 E_{\parallel}^{(i)} + n_1 E_{\parallel}^{(r)} = n_2 E_{\parallel}^{(t)}. \tag{5.11b}$$

For s-polarization,

$$n_1 E_\perp^{(i)} \cos\theta_i + n_1 E_\perp^{(r)} \cos\theta_r = n_2 E_\perp^{(t)} \cos\theta_t, \tag{5.12a}$$

$$E_\perp^{(i)} + E_\perp^{(r)} = E_\perp^{(t)}. \tag{5.12b}$$

The equation sets (5.11) and (5.12) can be used to calculate the relation between incident, the reflected and the transmitted amplitudes. For p-polarization, one obtains

$$\frac{E_\parallel^{(r)}}{E_\parallel^{(i)}} = \frac{n_2 \cos\theta_i - n_1 \cos\theta_t}{n_2 \cos\theta_i + n_1 \cos\theta_t}, \tag{5.13a}$$

$$\frac{E_\parallel^{(t)}}{E_\parallel^{(i)}} = \frac{2 n_1 \cos\theta_i}{n_2 \cos\theta_i + n_1 \cos\theta_t}. \tag{5.13b}$$

Similarly, for s-polarization,

$$\frac{E_\perp^{(r)}}{E_\perp^{(i)}} = \frac{n_1 \cos\theta_i - n_2 \cos\theta_t}{n_1 \cos\theta_i + n_2 \cos\theta_t}, \tag{5.14a}$$

$$\frac{E_\perp^{(t)}}{E_\perp^{(i)}} = \frac{2 n_1 \cos\theta_i}{n_1 \cos\theta_i + n_2 \cos\theta_t}. \tag{5.14b}$$

The equation sets (5.13) and (5.14) are the well-known Fresnel equations. In their form given above, they contain only real quantities. This is why the reflected field can only experience a phase shift of 0 or π. This situation changes dramatically when a material exhibiting absorption is considered.

5.3.3 Reflection and refraction at the boundary of an absorbing medium

In the following, a medium with a complex refractive index $N = n(1 + i\kappa)$ is considered, i. e. one that shows absorption[2]. Here, κ is called the attenuation index. This complex index of refraction is connected to the complex dielectric function $\epsilon = \epsilon_1 + i\epsilon_2$ of the material. For many metals, values of the frequency-dependent dielectric function can be found in [145]. The relationship between the complex dielectric function and the complex refractive index is as follows:

$$n = \frac{1}{\sqrt{2}} \left((\epsilon_1^2 + \epsilon_2^2)^{1/2} + \epsilon_1 \right)^{1/2}, \tag{5.15a}$$

$$n\kappa = \frac{1}{\sqrt{2}} \left((\epsilon_1^2 + \epsilon_2^2)^{1/2} - \epsilon_1 \right)^{1/2}. \tag{5.15b}$$

[2] In the literature, there is frequently a different definition of the complex refractive index: $N = n + i\kappa$.

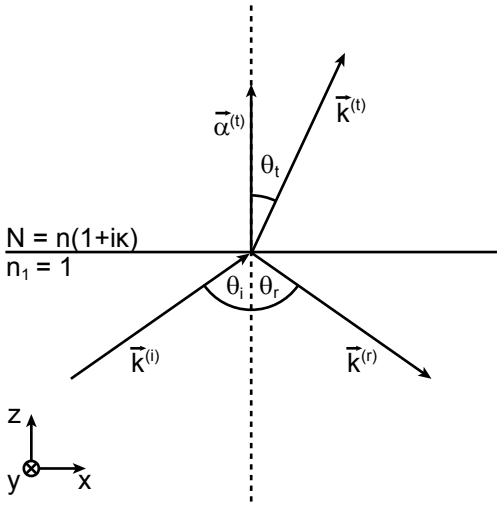

Figure 5.2: Light at an interface between vacuum and an absorbing medium

The complex refractive index results in a complex wave-vector $\vec{K} = \vec{k} + i\vec{\alpha}$. Considering, as above, the spatiotemporal properties of a plane wave at an interface,

$$\text{(incident wave)} \qquad \exp[i(\vec{k}^{(i)}\vec{r} - \omega t)], \tag{5.16}$$

$$\text{(transmitted wave)} \quad \exp[i(\vec{K}^{(t)}\vec{r} - \omega t)] = \exp(-\vec{\alpha}^{(t)}\vec{r})\exp[i(\vec{k}^{(t)}\vec{r} - \omega t)], \tag{5.17}$$

they need to match for all times t and all points $\vec{r}$ at the interface. Equating real and imaginary parts individually, one obtains

$$\vec{k}^{(t)}\vec{r} = \vec{k}^{(i)}\vec{r}, \tag{5.18}$$

$$\vec{\alpha}^{(t)}\vec{r} = 0. \tag{5.19}$$

Eq. (5.18) resembles the familiar Snell's law. Eq. (5.19) indicates that $\vec{\alpha}^{(t)}$ is normal to the interface and thus planes of constant amplitude of the transmitted field are parallel to the surface of the medium. Consequently, the vectors $\vec{\alpha}^{(t)}$ and $\vec{k}^{(t)}$ generally point in different directions, creating an inhomogeneous wave within the medium. The amplitude of the wavevector $k^{(t)}$ is a function of the angle θ_t between $\vec{k}^{(t)}$ and $\vec{\alpha}^{(t)}$.

In the following, the interface between vacuum and an absorbing medium is considered, representing the situation in the experiment. This is depicted in Fig. 5.2. For absorbing media, quantities like the refractive index, the wavevector or the dielectric constant were shown to be complex. Nevertheless, the relationships discussed in Sect. 5.3.1 are still valid if one pays attention to the complex nature of certain quantities. From Eq. (5.10), one obtains

$$\sin\Theta_t = (1/N)\sin\theta_i = \frac{\sin\theta_i}{n(1+i\kappa)}. \tag{5.20}$$

Since N is a complex quantity, so is Θ_t. It can thus no longer be directly identified with the direction of light propagation within the medium. For convenience, $\cos\Theta_t$ is expressed in terms of the real variables q and γ:

$$\cos\Theta_t = \sqrt{1-\sin^2\Theta_t} = qe^{i\gamma}. \tag{5.21}$$

In order to determine the propagation direction of the light in the medium, the spatially varying part of the wave $\exp\left[i(\vec{K}^{(t)}\vec{r}-\omega t)\right]$ is considered:

$$\begin{aligned}\vec{K}^{(t)}\cdot\vec{r} &= \frac{\omega}{c}n(1+i\kappa)(x\sin\Theta_t + z\cos\Theta_t)\\ &= \frac{\omega}{c}\left[x\sin\theta_i + znq(\cos\gamma-\kappa\sin\gamma) + inzq(\kappa\cos\gamma+\sin\gamma)\right].\end{aligned} \tag{5.22}$$

This equation allows to determine the propagation direction of the transmitted light wave and establishes the connection between $\vec{k}^{(t)}$ and $\vec{\alpha}^{(t)}$.

$$\vec{k}^{(t)} = \frac{\omega}{c}\begin{pmatrix}\sin\theta_i\\ 0\\ nq(\cos\gamma-\kappa\sin\gamma)\end{pmatrix} \tag{5.23}$$

$$\vec{\alpha}^{(t)} = \frac{\omega}{c}\begin{pmatrix}0\\ 0\\ nq(\kappa\cos\gamma+\sin\gamma)\end{pmatrix} \tag{5.24}$$

As seen above, the planes of constant amplitude of the transmitted field are parallel to the interface whereas the planes of constant phase make an angle θ_t with the normal to the interface:

$$\sin\theta_t = \frac{\sin\theta_i}{\sqrt{\sin^2\theta_i + n^2q^2(\cos\gamma-\kappa\sin\gamma)^2}}.$$

As far as the amplitudes of the reflected and transmitted waves are concerned, it is convenient to make use of the analogy with the Fresnel equations (5.13) and (5.14). Considering the interface between vacuum and an absorbing medium, one obtains for p-polarization:

$$\frac{E_\parallel^{(r)}}{E_\parallel^{(i)}} = \frac{N\cos\theta_i - \cos\Theta_t}{N\cos\theta_i + \cos\Theta_t}, \tag{5.25a}$$

$$\frac{E_\parallel^{(t)}}{E_\parallel^{(i)}} = \frac{2\cos\theta_i}{N\cos\theta_i + \cos\Theta_t}. \tag{5.25b}$$

For s-polarization, the relationships are

$$\frac{E_\perp^{(r)}}{E_\perp^{(i)}} = \frac{\cos\theta_i - N\cos\Theta_t}{\cos\theta_i + N\cos\Theta_t}, \tag{5.26a}$$

$$\frac{E_\perp^{(t)}}{E_\perp^{(i)}} = \frac{2\cos\theta_i}{\cos\theta_i + N\cos\Theta_t}. \tag{5.26b}$$

Here again, it is important to take note of the complex nature of capitalized quantities.

The equations derived above allow to calculate the behavior of a plane light wave as it hits the interface to an absorbing medium. The Fresnel equations (5.25) and (5.26) can be used to calculate the amplitude and phase relationships between the reflected and the incident or the transmitted and the incident wave, respectively. They can thus be utilized to calculate the effective field at the surface of the metal film as discussed in Sect. 5.2. In addition, the knowledge of the electromagnetic field at the surface of a metal film is important for the numerical simulation of the streaking effect, which is discussed in the following section.

5.4 Numerical simulation

To model the interaction between an electron and the electromagnetic wave of the laser pulse at the surface of the aluminum film, the initial value problem for the relativistic equations of motion[3] of the electron is solved numerically:

$$\frac{d}{dt}\vec{p}(t) = \vec{F}(\vec{x},\vec{v},t), \tag{5.27}$$

$$\frac{d}{dt}\vec{x}(t) = \vec{v}(t) = \frac{\vec{p}(t)c}{\sqrt{(p(t))^2 + m^2c^2}}, \tag{5.28}$$

$$\vec{x}(t_0) = \vec{x}_0, \tag{5.29}$$

$$\vec{p}(t_0) = \vec{p}_0, \tag{5.30}$$

where the accelerating force $\vec{F}$ is the Lorentz force

$$\vec{F}(\vec{x},\vec{v},t) = -e\left(\vec{E}(\vec{x},t) + \vec{v}(t)\times\vec{B}(\vec{x},t)\right). \tag{5.31}$$

Here, $\vec{x}$ and $\vec{p}$ denote the position and the momentum of the electron, respectively, and $\vec{x}_0$ and $\vec{p}_0$ are the initial values at time t_0. The momentum $\vec{p}$ and the velocity

[3] Although relativistic effects only contribute a minor correction for electrons at 25 keVand are thus usually neglected, they are included here in order to use as few approximations as possible. In addition, the developed code for solving the initial value problem can be adapted easily for higher electron energies where relativistic effects become more significant.

$\vec{v}$ of the electron are connected by $\vec{p} = \gamma m \vec{v}$, with $\gamma = (1 - v^2/c^2)^{-1/2}$. The fields $\vec{E}$ and $\vec{B}$ in Eq. (5.31) are determined as discussed in Sect. 5.3 taking into account the incident, reflected and transmitted fields as well as the optical properties of the aluminum film.

The solution of the initial value problem is calculated using a second-order Runge-Kutta method [146]. In this algorithm, the time is discretized and starting from the initial values, the solution for the vectors $\vec{x}$ and $\vec{p}$ is advanced from time-step to time-step, where the time-steps are separated by τ. For each time-step t_n, a first approximation of the position $\vec{x}_a$ and the momentum $\vec{p}_a$ at the following time-step is calculated using the velocity and force present at $\vec{x}_n$ and t_n, $\vec{F}_n = -e\left(\vec{E}(\vec{x}_n, t_n) + \vec{v}_n \times \vec{B}(\vec{x}_n, t_n)\right)$:

$$\vec{x}_a = \vec{x}_n + \tau \cdot \vec{v}_n, \tag{5.32}$$

$$\vec{p}_a = \vec{p}_n + \tau \cdot \vec{F}_n, \tag{5.33}$$

$$\vec{v}_a = \frac{\vec{p}_a c}{\sqrt{p_a^2 + m^2 c^2}}. \tag{5.34}$$

Using these approximate values, an approximate force $\vec{F}_a$ at the following time-step is calculated, $\vec{F}_a = -e\left(\vec{E}(\vec{x}_a, t_n + \tau) + \vec{v}_a \times \vec{B}(\vec{x}_a, t_n + \tau)\right)$. The actual propagation to the next time-step then uses velocity and force values that are the averages between the present time-step and the approximate values for the following time-step:

$$\vec{x}_{n+1} = \vec{x}_n + \tau \cdot \frac{1}{2}(\vec{v}_n + \vec{v}_a), \tag{5.35}$$

$$\vec{p}_{n+1} = \vec{p}_n + \tau \cdot \frac{1}{2}(\vec{F}_n + \vec{F}_a). \tag{5.36}$$

As detailed in [146], this midpoint method has an error of order $\mathcal{O}(\tau^3)$.

In order to avoid the accumulation of errors in the final result, the step size τ has to be chosen carefully. The choice of an appropriate step size τ can be simplified by a numerical experiment. The same initial value problem is solved for different step sizes τ. The final results for the vectors $\vec{x}$ and $\vec{v}$ after the same total propagation time can then be compared. As seen in Fig. 5.3 the values converge for $\tau \leq 10^{-18}\,\mathrm{s}$. This result is obtained for a geometry and laser parameters as used in the experiment. Consequently, $\tau = 10^{-18}\,\mathrm{s}$ is chosen as the time-step for the simulations.

The electromagnetic field in the simulation is set to resemble the ultrashort laser pulses in the experiment. Based on the plane waves discussed in detail in Sect. 5.3, short pulses are modeled by multiplication with Gaussian spatial and temporal profiles. In accordance with the situation in the experiment, a pulse duration of 50 fs (full width at half maximum of the intensity profile) is chosen. The beam profile is set to have a diameter of 54.8 µm (full width at half maximum of the intensity) which

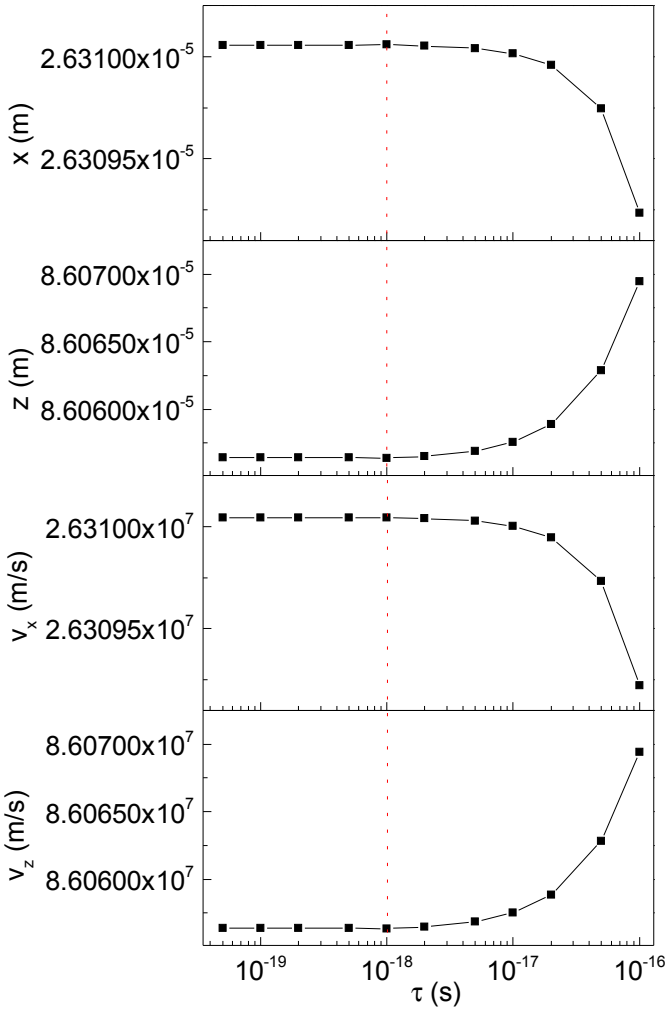

Figure 5.3: Step-size dependence of simulation results. The step size τ in the second-order Runge-Kutta method is varied in order to determine the convergence of the simulation results. For $\tau \leq 10^{-18}$ s the fluctuations in the calculated values for position and velocity are negligible and thus $\tau = 10^{-18}$ s is chosen as a step size for the subsequent simulations.

is the geometric mean of the major and minor axis diameters of the slightly elliptical focus observed in the experiment. Multiplying a plane wave with a Gaussian spatio-temporal profile is an approximation to the pulsed Gaussian light beam [147]. This approximation, however, does not create a large error because of the large waist of the laser beam. The Gaussian beam present in the experiment has a Rayleigh range of $z_0 = 8.5\,\mathrm{mm}$. This means that the beam radius changes by a factor of 1.0002 over a range of $\pm 150\,\mu\mathrm{m}$ around the focus, corresponding to the interaction region between laser and electron pulse. Similarly, the radius of curvature of the phase fronts changes from infinity at the focus to 0.482 m at a location 150 µm before or after the focus. The change in Gouy phase is also negligible in a $\pm 150\,\mu\mathrm{m}$ region around the focus ($\pm 18\,\mathrm{mrad}$). Thus, it is reasonable to approximate the laser pulse in the interaction region as a plane wave modulated by a Gaussian profile.

The simulation takes into account the reflection of the laser pulse at the surface as well as the penetration of the light into the material. Because of the low penetration depth of the light into the material, 15 nm, the thickness of the aluminum film is neglected and the metal extends into the half space. The interaction of the electron with the aluminum film is not taken into account. No scattering or absorption of electrons within the material is considered.

For the simulation the geometry is chosen in agreement with the experiment. The angle of incidence of the laser pulse on the surface of the aluminum film is 77° and the angle of the electron beam with the normal of the film's surface is 17°. In this situation velocity matching between the electron beam and the phase fronts of the laser field is achieved (see Sect. 2.6).

In the simulation the laser pulse is set up such that its center arrives at the center of the metal surface at $t = 0\,\mathrm{fs}$. The electron has an initial velocity of $0.3\,c$ and can be started with a delay with respect to the laser pulse. If no delay is chosen, the electron is initialized in a way that it arrives at the center of the vacuum-metal interface at $t = 0\,\mathrm{fs}$ in case of no interaction with the laser. The calculation of the trajectory of the electron starts at $t = -2\,\mathrm{ps}$ and ends at $t = 1\,\mathrm{ps}$, such that the Lorentz force (Eq. (5.31)) is negligible at the start and at the end of the simulation time window.

Fig. 5.4 shows the result of the numerical simulation for a peak electric field of the incident laser pulse of $1.25 \cdot 10^9\,\mathrm{V\,m^{-1}}$. The final velocity of the electron is plotted as a function of the delay between the laser pulse and the electron. The velocity gain shows an oscillatory behavior with a period equal to the period of the field oscillations of the laser pulse. The maximum velocity gain occurs at a delay of 0.5 fs instead of being shifted by a quarter period (0.7 fs) from zero delay as suggested by Eq. (5.1). This is indicative of the phase shift that occurs upon reflection of the laser pulse on the metal surface, highlighting the necessity of taking the incident as well as the reflected fields into account. The electron experiences a maximum velocity gain of $\Delta v = 131\,\mathrm{km\,s^{-1}}$ corresponding to an energy gain of $\Delta W = 77.2\,\mathrm{eV}$.

The dotted line in Fig. 5.4 is an overlay of the temporal envelope of the electric

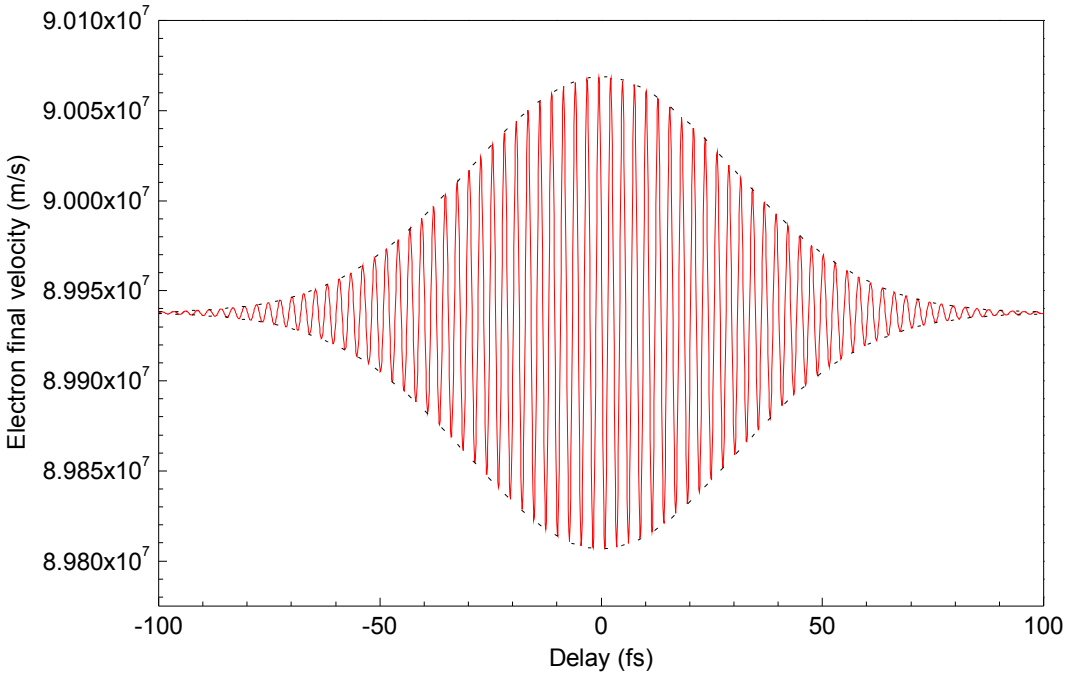

Figure 5.4: Result of the simulation. The final velocity of the electron after the interaction with the laser pulse oscillates with the same period as the laser's field. The maximum energy gain is 77.2 eV. For comparison, the dotted line is an overlay of the temporal profile of the electric field of the laser pulse. It agrees with the envelope of the final velocity of the electron, indicating that the acceleration effect is linear in the electric field.

field of the laser pulse used for the calculation. It nicely matches the envelope of the final electron energy curve. This confirms that the observed acceleration effect is linear in the electric field.

The above results indicate that the streaking technique can be adapted to electrons at an energy of 25 keV. The energy gain of the electrons follows the oscillations of the laser field thus providing the tools for the characterization of electron pulses with durations below the laser's period, i. e. in the low-femtosecond or even attosecond range.

In the above simulation, only a single electron on a central trajectory is considered in contrast to the experiment, where a spatially extended electron beam is found. Due to the employed velocity matching geometry (see Sect. 2.6) the delay between the laser phase fronts and the electron pulse does not vary across the surface of the aluminum film. Thus, the temporal resolution of the technique is not reduced by the velocity mismatch.

However, since the size of the electron beam in the experiment is larger than the laser spot, the different parts of the electron beam interact with laser fields of different strengths. Since the observed energy gain is proportional to the laser field strength, this means that for a certain delay value the electron energy gain ranges from zero for electrons outside of the spot size of the laser to the maximum value as determined in the simulation. In this case, the streaking effect can still be used to characterize an electron pulse with a duration much shorter than the laser oscillation period: When the delay is set close to a zero-crossing of the energy gain, the electron pulse duration is encoded in the span between energy gain and the energy loss. Alternatively, the size of the electron beam can be reduced by using a pinhole, or the size of the laser beam can be enlarged.

The electron pulses in the present experiment have a duration significantly longer than the laser pulses. In addition, the laser pulses are not phase stabilized. This means that the temporal oscillations visible in Fig. 5.4 will not be observable. We thus expect an energy gain feature that is smeared out in the energy direction and in the delay direction. Despite this apparent loss of information, the delay-time dependence of the energy spectra of the spatially extended electron beam provides a temporal cross-correlation of the electron pulse and the laser pulse, the details of which will be discussed in the context of the experimental data.

5.5 Experimental realization

5.5.1 Experimental setup

The central part of the experimental setup is depicted in Fig. 5.5. The laser system used for the experiments is described in Sect. 2.1. Using the pulse picker, the repetition rate of the laser is reduced to 128 kHz, thus avoiding damage to the alu-

minum film. In order to achieve synchronization between the electron pulses and the streaking laser pulses, both pulses are derived from the same pulse train by means of a beam splitter. The details of the electron generation are discussed in Sect. 2.2. Here, we use the third harmonic of the titanium:sapphire laser to generate the electron pulses which are accelerated to 25 keV over a distance of 3 mm. The magnetic

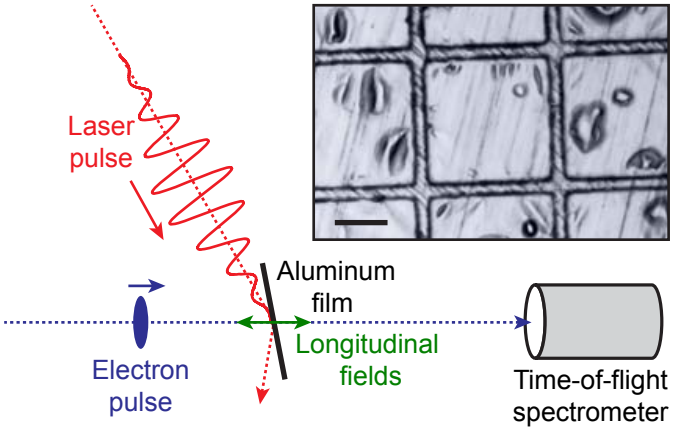

Figure 5.5: Experimental setup of the streaking experiment. The laser is incident under a shallow angle on the aluminum film, where the longitudinal fields accelerate the electron pulse. Changes in the electron energy are recorded with a time-of-flight spectrometer. The freestanding aluminum film has a thickness of 50 nm and is mounted on a supporting grid (inset, scale bar: 100 µm).

solenoid lens forms a roughly collimated electron beam which travels towards a freestanding aluminum film with a thickness of approximately 50 nm supported by a 100 lines per inch transmission electron microscopy mesh (inset in Fig. 5.5). The choice of the material for the metal film was influenced by three factors: the electron transmission of the material, its laser damage threshold and the simulated strength of the streaking effect. The present aluminum film has a transmission of approx. 3.5% for electrons at 25 keV. The electron beam has an angle of incidence of 17° and a size of 323 µm by 288 µm (full width at half maximum) at the aluminum film.

The major part of the laser light (up to 48 mW) is focused directly onto the aluminum film (beam waist 44 µm by 68 µm full width at half maximum) under a shallow angle (angle of incidence: 77°). The angles between the laser, the electron beam and the surface of the aluminum film are chosen such that all spots on the foil are hit with the same delay between electron and laser (see Sect. 2.6 for details). We ensure that the laser pulses are temporally compressed to approximately 50 fs (full width at half maximum) at the aluminum film and overlap the laser pulse and the electron pulse on the film both spatially and temporally. In order to maximize the streaking effect, we routinely use a laser polarization in the plane formed by

the laser and the electron beam (parallel polarization). The laser pulses can be attenuated by means of a half-wave plate and a polarizer. A mechanical delay line located in the laser path leading to the electron generation can be used to vary the delay between the electron pulses and the laser pulses.

After the interaction with the laser pulse and the transmission through the aluminum film, the electron pulses propagate towards a home-built time-of-flight spectrometer[4] consisting of a high-voltage drift-tube (40 mm inner diameter, 200 mm length) and a commercial microchannel plate (MCP) detector in combination with a time-to-digital converter unit (Surface Concept GmbH) providing a time resolution of approximately 200 ps (full width at half maximum). The start signal for the time-of-flight measurement is derived from the laser pulses used in the experiment, impinging on a fast photodiode, while the electron pulses hitting the MCP detector provide the stop signal. In order to introduce sufficiently high dispersion to the 25-keV electrons to resolve few-eV energy modulations from the laser's streaking field, the drift-tube's voltage is set to reject electrons with energies less than 5 eV below the central energy of 25 keV. The achieved energy resolution is better than 0.5 eV (full width at half maximum) within ±3 eV around the central energy and better than 1 eV (full width at half maximum) within 13 eV above the central energy.

The spectrometer is calibrated by precisely varying the acceleration voltage at the photocathode (the drift-tube's voltage staying the same) and recording the time-of-flight spectrum of the direct electron beam. The streaking spectra are then calculated from the raw time-of-flight data using the time-to-energy mapping, $t(E)$, and energy-dependent amplitude corrections from the calibration data. Finally, the amplitude is weighted by $\mathrm{d}t(E)/\mathrm{d}E$, in order to account for the nonlinear relation between the sizes of time intervals and corresponding energy intervals.

5.5.2 Results

Figure 5.6 shows energy spectra of the electrons as a function of the delay between the electron pulses and the laser pulses. Negative delays indicate that the electron pulses arrive at the aluminum foil before the laser pulses. In the plot, the spectrum of the electron pulses at a large negative delay and thus without any effect of the laser pulses is subtracted in order to accentuate the changes in the spectrum. The color encodes the increase or decrease of electron counts at a specific energy on a logarithmic scale. In this visualization values between -1 and 1 are plotted as 0. The scaling of the data was chosen such that noise mostly falls into this range. In the proximity of zero delay, where laser pulses and electron pulses overlap temporally, electrons are redistributed from their original energy to higher and lower energies. Up to approximately 17 eV energy gain features are visible that are separated by about 1.6 eV, the laser's photon energy. In the following, we call these features

[4]The time-of-flight spectrometer was developed by Alexander Gliserin.

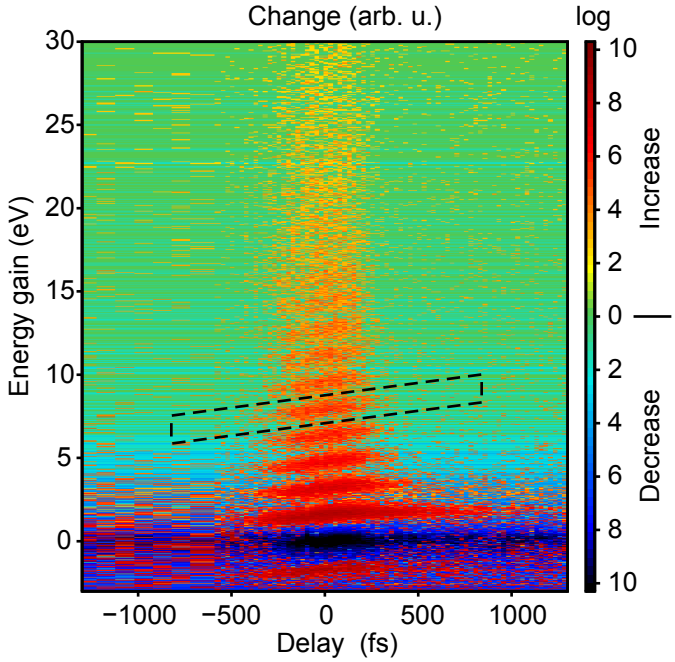

Figure 5.6: Spectrogram of streaked electrons at 25 keV. Electron spectra are plotted as a function of the delay between electron and laser pulses. For clarity, the unstreaked spectrum for a large negative delay is subtracted and the color scale is logarithmic. The dashed line encircles an exemplary region of interest for data analysis.

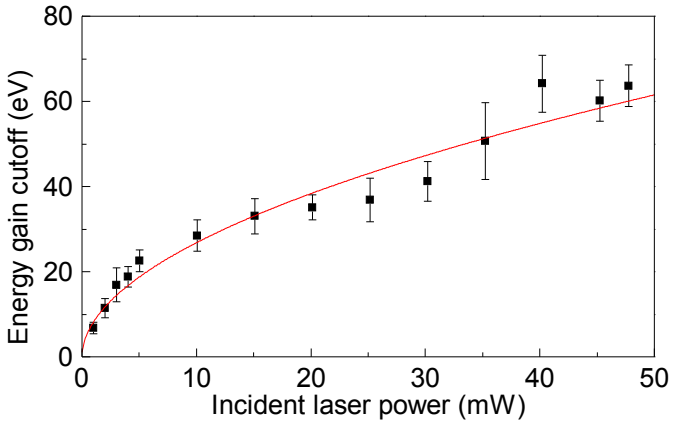

Figure 5.7: Power dependence of the cutoff energy. The maximum energy gain at optimal overlap is plotted for different incident laser powers. The red line is a least-square fit to the data of the form $E_{cutoff} \propto (P_{laser})^a$, yielding an exponent of $a = 0.52 \pm 0.03$. This indicates that the magnitude of the streaking effect is determined by the electric field of the laser.

orders, although their existence does not originate from a multi-photon process. Instead, the features result from the spectral interference within a single electron wavepacket.

As detailed in [148], we expect the electrons forming our pulses to have a temporal coherence greater than approximately 2 fs. Since this time is comparable to the duration of a laser cycle there are several points in time when the electron can leave the laser's field and obtain the same energy gain. Because these quantum pathways are indistinguishable, they interfere and form spectral features separated by the laser's photon energy [149]. The shift in the maxima of the streaking orders as a function of the delay time represents the varying initial energy of the electrons before the interaction with the laser pulse, i.e. the electron pulse's chirp. At higher energy gains, distinct features are no longer visible owing to the limited energy resolution of the detection system in this range. On the energy loss side, just one feature is visible because of our choice of the spectrometer's energy window. For the experimental conditions presented in Fig. 5.6, the highest energy gain extends up to approximately 65 eV. We call this value the cutoff energy.

In Fig. 5.7 we analyze the cutoff energy of the streaked electrons at the point of optimal overlap between laser and electron pulse ($t_d = 0$ fs) for varying incident laser powers. In order to evaluate the power dependence of the cutoff energy we fit a function of the form $E_{cutoff} \propto (P_{laser})^a$ to the experimental data. This results in a value of $a = 0.52 \pm 0.03$, which is in excellent agreement with the exponent 0.5 expected from Eq. (5.1) or the numerical simulation (Sect. 5.4). Indeed, the cutoff

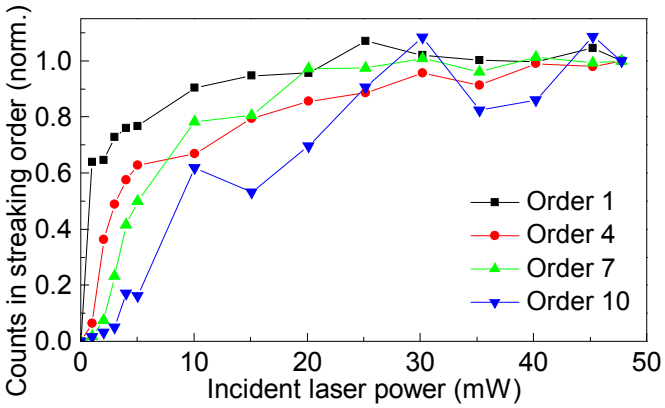

Figure 5.8: Power dependence of the streaking orders. The onset of different streaking orders is shown as a function of the incident laser power at the optimal overlap. Lower orders appear at lower laser powers.

energy scales linearly with the maximum electric field strength of the laser pulses.

In order to calculate the expected cutoff energy of the streaked electron pulses we use Eq. (5.1) and the effective accelerating field $\vec{E}_{eff} = \vec{E} + \vec{v} \times \vec{B}$ as discussed in Sect. 5.2. Taking into account the optical properties of the aluminum film, we find that the directions of $\vec{E}_{eff}$ at the surface of the metal film oscillates. This is due to the phase shift between the incident and the reflected wave. At its greatest magnitude, $\vec{E}_{eff}$ is oriented along the direction of electron trajectory. We thus set $\theta = 0$ in Eq. (5.1). For our experimental parameters, we calculate a maximum accelerating field of $|\vec{E}_{eff}^{max}| = 1.83 \cdot 10^9\,\mathrm{V\,m^{-1}}$ and thus a maximum cutoff energy of 73 eV, which is in good agreement with the experimental findings.

The maximum energy gain determined in the numerical simulation (Sect. 5.4), 77 eV, is about 5 % larger than the value calculated from the classical formula. Considering that Eq. (5.1) is non-relativistic and assumes the instantaneous disappearance of the electron from the field of the laser, thus neglecting the field's penetration into the metal, this discrepancy is not surprising. However, it is small enough to use Eq. (5.1) as a suitable approximation for the observed effect.

Figure 5.8 illustrates how features of different orders behave for increasing incident laser powers. Features with small energy gain appear at lower laser powers than features with higher energy gains consistent with our interpretation of the effect. We note that features with an energy gain of few electronvolts are already detectable for the smallest incident laser power of 1 mW.

Figure 5.9 shows the dependence of the electron cutoff energy on the laser polarization. We varied the polarization of the incident laser pulse using a half-wave plate. Zero degrees correspond to parallel polarization, i.e. polarization in the plane spanned by electron and laser beam. The solid line is a least-square fit to the data

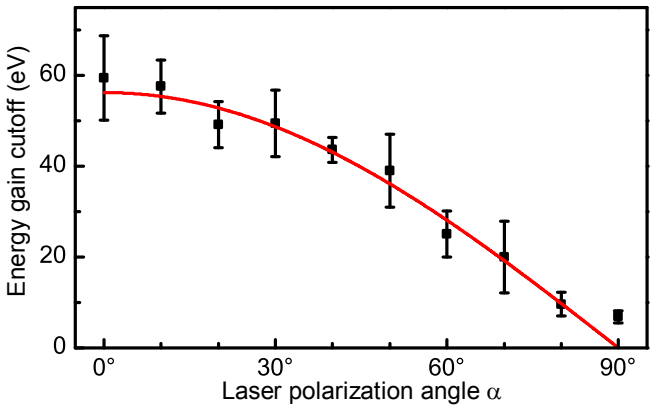

Figure 5.9: Polarization dependence of the cutoff energy. The maximum energy gain at optimal overlap is plotted for different incident laser polarizations. The red line is a cosine least-square fit to the data based on Eq. (5.1).

using a cosine function as expected from Eq. (5.1). We see an energy gain effect even for incident light polarized perpendicularly to the plane spanned by electron and laser beam, which we attribute to imperfections in our polarization optics.

Figure 5.10 displays the temporal behavior of the effect. For the temporal analysis of the streaking effect we select skewed rectangular regions of interest containing single streaking features from the data (see Fig. 5.6) and integrate those along the energy axis. At higher energies where the streaking features are no longer distinguishable, similar regions of interest with edges parallel to the lower energy ones are selected and integrated. This results in temporal profiles of the electron counts for the region of interest. These profiles are fitted with Gaussian functions. The resulting fit values are shown in Fig. 5.10 as a function of the average electron energy in the respective region of interest. The error bars in Fig. 5.10 represent the standard errors of the Gaussian fits.

Each temporal profile represents a cross-correlation between the electron pulse and the laser pulse. Here, the effective laser pulse duration to be taken into account is the time where the envelope of the electric field exceeds the level necessary to generate the energy gain corresponding to the region of interest. Thus, for increasing values of the energy gain, the electron pulse duration is convolved with decreasing effective laser pulse durations. At some electron energy gain, the contribution of the laser pulse duration to the convolved duration of the streaking effect becomes insignificant and the cross-correlation duration no longer depends on the electron's energy gain. Since the electron pulse duration in our experiment is significantly longer than the laser pulse duration we see a fast approach to a stationary value, which corresponds directly to the electron pulse duration. For the data shown in

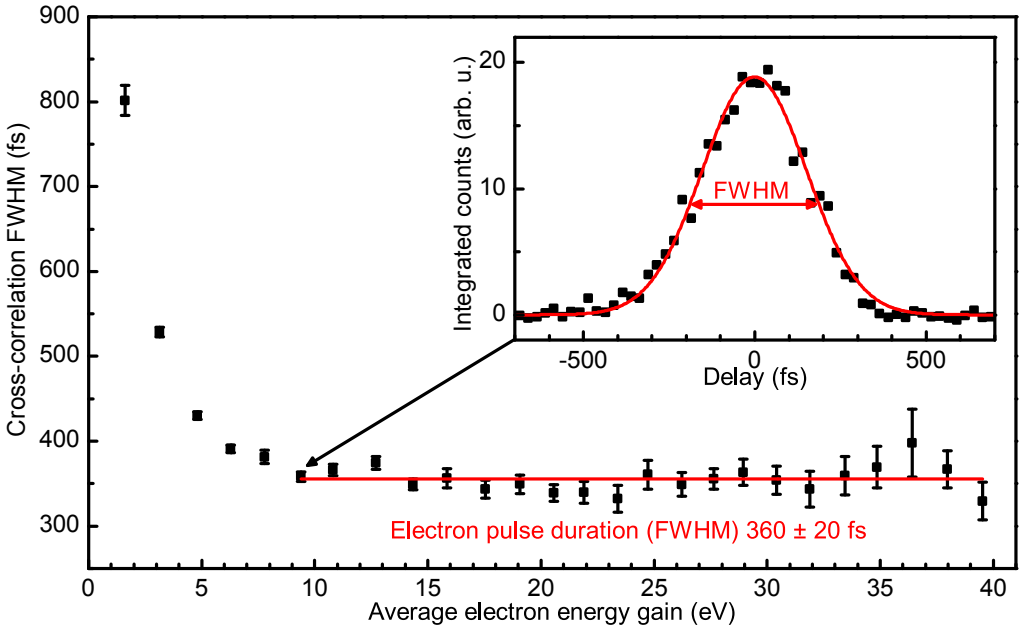

Figure 5.10: Cross-correlation between electron pulse and laser pulse. For each delay step, the electron counts in a certain energy range were integrated (inset). This provides a cross-correlation between the electron pulse and the laser pulse at a certain average energy gain. The cross-correlation signal is fitted with a Gaussian function. The results of these fits are shown in the main figure. The effective laser pulse duration is determined by the duration of the fraction of the laser pulse where the electric field is sufficient to produce the energy gain under consideration. This time decreases with increasing electron energy gain to the point where the effective laser pulse duration no longer contributes and the cross-correlation width approaches the electron pulse duration. This analysis yields an electron pulse duration of (360 ± 20) fs (full width at half maximum, FWHM).

Fig. 5.10, an electron pulse duration of (360 ± 20) fs (full width at half maximum) is retrieved. The electron pulse duration and its uncertainty are obtained as the mean value and the standard deviation of the Gaussian widths after convergence, respectively.

We note that for low energy gains the streaking features become much longer and also asymmetric in time. We attribute this effect to the non-Gaussian spectral profile of our laser pulses which results in significant pre- and after-pulses in the temporal domain with laser field strength sufficient to cause an electron acceleration in this range. The asymmetry of the signal may be attributed to uncorrected third-order dispersion from the prism compressor in our laser system, which typically results in an unsymmetrical temporal profile of the pulse.

In summary, we have shown that the principles of streaking can be extended to the characterization of free electrons at keV energies. The effect behaves similar to the streaking of lower energy electrons and provides a cross-correlation between the laser and electron pulses.

5.6 Application to electron pulse characterization

In the following section we make use of the streaking effect to characterize femtosecond electron pulses for diffraction experiments. The characterization of femtosecond electron pulses is of great interest in the fields of time-resolved electron diffraction and time-resolved electron microscopy. It constitutes a necessary prerequisite for the continuous reduction of electron pulse durations. Previous approaches include techniques based on conventional streak-cameras [134] and deflecting cavities [67]. Field-enhancement in the proximity of nanostructures has also been used to characterize femtosecond electron pulses [150]. Another method that has been proposed is based on the streaking of Auger electrons emitted by the incident electron pulses [149]. Ponderomotive scattering, i. e. the deflection of the electron pulse by the gradient of the intensity profile of a laser pulse, is used widely in the field [57]. Using a standing wave approach it has been implemented with conventional amplified laser systems [58]. However, since it is based on the temporal intensity profile of the laser pulse, its time resolution is limited to the pulse duration of the employed laser pulses.

Here, we demonstrate exemplarily the application of the streaking technique to electron pulse characterization. Being sensitive to the electromagnetic field of the laser pulse, the temporal resolution of this approach is not limited to the pulse duration of the laser pulse. Figure 5.11 shows streaking spectrograms for four different numbers of electrons per pulse. The average number of electrons per pulse was adjusted by changing the intensity of the laser pulses on the photocathode. We quantified this number by taking into account the detector's sensitivity, the electron transmission through the aluminum film, the integration time and the repetition

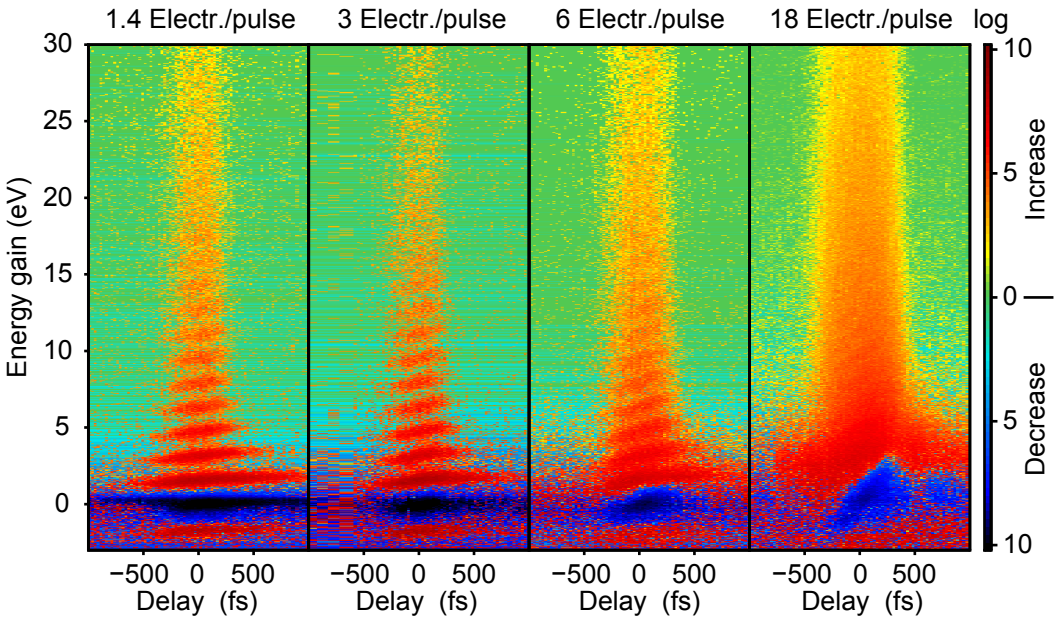

Figure 5.11: Streaking spectrograms for an average of 1.4, 3, 6 and 18 electrons per pulse. The data reflects an increase of pulse duration, chirp and bandwidth as well as a decrease in the visibility of streaking features for increasing electron numbers.

rate of the laser.

Despite their similarity the spectrograms differ in several aspects. Firstly, the electron pulse duration, evaluated as discussed above, increases with the number of electrons per pulse. Secondly, the slope of the streaking features increases with increasing electron densities within the pulse. This is representative of the chirp of the electron pulses, i. e. the correlation between momentum and longitudinal position within the pulse. For example, an electron pulse consisting of many electrons has a certain electron energy distribution due to the generation mechanism [53]. If we consider a beam propagating towards a target, the electrons with higher energies arrive at the target at an earlier time than those with a lower energy. If the time difference between the leading and the trailing electrons is large compared to the pulse duration of the laser pulses generating the electron pulses, the dependency between the electron velocity and the arrival time is linear [54]. In addition, if many electrons form an electron pulse, these electrons will repel each other (space-charge effect). This leads to a further broadening of the electron pulse's temporal profile and of its energy spectrum. The change in the slope of the streaking features in Fig. 5.11 is indicative of this effect.

We analyze the streaking spectrograms in the following way. After selecting skewed regions of interest containing single streaking features we take a lineout along the energy axis for each delay value. This lineout is fitted with a Gaussian function yielding values for the center of the streaking feature and its amplitude for each delay time. Due to the automatic fitting routines, some of these fits do not converge properly and are neglected in the subsequent analysis. We consider the fitted amplitudes as a function of delay time and perform another Gaussian fit to retrieve the electron-laser cross-correlation time. The slope of the streaking features is obtained by fitting a linear function to the fitted center positions as a function of the delay time. The energy bandwidth of the electron pulses is retrieved by multiplying the fitted cross-correlation time with the slope of the streaking feature. Finally, the chirp of the electron pulse is calculated by dividing the energy bandwidth by the electron pulse duration[5].

Thirdly, the visibility of the streaking features decreases with increasing electron numbers. This may be caused by an insufficient experimental resolution for the tilted streaking orders or by a loss in temporal coherence in the electron pulses. Future studies with improved temporal and energy resolutions will allow to answer this question. The results for pulse duration, energy bandwidth and chirp are summarized in Table 5.1.

The experimental results illustrate the detrimental effects of Coulomb repulsion even for low electron numbers per pulse. Although the electron pulse duration changes by less than 10% in the range from 1.4 to 6 electrons per pulse, the energy

[5]We note that this method of determining the chirp of the electron pulses is not completely analogous to the definition of the chirp used in optics.

Average number of electrons	Pulse duration (fs, FWHM)	Energy bandwidth (eV, FWHM)	Electron chirp (eV/ps)
1.4	360 ± 20	0.39 ± 0.06	1.1 ± 0.2
3	370 ± 30	0.58 ± 0.03	1.6 ± 0.2
6	390 ± 20	1.01 ± 0.08	2.6 ± 0.2
18	540 ± 20	2.9 ± 0.2	5.4 ± 0.4

Table 5.1: Summary of electron pulse properties.

bandwidth almost triples. This has profound negative consequences for the coherence properties of the electron pulses. Going from 6 to 18 electrons per pulse, the electron pulse duration increases by approx. 50%. These findings highlight the necessity of working in a genuine single-electron regime in order to achieve the highest coherence and temporal resolution.

5.7 Conclusion and outlook

We have successfully extended the technique of laser streaking to freely propagating electron pulses at an energy of 25 keV. As a first application, electron pulses for ultrafast diffraction experiments were characterized in great detail, revealing not only their pulse duration but also their energy bandwidth and chirp. In addition, interference features in the electron spectra provide some insight into the temporal coherence properties of the electrons.

Considering that both the experimental results and the numerical simulation showed the observed streaking effect is dependent on the electric field of the laser pulse, the temporal resolution relevant to the characterization of electron pulses is not limited by the duration of the laser pulse. Thus, in contrast to all other techniques, laser streaking offers the potential of the characterization of attosecond electron pulses [64]. Consequently, it is one of the enabling technologies for advancing ultrafast electron diffraction towards ever higher temporal resolutions. With electron compression efforts underway in our laboratory [63], it has already proven vital to the temporal compression of electron pulses.

6 Conclusions

Ultrafast electron diffraction provides the tools required for studying structural dynamics in a variety of samples. At the typical energies of tens to hundreds of kiloelectronvolts, electrons have a de Broglie wavelength in the picometer range making them ideally suited for resolving inter-atomic distances. At the same time, electron pulse durations of a few hundred femtoseconds enable studies of many dynamical processes involving the movement of atoms. The capabilities of ultrafast electron diffraction can be expanded significantly, if shorter electron pulses are available. This is why there is a large interest in the electron diffraction community in reducing the electron pulse duration. Simulations suggest that electron diffraction experiments can ultimately be extended to studying the dynamics of electron densities. The required electron pulse durations for these experiments are in the sub-femtosecond range.

Another important parameter is the transverse coherence of the electron pulses. A coherence width larger than the size of the scattering structure, for example a molecule or the unit cell of a crystal, is required to produce a useful diffraction pattern. Current electron diffraction experiments are severely limited in this respect and can only be used to study small unit cells and molecules with sizes below one nanometer.

In the present work, we discuss our progress in exploring and pushing the limits of ultrafast electron diffraction. For this purpose, we implemented a versatile experimental setup that addresses the main difficulties in producing short and coherent electron pulses. These difficulties arise from two fundamental properties of electrons.

Firstly, electrons repel each other. This causes a dense cloud of electrons to expand rapidly. Our approach to circumventing this so-called space-charge effect is to generate electron pulses that contain just a single electron. This eliminates all detrimental effects of Coulomb repulsion between electrons but also reduces the electron flux. In order to compensate for this loss of flux we increased the repetition rate of our diffraction experiment to several MHz. In the single-electron regime, all electron pulse parameters, like pulse duration, velocity and energy distributions, are defined as averages over a large number of single-electron pulses.

Secondly, even in the absence of space charge, electron pulses with a finite energy distribution will expand as they propagate away from their source. This is because electrons with different energies travel at different velocities: Vacuum is dispersive for electrons. This second cause of electron pulse lengthening was also addressed in the present work. The electron energy distribution responsible for the broadening of the electron pulse upon propagation through vacuum is directly influenced by the mismatch between the photon energy and the work function during the photoemission process. Using a tunable source of ultraviolet light pulses, we were able

to show that the widths of the electrons' velocity and energy distributions can be reduced significantly by using a photon energy that is matched to the work function of the cathode material. By optimizing the laser's pulse duration and wavelength with respect to the cathode's work function, electron pulses with a duration below 100 fs can be produced.

In a separate experiment, we studied the coherence properties of our single-electron pulses. A magnetic lens scan was used to determine the transverse velocity spread of the electrons, from which the transverse coherence length of the electrons was calculated. This measurement yielded a transverse coherence length of approximately 20 nm at a beam radius of 77 µm (standard deviation). This result was confirmed by an independent diffraction measurement where high-quality diffraction patterns with very sharp peaks were obtained.

The measured transverse coherence length of our electron pulses represents an improvement of about an order of magnitude over previously reported results. It thus opens up a new range of molecules to be studied by ultrafast electron diffraction, which were previously too large for the limited coherence of the available electron beams.

The large coherence of our electron beam is the consequence of two improvements, the reduced transverse velocity spread of our single-electron pulses due to the absence of space charge and the small source size of the electron beam. Both aspects are directly linked to the single-electron regime. Since the photon energy in the coherence experiment was not perfectly matched to the cathode's work function, the use of tunable ultraviolet light promises a further improvement of the transverse coherence.

In the ultrafast electron diffraction community a lot of attention is focused on reducing the electron pulse duration. However, the tools for characterizing electron pulses do not develop as quickly. The temporal resolution obtained with ponderomotive scattering, currently state of the art, is intrinsically limited to the laser pulse duration. However, current pulse compression techniques involving microwave cavities can compress the electron pulses below the duration of the original laser pulse duration. Consequently, there is a need for an improved pulse characterization technique, ideally with the capability of characterizing the envisioned sub-femtosecond pulses.

In this work, we presented a new approach to the characterization of ultrashort electron pulses. It extends the established techniques of attosecond streaking to freely propagating electron pulses at energies of tens of kiloelectronvolts. The technique is based on the interaction between the electron pulse and a laser pulse at the surface of thin metal film. The electric and magnetic fields of the laser pulse accelerate the electron, but this interaction ends abruptly when the electron leaves these fields at the surface of the metal film which reflects the laser light. The electron is left with an energy shift depending on the relative delay between the laser and the electron pulse.

We showed that the energy gain of the electron is determined by the field of the laser pulse rather than by its intensity envelope. Thus, the laser streaking technique is capable of characterizing electron pulses with a pulse duration below the laser's oscillation period. Consequently, laser streaking of freely propagating electron pulses at tens of kiloelectronvolts will most likely become one of the keys to advancing electron diffraction to temporal resolutions in the few-femtosecond or even sub-femtosecond range.

In addition to the electron pulse duration, information about the bandwidth and the chirp of the electron pulses can be obtained from the laser streaking measurement. We thus applied the newly developed technique to electron pulses with different numbers of electrons per pulse and observed the effects of Coulomb repulsion on the mentioned properties of the electron pulses. This study highlighted once more the importance of working in the single-electron regime for achieving the highest temporal resolutions.

Ultrafast electron diffraction in a transmission geometry requires samples with a thickness of typically tens of nanometers, the production of which is non-trivial. Frequently, samples can only be prepared with a diameter of a few hundred micrometers. In order to find the ideal excitation conditions for the sample in a time-resolved experiment, it is helpful to perform spectroscopic measurements on the sample. For this purpose, a microspectrometer was developed as part of the present work. It provides a spot size below 200 µm (full width at half maximum) in the wavelength range from 215 to 1030 nm. In addition to measurements in a transmission geometry, the microspectrometer can be used for fluorometry and reflectance measurements. It is thus an ideal tool for the characterization of samples for ultrafast electron diffraction.

In the context of the other activities in our group, the results presented here represent important steps towards our common goal of the performing electron diffraction experiments at the highest resolutions. Alexander Gliserin and Matthew Walbran are investigating the compression of electron pulses by means of a microwave cavity. They are also designing new ways of synchronizing the microwave fields to the laser pulses in order to achieve the optimal compression effect. Consequently, their work depends critically on the developed electron pulse characterization. In fact, first streaking experiments with cavity-compressed electron pulses were performed recently with promising results.

On the target side of the experiment, Stefan Lahme and Alexander André have gained a lot of expertise in the preparation and characterization of samples for ultrafast electron diffraction experiments. In this context, they profited very much from the development of the microspectrometer. In addition, Stefan Lahme has made some significant improvements to the electron diffraction apparatus.

While today some of the described activities still take place at individual experimental setups, the goal for the future will be to combine all of the accumulated

knowledge in a single experiment. This experiment will provide well characterized, highly coherent, cavity-compressed single-electron pulses with pulse durations well below 100 fs, which can be used to study a wide variety of samples. This will mark a significant progress towards our ultimate goal of studying electron dynamics in solids in the same way atomic dynamics are studied today.

Bibliography

[1] Bragg, W. L. The structure of some crystals as indicated by their diffraction of x-rays. *Proceedings of the Royal Society of London. Series A, Containing Papers of a Mathematical and Physical Character* **89**, 248–277 (1913).

[2] Watson, J. D. & Crick, F. H. C. Molecular structure of nucleic acids: A structure for deoxyribose nucleic acid. *Nature* **171**, 737–738 (1953).

[3] Wilkins, M. H. F., Stokes, A. R. & Wilson, H. R. Molecular structure of nucleic acids: Molecular structure of deoxypentose nucleic acids. *Nature* **171**, 738–740 (1953).

[4] Franklin, R. E. & Gosling, R. G. Molecular configuration in sodium thymonucleate. *Nature* **171**, 740–741 (1953).

[5] Henderson, R., Baldwin, J., Ceska, T., Zemlin, F., Beckmann, E. & Downing, K. Model for the structure of bacteriorhodopsin based on high-resolution electron cryo-microscopy. *Journal of Molecular Biology* **213**, 899–929 (1990).

[6] Zewail, A. H. 4D ultrafast electron diffraction, crystallography, and microscopy. *Annual Review of Physical Chemistry* **57**, 65–103 (2006).

[7] Sciaini, G. & Miller, R. J. D. Femtosecond electron diffraction: heralding the era of atomically resolved dynamics. *Reports on Progress in Physics* **74**, 096101 (2011).

[8] Zewail, A. H. Femtochemistry: Atomic-scale dynamics of the chemical bond using ultrafast lasers. In Grenthe, I. (ed.) *Nobel Lectures, Chemistry 1996–2000*, 274–367 (World Scientific Publishing Co., Singapore, 2003).

[9] Demtröder, W. *Laser Spectroscopy, Vol. 2: Experimental Techniques* (Springer, Berlin, 2008), 4th edn.

[10] Srinivasan, R., Feenstra, J. S., Park, S. T., Xu, S. & Zewail, A. H. Dark structures in molecular radiationless transitions determined by ultrafast diffraction. *Science* **307**, 558–563 (2005).

[11] Kim, J., Kim, K. H., Lee, J. H. & Ihee, H. Ultrafast x-ray diffraction in liquid, solution and gas: present status and future prospects. *Acta Crystallographica Section A* **66**, 270–280 (2010).

[12] Hada, M., Pichugin, K. & Sciaini, G. Ultrafast structural dynamics with table top femtosecond hard x-ray and electron diffraction setups. *The European Physical Journal Special Topics* **222**, 1093–1123 (2013).

[13] for Structural Bioinformatics, R. C. Protein data bank: Holdings report. `http://www.rcsb.org/pdb/statistics/holdings.do` (2013). [Online; accessed August 20, 2013].

[14] Bargheer, M., Zhavoronkov, N., Woerner, M. & Elsaesser, T. Recent progress in ultrafast x-ray diffraction. *ChemPhysChem* **7**, 783–792 (2006).

[15] Emma, P., Akre, R., Arthur, J., Bionta, R., Bostedt, C., Bozek, J., Brachmann, A., Bucksbaum, P., Coffee, R., Decker, F.-J., Ding, Y. *et al.* First lasing and operation of an ångstrom-wavelength free-electron laser. *Nature Photonics* **4**, 641–647 (2010).

[16] Ishikawa, T., Aoyagi, H., Asaka, T., Asano, Y., Azumi, N., Bizen, T., Ego, H., Fukami, K., Fukui, T., Furukawa, Y., Goto, S. *et al.* A compact x-ray free-electron laser emitting in the sub-ångstrom region. *Nature Photonics* **6**, 540–544 (2012).

[17] Vartanyants, I. A., Singer, A., Mancuso, A. P., Yefanov, O. M., Sakdinawat, A., Liu, Y., Bang, E., Williams, G. J., Cadenazzi, G., Abbey, B., Sinn, H. *et al.* Coherence properties of individual femtosecond pulses of an x-ray free-electron laser. *Physical Review Letters* **107**, 144801 (2011).

[18] Boutet, S., Lomb, L., Williams, G. J., Barends, T. R. M., Aquila, A., Doak, R. B., Weierstall, U., DePonte, D. P., Steinbrener, J., Shoeman, R. L., Messerschmidt, M. *et al.* High-resolution protein structure determination by serial femtosecond crystallography. *Science* **337**, 362–364 (2012).

[19] Bostedt, C., Bozek, J. D., Bucksbaum, P. H., Coffee, R. N., Hastings, J. B., Huang, Z., Lee, R. W., Schorb, S., Corlett, J. N., Denes, P., Emma, P., Falcone, R. W., Schoenlein, R. W., Doumy, G., Kanter, E. P., Kraessig, B., Southworth, S., Young, L., Fang, L., Hoener, M., Berrah, N., Roedig, C. & DiMauro, L. F. Ultra-fast and ultra-intense x-ray sciences: first results from the Linac Coherent Light Source free-electron laser. *Journal of Physics B: Atomic, Molecular and Optical Physics* **46**, 164003 (2013).

[20] Barty, A., Boutet, S., Bogan, M. J., Hau-Riege, S., Marchesini, S., Sokolowski-Tinten, K., Stojanovic, N., Tobey, R., Ehrke, H., Cavalleri, A., Dusterer, S., Frank, M., Bajt, S., Woods, B. W., Seibert, M. M., Hajdu, J., Treusch, R. & Chapman, H. N. Ultrafast single-shot diffraction imaging of nanoscale dynamics. *Nature Photonics* **2**, 415–419 (2008).

[21] Clark, J. N., Beitra, L., Xiong, G., Higginbotham, A., Fritz, D. M., Lemke, H. T., Zhu, D., Chollet, M., Williams, G. J., Messerschmidt, M., Abbey, B., Harder, R. J., Korsunsky, A. M., Wark, J. S. & Robinson, I. K. Ultrafast

three-dimensional imaging of lattice dynamics in individual gold nanocrystals. *Science* **341**, 56–59 (2013).

[22] Sokolowski-Tinten, K., Blome, C., Blums, J., Cavalleri, A., Dietrich, C., Tarasevitch, A., Uschmann, I., Forster, E., Kammler, M., Horn-von Hoegen, M. & von der Linde, D. Femtosecond x-ray measurement of coherent lattice vibrations near the Lindemann stability limit. *Nature* **422**, 287–289 (2003).

[23] Zamponi, F., Rothhardt, P., Stingl, J., Woerner, M. & Elsaesser, T. Ultrafast large-amplitude relocation of electronic charge in ionic crystals. *Proceedings of the National Academy of Sciences* **109**, 5207–5212 (2012).

[24] Chergui, M. & Zewail, A. H. Electron and x-ray methods of ultrafast structural dynamics: Advances and applications. *ChemPhysChem* **10**, 28–43 (2009).

[25] Neutze, R., Wouts, R., van der Spoel, D., Weckert, E. & Hajdu, J. Potential for biomolecular imaging with femtosecond x-ray pulses. *Nature* **406**, 752–757 (2000).

[26] Carbone, F., Musumeci, P., Luiten, O. J. & Hebert, C. A perspective on novel sources of ultrashort electron and x-ray pulses. *Chemical Physics* **392**, 1–9 (2012).

[27] Kong, Q., Lee, J. H., Plech, A., Wulff, M., Ihee, H. & Koch, M. H. J. Ultrafast x-ray solution scattering reveals an unknown reaction intermediate in the photolysis of $[Ru_3(CO)_{12}]$. *Angewandte Chemie International Edition* **47**, 5550–5553 (2008).

[28] Lee, J. H., Kim, J., Cammarata, M., Kong, Q., Kim, K. H., Choi, J., Kim, T. K., Wulff, M. & Ihee, H. Transient x-ray diffraction reveals global and major reaction pathways for the photolysis of iodoform in solution. *Angewandte Chemie International Edition* **47**, 1047–1050 (2008).

[29] Braun, M., Korff Schmising, C. v., Kiel, M., Zhavoronkov, N., Dreyer, J., Bargheer, M., Elsaesser, T., Root, C., Schrader, T. E., Gilch, P., Zinth, W. & Woerner, M. Ultrafast changes of molecular crystal structure induced by dipole solvation. *Physical Review Letters* **98**, 248301 (2007).

[30] Woerner, M., Zamponi, F., Ansari, Z., Dreyer, J., Freyer, B., Premont-Schwarz, M. & Elsaesser, T. Concerted electron and proton transfer in ionic crystals mapped by femtosecond x-ray powder diffraction. *Journal of Chemical Physics* **133**, 064509 (2010).

[31] Rischel, C., Rousse, A., Uschmann, I., Albouy, P.-A., Geindre, J.-P., Audebert, P., Gauthier, J.-C., Froster, E., Martin, J.-L. & Antonetti, A. Femtosecond

time-resolved x-ray diffraction from laser-heated organic films. *Nature* **390**, 490–492 (1997).

[32] Siders, C. W., Cavalleri, A., Sokolowski-Tinten, K., Toth, C., Guo, T., Kammler, M., Hoegen, M. H. v., Wilson, K. R., Linde, D. v. d. & Barty, C. P. J. Detection of nonthermal melting by ultrafast x-ray diffraction. *Science* **286**, 1340–1342 (1999).

[33] Rousse, A., Rischel, C., Fourmaux, S., Uschmann, I., Sebban, S., Grillon, G., Balcou, P., Forster, E., Geindre, J., Audebert, P., Gauthier, J. & Hulin, D. Non-thermal melting in semiconductors measured at femtosecond resolution. *Nature* **410**, 65–68 (2001).

[34] Lindenberg, A. M., Larsson, J., Sokolowski-Tinten, K., Gaffney, K. J., Blome, C., Synnergren, O., Sheppard, J., Caleman, C., MacPhee, A. G., Weinstein, D., Lowney, D. P. *et al.* Atomic-scale visualization of inertial dynamics. *Science* **308**, 392–395 (2005).

[35] Miller, R. J. D., Ernstorfer, R., Harb, M., Gao, M., Hebeisen, C. T., Jean-Ruel, H., Lu, C., Moriena, G. & Sciaini, G. 'Making the molecular movie': first frames. *Acta Crystallographica Section A* **66**, 137–156 (2010).

[36] Orloff, J. (ed.) *Handbook of Charged Particle Optics* (CRC Press, 2008), 2nd edn.

[37] Williamson, J. C., Cao, J. M., Ihee, H., Frey, H. & Zewail, A. H. Clocking transient chemical changes by ultrafast electron diffraction. *Nature* **386**, 159–162 (1997).

[38] Cao, J., Ihee, H. & Zewail, A. H. Ultrafast electron diffraction and direct observation of transient structures in a chemical reaction. *Proceedings of the National Academy of Sciences* **96**, 338–342 (1999).

[39] Ihee, H., Lobastov, V. A., Gomez, U. M., Goodson, B. M., Srinivasan, R., Ruan, C.-Y. & Zewail, A. H. Direct imaging of transient molecular structures with ultrafast diffraction. *Science* **291**, 458–462 (2001).

[40] Ihee, H., Cao, J. & Zewail, A. H. Ultrafast electron diffraction of transient [$Fe(CO)_4$]: Determination of molecular structure and reaction pathway. *Angewandte Chemie International Edition* **40**, 1532–1536 (2001).

[41] Goodson, B. M., Ruan, C.-Y., Lobastov, V. A., Srinivasan, R. & Zewail, A. H. Ultrafast electron diffraction: complex landscapes of molecular structures in thermal and light-mediated reactions. *Chemical Physics Letters* **374**, 417–424 (2003).

[42] Jean-Ruel, H., Cooney, R. R., Gao, M., Lu, C., Kochman, M. A., Morrison, C. A. & Miller, R. J. D. Femtosecond dynamics of the ring closing process of diarylethene: A case study of electrocyclic reactions in photochromic single crystals. *Journal of Physical Chemistry A* **115**, 13158–13168 (2011).

[43] Eichberger, M., Schafer, H., Krumova, M., Beyer, M., Demsar, J., Berger, H., Moriena, G., Sciaini, G. & Miller, R. J. D. Snapshots of cooperative atomic motions in the optical suppression of charge density waves. *Nature* **468**, 799–802 (2010).

[44] Erasmus, N., Eichberger, M., Haupt, K., Boshoff, I., Kassier, G., Birmurske, R., Berger, H., Demsar, J. & Schwoerer, H. Ultrafast dynamics of charge density waves in $4H_b - TaSe_2$ probed by femtosecond electron diffraction. *Physical Review Letters* **109**, 167402 (2012).

[45] Williamson, S., Mourou, G. & Li, J. C. M. Time-resolved laser-induced phase transformation in aluminum. *Physical Review Letters* **52**, 2364 (1984).

[46] Siwick, B. J., Dwyer, J. R., Jordan, R. E. & Miller, R. J. D. An atomic-level view of melting using femtosecond electron diffraction. *Science* **302**, 1382–1385 (2003).

[47] Siwick, B. J., Dwyer, J. R., Jordan, R. E. & Miller, R. Femtosecond electron diffraction studies of strongly driven structural phase transitions. *Chemical Physics* **299**, 285–305 (2004).

[48] Harb, M., Ernstorfer, R., Hebeisen, C. T., Sciaini, G., Peng, W., Dartigalongue, T., Eriksson, M. A., Lagally, M. G., Kruglik, S. G. & Miller, R. J. D. Electronically driven structure changes of Si captured by femtosecond electron diffraction. *Physical Review Letters* **100**, 155504 (2008).

[49] Ernstorfer, R., Harb, M., Hebeisen, C. T., Sciaini, G., Dartigalongue, T. & Miller, R. J. D. The formation of warm dense matter: Experimental evidence for electronic bond hardening in gold. *Science* **323**, 1033–1037 (2009).

[50] Baum, P., Yang, D.-S. & Zewail, A. H. 4D visualization of transitional structures in phase transformations by electron diffraction. *Science* **318**, 788–792 (2007).

[51] Gao, M., Lu, C., Jean-Ruel, H., Liu, L. C., Marx, A., Onda, K., Koshihara, S.-y., Nakano, Y., Shao, X., Hiramatsu, T., Saito, G., Yamochi, H., Cooney, R. R., Moriena, G., Sciaini, G. & Miller, R. J. D. Mapping molecular motions leading to charge delocalization with ultrabright electrons. *Nature* **496**, 343–346 (2013).

[52] Baum, P. & Zewail, A. H. 4D attosecond imaging with free electrons: Diffraction methods and potential applications. *Chemical Physics* **366**, 2–8 (2009).

[53] Aidelsburger, M., Kirchner, F. O., Krausz, F. & Baum, P. Single-electron pulses for ultrafast diffraction. *Proceedings of the National Academy of Sciences* **107**, 19714–19719 (2010).

[54] Siwick, B. J., Dwyer, J. R., Jordan, R. E. & Miller, R. J. D. Ultrafast electron optics: Propagation dynamics of femtosecond electron packets. *Journal of Applied Physics* **92**, 1643 (2002).

[55] van Oudheusden, T., de Jong, E. F., van der Geer, S. B., 't Root, W. P. E. M. O., Luiten, O. J. & Siwick, B. J. Electron source concept for single-shot sub-100 fs electron diffraction in the 100 keV range. *Journal of Applied Physics* **102**, 093501 (2007).

[56] Siwick, B. J., Green, A. A., Hebeisen, C. T. & Miller, R. J. D. Characterization of ultrashort electron pulses by electron-laser pulse cross correlation. *Optics Letters* **30**, 1057–1059 (2005).

[57] Hebeisen, C. T., Ernstorfer, R., Harb, M., Dartigalongue, T., Jordan, R. E. & Dwayne Miller, R. J. Femtosecond electron pulse characterization using laser ponderomotive scattering. *Optics Letters* **31**, 3517–3519 (2006).

[58] Hebeisen, C. T., Sciaini, G., Harb, M., Ernstorfer, R., Dartigalongue, T., Kruglik, S. G. & Miller, R. J. D. Grating enhanced ponderomotive scattering for visualization and full characterization of femtosecond electron pulses. *Optics Express* **16**, 3334–3341 (2008).

[59] Gahlmann, A., Tae Park, S. & Zewail, A. H. Ultrashort electron pulses for diffraction, crystallography and microscopy: theoretical and experimental resolutions. *Physical Chemistry Chemical Physics* **10**, 2894–2909 (2008).

[60] Kassier, G. H., Haupt, K., Erasmus, N., Rohwer, E. G. & Schwoerer, H. Achromatic reflectron compressor design for bright pulses in femtosecond electron diffraction. *Journal of Applied Physics* **105**, 113111 (2009).

[61] Wang, Y. & Gedik, N. Electron pulse compression with a practical reflectron design for ultrafast electron diffraction. *IEEE Journal of Selected Topics in Quantum Electronics* **18**, 140–147 (2012).

[62] Tokita, S., Hashida, M., Inoue, S., Nishoji, T., Otani, K. & Sakabe, S. Single-shot femtosecond electron diffraction with laser-accelerated electrons: Experimental demonstration of electron pulse compression. *Physical Review Letters* **105**, 215004 (2010).

[63] Gliserin, A., Apolonski, A., Krausz, F. & Baum, P. Compression of single-electron pulses with a microwave cavity. *New Journal of Physics* **14**, 073055 (2012).

[64] Fill, E., Veisz, L., Apolonski, A. & Krausz, F. Sub-fs electron pulses for ultrafast electron diffraction. *New Journal of Physics* **8**, 272 (2006).

[65] Veisz, L., Kurkin, G., Chernov, K., Tarnetsky, V., Apolonski, A., Krausz, F. & Fill, E. Hybrid dc–ac electron gun for fs-electron pulse generation. *New Journal of Physics* **9**, 451 (2007).

[66] Gliserin, A., Walbran, M. & Baum, P. Passive optical enhancement of laser-microwave synchronization. *Applied Physics Letters* **103**, 031113 (2013).

[67] van Oudheusden, T., Pasmans, P. L. E. M., van der Geer, S. B., de Loos, M. J., van der Wiel, M. J. & Luiten, O. J. Compression of subrelativistic space-charge-dominated electron bunches for single-shot femtosecond electron diffraction. *Physical Review Letters* **105**, 264801 (2010).

[68] Chatelain, R. P., Morrison, V. R., Godbout, C. & Siwick, B. J. Ultrafast electron diffraction with radio-frequency compressed electron pulses. *Applied Physics Letters* **101**, 081901 (2012).

[69] Gao, M., Jean-Ruel, H., Cooney, R. R., Stampe, J., de Jong, M., Harb, M., Sciaini, G., Moriena, G. & Dwayne Miller, R. J. Full characterization of RF compressed femtosecond electron pulses using ponderomotive scattering. *Optics Express* **20**, 12048–12058 (2012).

[70] Morrison, V. R., Chatelain, R. P., Godbout, C. & Siwick, B. J. Direct optical measurements of the evolving spatio-temporal charge density in ultrashort electron pulses. *Optics Express* **21**, 21–29 (2013).

[71] Itatani, J., Quéré, F., Yudin, G. L., Ivanov, M. Y., Krausz, F. & Corkum, P. B. Attosecond streak camera. *Physical Review Letters* **88**, 173903 (2002).

[72] Ganz, T., Pervak, V., Apolonski, A. & Baum, P. 16 fs, 350 nJ pulses at 5 MHz repetition rate delivered by chirped pulse compression in fibers. *Optics Letters* **36**, 1107–1109 (2011).

[73] Herriott, D. R. & Schulte, H. J. Folded optical delay lines. *Applied Optics* **4**, 883 (1965).

[74] Naumov, S., Fernandez, A., Graf, R., Dombi, P., Krausz, F. & Apolonski, A. Approaching the microjoule frontier with femtosecond laser oscillators. *New Journal of Physics* **7**, 216 (2005).

[75] Humphries, S., Jr. *Principles of Charged Particle Acceleration* (Wiley-Interscience, 1986), 1st edn.

[76] Niedrig, H. *Wellencharakter der Materie*, vol. 3 of *Bergmann-Schaefer, Lehrbuch der Experimentalphysik*, chap. 8, 855–903 (de Gruyter, 1974), 6th edn.

[77] Bergeman, T., Erez, G. & Metcalf, H. J. Magnetostatic trapping fields for neutral atoms. *Physical Review A* **35**, 1535–1546 (1987).

[78] Weninger, C. & Baum, P. Temporal distortions in magnetic lenses. *Ultramicroscopy* **113**, 145–151 (2012).

[79] Aidelsburger, M. *Bandwidth and Duration of Femtosecond Electron Pulses from Photoemission.* Bachelor's thesis, Ludwig-Maximilians-Universität München (2009).

[80] Dowell, D. H. & Schmerge, J. F. Quantum efficiency and thermal emittance of metal photocathodes. *Physical Review Special Topics – Accelerators and Beams* **12**, 074201 (2009).

[81] Wytrykus, D., Centurion, M., Reckenthaeler, P., Krausz, F., Apolonski, A. & Fill, E. Ultrashort pulse electron gun with a MHz repetition rate. *Applied Physics B: Lasers and Optics* **96**, 309–314 (2009).

[82] Bradler, M., Baum, P. & Riedle, E. Femtosecond continuum generation in bulk laser host materials with sub-µJ pump pulses. *Applied Physics B: Lasers and Optics* **97**, 561–574 (2009).

[83] Jiang, X., Berglund, C. N., Bell, A. E. & Mackie, W. A. Photoemission from gold thin films for application in multiphotocathode arrays for electron beam lithography. *Journal of Vacuum Science and Technology B* **16**, 3374–3379 (1998).

[84] Hinterberger, F. *Physik der Teilchenbeschleuniger und Ionenoptik* (Springer, 2008), 2nd edn.

[85] McDonald, K. T. & Russell, D. P. Methods of emittance measurement. In Month, M. & Turner, S. (eds.) *Frontiers of Particle Beams: Observation, Diagnosis and Correction, Proceedings of a Topical Course held by the Joint US-CERN School on Particle Accelerators*, vol. 343 of *Lecture Notes in Physics* (Springer, 1989).

[86] Wiedemann, H. *Particle Accelerator Physics: Basic Principles and Linear Beam Dynamics* (Springer, 1993), 1st edn.

[87] Anderson, S. G., Rosenzweig, J. B., LeSage, G. P. & Crane, J. K. Space-charge effects in high brightness electron beam emittance measurements. *Physical Review Special Topics – Accelerators and Beams* **5**, 014201 (2002).

[88] de Araújo, M. A., Silva, R., de Lima, E., Pereira, D. P. & de Oliveira, P. C. Measurement of Gaussian laser beam radius using the knife-edge technique: improvement on data analysis. *Applied Optics* **48**, 393–396 (2009).

[89] Williamson, J. C. & Zewail, A. H. Ultrafast electron diffraction. Velocity mismatch and temporal resolution in crossed-beam experiments. *Chemical Physics Letters* **209**, 10–16 (1993).

[90] Baum, P. & Zewail, A. H. Breaking resolution limits in ultrafast electron diffraction and microscopy. *Proceedings of the National Academy of Sciences* **103**, 16105–16110 (2006).

[91] Kreier, D. & Baum, P. Avoiding temporal distortions in tilted pulses. *Optics Letters* **37**, 2373–2375 (2012).

[92] Michler, G. H. & Lebek, W. *Ultramikrotomie in der Materialforschung* (Hanser Verlag, München, 2004).

[93] Eichberger, M., Krumova, M., Berger, H. & Demsar, J. Sample preparation methods for femtosecond electron diffraction experiments. *Ultramicroscopy* **127**, 9–13 (2013).

[94] Born, M. & Wolf, E. *Principles of Optics: Electromagnetic Theory of Propagation, Interference and Diffraction of Light* (Pergamon Press, 1970), 4th edn.

[95] Hering, E., Martin, R. & Stohrer, M. *Physik für Ingenieure* (Springer, Berlin, 2012), 11th edn.

[96] Nilsson, P.-O. Determination of optical constants from intensity measurements at normal incidence. *Applied Optics* **7**, 435–442 (1968).

[97] Hazelwood, R. Derivation of optical constants from transmission measurements alone–applied to $MoSe_2$. *Thin Solid Films* **6**, 329–341 (1970).

[98] Poelman, D. & Smet, P. F. Methods for the determination of the optical constants of thin films from single transmission measurements: a critical review. *Journal of Physics D: Applied Physics* **36**, 1850–1857 (2003).

[99] Hoheneder, M. *Spektroskopie ultraschneller Protonenübergänge in molekularen Nanokristallen*. Bachelor's thesis, Technische Universität München (2012).

[100] Karpicz, R., Gulbinas, V., Lewanowicz, A., Macernis, M., Sulskus, J. & Valkunas, L. Relaxation pathways of excited n-(triphenylmethyl)salicylidenimine in solutions. *Journal of Physical Chemistry A* **115**, 1861–1868 (2011).

[101] Zewail, A. H. & Thomas, J. M. *4D Electron Microscopy: Imaging in Space and Time* (Imperial College Press, 2009).

[102] Barwick, B., Park, H. S., Kwon, O.-H., Baskin, J. S. & Zewail, A. H. 4D imaging of transient structures and morphologies in ultrafast electron microscopy. *Science* **322**, 1227–1231 (2008).

[103] Spence, J. C. H. *High-Resolution Electron Microscopy* (Oxford University Press, 2003).

[104] van der Geer, S. B., de Loos, M. J., Vredenbregt, E. J. D. & Luiten, O. J. Ultracold electron source for single-shot, ultrafast electron diffraction. *Microscopy and Microanalysis* **15**, 282–289 (2009).

[105] Mandel, L. & Wolf, E. *Optical coherence and quantum optics* (Cambridge University Press, 2008), 1st edn.

[106] McMorran, B. & Cronin, A. D. Model for partial coherence and wavefront curvature in grating interferometers. *Physical Review A* **78**, 013601 (2008).

[107] Collin, S., Merano, M., Gatri, M., Sonderegger, S., Renucci, P., Ganière, J.-D. & Deveaud, B. Transverse and longitudinal space-charge-induced broadenings of ultrafast electron packets. *Journal of Applied Physics* **98**, 094910 (2005).

[108] Pei, Z. & Berglund, C. N. Angular distribution of photoemission from gold thin films. *Japanese Journal of Applied Physics* **41**, L52–L54 (2002).

[109] Jensen, K. L., Petillo, J. J., Montgomery, E. J., Pan, Z., Feldman, D. W., O'Shea, P. G., Moody, N. A., Cahay, M., Yater, J. E. & Shaw, J. L. Application of a general electron emission equation to surface nonuniformity and current density variation. *Journal of Vacuum Science and Technology B* **26**, 831–837 (2008).

[110] Cho, B., Ichimura, T., Shimizu, R. & Oshima, C. Quantitative evaluation of spatial coherence of the electron beam from low temperature field emitters. *Physical Review Letters* **92**, 246103 (2004).

[111] Damascelli, A. Probing the electronic structure of complex systems by ARPES. *Physica Scripta* **2004**, 61–74 (2004).

[112] Mahan, G. D. Theory of photoemission in simple metals. *Physical Review B* **2**, 4334–4350 (1970).

[113] Bach, R., Pope, D., Liou, S.-H. & Batelaan, H. Controlled double-slit electron diffraction. *New Journal of Physics* **15**, 033018 (2013).

[114] Claessens, B. J., van der Geer, S. B., Taban, G., Vredenbregt, E. J. D. & Luiten, O. J. Ultracold electron source. *Physical Review Letters* **95**, 164801 (2005).

[115] McCulloch, A. J., Sheludko, D. V., Saliba, S. D., Bell, S. C., Junker, M., Nugent, K. A. & Scholten, R. E. Arbitrarily shaped high-coherence electron bunches from cold atoms. *Nature Physics* **7**, 785–788 (2011).

[116] Saliba, S. D., Putkunz, C. T., Sheludko, D. V., McCulloch, A. J., Nugent, K. A. & Scholten, R. E. Spatial coherence of electron bunches extracted from an arbitrarily shaped cold atom electron source. *Optics Express* **20**, 3967–3974 (2012).

[117] Taban, G., Reijnders, M. P., Fleskens, B., van der Geer, S. B., Luiten, O. J. & Vredenbregt, E. J. D. Ultracold electron source for single-shot diffraction studies. *Europhysics Letters* **91**, 46004 (2010).

[118] Reijnders, M. P., Debernardi, N., van der Geer, S. B., Mutsaers, P. H. A., Vredenbregt, E. J. D. & Luiten, O. J. Phase-space manipulation of ultracold ion bunches with time-dependent fields. *Physical Review Letters* **105**, 034802 (2010).

[119] McCulloch, A. J., Sheludko, D. V., Junker, M. & Scholten, R. E. High-coherence picosecond electron bunches from cold atoms. *Nature Communications* **4**, 1692 (2013).

[120] Engelen, W. J., van der Heijden, M. A., Bakker, D. J., Vredenbregt, E. J. D. & Luiten, O. J. High-coherence electron bunches produced by femtosecond photoionization. *Nature Communications* **4**, 1693 (2013).

[121] Limborg-Deprey, C. & Bolton, P. R. Optimum electron distributions for space charge dominated beams in photoinjectors. *Nuclear Instruments and Methods in Physics Research Section A* **557**, 106–116 (2006).

[122] Luiten, O. J., van der Geer, S. B., de Loos, M. J., Kiewiet, F. B. & van der Wiel, M. J. How to realize uniform three-dimensional ellipsoidal electron bunches. *Physical Review Letters* **93**, 094802 (2004).

[123] Musumeci, P., Moody, J. T., England, R. J., Rosenzweig, J. B. & Tran, T. Experimental generation and characterization of uniformly filled ellipsoidal electron-beam distributions. *Physical Review Letters* **100**, 244801 (2008).

[124] Yang, D.-S., Mohammed, O. F. & Zewail, A. H. Scanning ultrafast electron microscopy. *Proceedings of the National Academy of Sciences* **107**, 14993–14998 (2010).

[125] Paarmann, A., Gulde, M., Müller, M., Schäfer, S., Schweda, S., Maiti, M., Xu, C., Hohage, T., Schenk, F., Ropers, C. & Ernstorfer, R. Coherent femtosecond low-energy single-electron pulses for time-resolved diffraction and imaging: A numerical study. *Journal of Applied Physics* **112**, 113109 (2012).

[126] Hommelhoff, P., Sortais, Y., Aghajani-Talesh, A. & Kasevich, M. A. Field emission tip as a nanometer source of free electron femtosecond pulses. *Physical Review Letters* **96**, 077401 (2006).

[127] Barwick, B., Corder, C., Strohaber, J., Chandler-Smith, N., Uiterwaal, C. & Batelaan, H. Laser-induced ultrafast electron emission from a field emission tip. *New Journal of Physics* **9**, 142 (2007).

[128] Ropers, C., Solli, D. R., Schulz, C. P., Lienau, C. & Elsaesser, T. Localized multiphoton emission of femtosecond electron pulses from metal nanotips. *Physical Review Letters* **98**, 043907 (2007).

[129] Chang, C.-C., Kuo, H.-S., Hwang, I.-S. & Tsong, T. T. A fully coherent electron beam from a noble-metal covered W(111) single-atom emitter. *Nanotechnology* **20**, 115401 (2009).

[130] Bradley, D., Liddy, B. & Sleat, W. Direct linear measurement of ultrashort light pulses with a picosecond streak camera. *Optics Communications* **2**, 391–395 (1971).

[131] Schelev, M. Y., Richardson, M. C. & Alcock, A. J. Image-converter streak camera with picosecond resolution. *Applied Physics Letters* **18**, 354–357 (1971).

[132] Ito, T., Hiramatsu, M., Hosoda, M. & Tsuchiya, Y. Picosecond time-resolved absorption spectrometer using a streak camera. *Review of Scientific Instruments* **62**, 1415–1419 (1991).

[133] Owaki, S. Time structure monitoring of the electron beam in a linear accelerator. *Japanese Journal of Applied Physics* **22**, 723–727 (1983).

[134] Watanabe, T., Uesaka, M., Sugahara, J., Ueda, T., Yoshii, K., Shibata, Y., Sakai, F., Kondo, S., Kando, M., Kotaki, H. & Nakajima, K. Subpicosecond electron single-beam diagnostics by a coherent transition radiation interferometer and a streak camera. *Nuclear Instruments and Methods in Physics Research Section A* **437**, 1–11 (1999).

[135] Paul, P. M., Toma, E. S., Breger, P., Mullot, G., Augé, F., Balcou, P., Muller, H. G. & Agostini, P. Observation of a train of attosecond pulses from high harmonic generation. *Science* **292**, 1689–1692 (2001).

[136] Drescher, M., Hentschel, M., Kienberger, R., Tempea, G., Spielmann, C., Reider, G. A., Corkum, P. B. & Krausz, F. X-ray pulses approaching the attosecond frontier. *Science* **291**, 1923–1927 (2001).

[137] Hentschel, M., Kienberger, R., Spielmann, C., Reider, G. A., Milosevic, N., Brabec, T., Corkum, P., Heinzmann, U., Drescher, M. & Krausz, F. Attosecond metrology. *Nature* **414**, 509–513 (2001).

[138] Brabec, T. & Krausz, F. Intense few-cycle laser fields: Frontiers of nonlinear optics. *Reviews of Modern Physics* **72**, 545–591 (2000).

[139] Kienberger, R., Goulielmakis, E., Uiberacker, M., Baltuska, A., Yakovlev, V., Bammer, F., Scrinzi, A., Westerwalbesloh, T., Kleineberg, U., Heinzmann, U., Drescher, M. & Krausz, F. Atomic transient recorder. *Nature* **427**, 817–821 (2004).

[140] Krausz, F. & Ivanov, M. Attosecond physics. *Reviews of Modern Physics* **81**, 163–234 (2009).

[141] Gagnon, J., Goulielmakis, E. & Yakovlev, V. The accurate FROG characterization of attosecond pulses from streaking measurements. *Applied Physics B: Lasers and Optics* **92**, 25–32 (2008).

[142] Drescher, M., Hentschel, M., Kienberger, R., Uiberacker, M., Yakovlev, V., Scrinzi, A., Westerwalbesloh, T., Kleineberg, U., Heinzmann, U. & Krausz, F. Time-resolved atomic inner-shell spectroscopy. *Nature* **419**, 803–807 (2002).

[143] Neppl, S., Ernstorfer, R., Bothschafter, E. M., Cavalieri, A. L., Menzel, D., Barth, J. V., Krausz, F., Kienberger, R. & Feulner, P. Attosecond time-resolved photoemission from core and valence states of magnesium. *Physical Review Letters* **109**, 087401 (2012).

[144] Fowles, G. R. *Introduction to Modern Optics* (Dover Publications, 1989), 2nd edn.

[145] Rakić, A. D., Djurišić, A. B., Elazar, J. M. & Majewski, M. L. Optical properties of metallic films for vertical-cavity optoelectronic devices. *Applied Optics* **37**, 5271–5283 (1998).

[146] Press, W. H., Flannery, B. P., Teukolsky, S. A. & Vetterling, W. T. *Numerical Recipes in C: The Art of Scientific Computing* (Cambridge University Press, 1992), 2nd edn.

[147] Porras, M. A. Ultrashort pulsed Gaussian light beams. *Physical Review E* **58**, 1086–1093 (1998).

[148] Baum, P. On the physics of ultrashort single-electron pulses for time-resolved microscopy and diffraction. *Chemical Physics* **423**, 55–61 (2013).

[149] Reckenthaeler, P., Centurion, M., Yakovlev, V. S., Lezius, M., Krausz, F. & Fill, E. E. Proposed method for measuring the duration of electron pulses by attosecond streaking. *Physical Review A (Atomic, Molecular, and Optical Physics)* **77**, 042902 (2008).

[150] Park, S. T., Lin, M. M. & Zewail, A. H. Photon-induced near-field electron microscopy (PINEM): theoretical and experimental. *New Journal of Physics* **12**, 123028 (2010).

Data archiving

The raw data presented in this thesis as well as the associated evaluation tools are stored on the data archive server of the Laboratory for Attosecond Physics at the Max-Planck-Institute of Quantum Optics. This also includes the LaTeX source code and all figures of the thesis. The figures are included as PDF-Files that can be edited in Adobe Illustrator CS4. Some diagrams were directly exported from OriginLab Origin 9, some were generated in MathWorks MATLAB 2010a and edited in Illustrator. Most (if not all) figures received a final edit in Illustrator (fonts, size, etc.). In addition to MATLAB, Wolfram Mathematica 9 was used for some of the calculations/simulations. National Instruments LabVIEW was used for data acquisition and some data analysis.

Chapter 1

Figure 1.1

Caption: Ultrafast electron diffraction, schematic
File: UED_schematic.pdf

Figure 1.2

Caption: Broadening of single-electron pulses
File: single_electron_broadening.pdf

Figure 1.3

Caption: Electron pulse compression, schematic
File: pulse_compression.pdf

Chapter 2

Figure 2.1

Caption: Femtosource XL, schematic
File: Femtosource_XL.pdf

Figure 2.2

Caption: Femtosource XL, spectrum and autocorrelation
Files: femtosourceXL_spectrum.pdf, FemtosourceXL_autocorrelation.pdf
Source data: femtosourceXL/
Notes: Spectral data (110218ls01.txt) and autocorrelation data aquired with Femtolasers Femtometer (ac.dat) were plotted using Origin (Plots.opj).

Figure 2.3

Caption: Electron gun, mechanical design and electric field distribution
File: source_efield.pdf
Source data: source_efield/
Notes: The electric field distribution was calculated using COMSOL Multiphysics (egun_UED1.mph). A plot of the electric field distribution (field30kV.PNG) and a drawing of the mechanical design (Mechanics_scaled.pdf) were overlaid in Illustrator to produce the final figure.

Figure 2.4

Caption: Focusing on the photocathode
File: source_focussing_schematic.pdf

Figure 2.5

Caption: Focus optimization on the photocathode
File: source_focussing_waist.pdf
Source data: source_focussing/
Notes: The beam propagation was calculated in MATLAB using ABCD-matrices and Gaussian beams (focussing.m). The resulting data files (data266nm.txt, data286nm.txt) were plotted using Origin (Pretty_plot_thesis.opj).

Figure 2.6

Caption: Magnetic field of a solenoid
File: solenoid_schematic.pdf

Figure 2.7

Caption: Magnetic lens and deflection coils
File: magnetic_lens_assembly.pdf

Figure 2.8

Caption: Laser beam path for sample excitation
File: excitation_setup.pdf

Figure 2.9

Caption: Point spread function of the CMOS detector
File: detector_PSF.pdf
Source data: detector_PSF/

Notes: Tietz Video and Image Processing Systems GmbH provided a plot of the measured PSF of a detector very similar to the one used for the presented experiments (PSF_40kV_Baum.pdf). The extracted graphics file (PSF_40kV_Baum.TIF) was converted into a list of data values (extracted_data_(scanIt).txt) using the program ScanIt (executable included with the source data). This data was then analyzed and plotted in Origin (PSF_fit.opj).

Figure 2.10

Caption: Deconvolution error, point spread function
File: deconvolution_error.pdf
Source data: detector_PSF/
Notes: A numerical experiment was performed as described in the text. Mathematica was used for this purpose (PSF_numerical_experiment.nb). Using this program, the different values shown in Figure 2.10 were calculated. They were collected and plotted in Origin (deconvolution_error_numerical_experiment.opj).

Figure 2.11

Caption: Generation of tunable ultraviolet laser pulses
File: tunable_UV.pdf

Figure 2.12

Caption: Tunable laser pulses in the ultraviolet spectral range
File: tunable_UV_spectrum.pdf
Source data: tunable_UV_spectrum/
Notes: The original data has been archived with the cited article. The figure was adapted for this work in Origin (tunable_UV.opj).

Figure 2.13

Caption: Electron generation with tunable ultraviolet pulses
File: tunable_UV_beam.pdf
Source data: tunable_UV_beam/
Notes: The original data has been archived with the cited article. The figure was adapted for this work in Origin (tunable_UV_beam.opj).

Figure 2.14

Caption: Defocusing effect of anode hole
File: Anode_hole.pdf

Figure 2.15

Caption: Electron beam profile and Gaussian fit
Files: UEDBeamProfile_data_1000mA.pdf, UEDBeamProfile_fit_1000mA.pdf, UEDBeamProfile_diff_1000mA.pdf
Source data: UEDBeamProfile/
Notes: The raw data file from the UED apparatus (I-1000mA.img) was processed with the MATLAB program readData2_V2.m. The resulting files UEDBeamProfile_data_1000mA.mat, UEDBeamProfile_fit_1000mA.mat and UEDBeamProfile_diff_1000mA.mat were plotted using the MATLAB *.m scripts of the same names.

Figure 2.16

Caption: Magnetic lens scan of the electron beam
File: magn_lens_scan_font_fixed.pdf
Source data: magn_lens_scan/
Notes: The data was plotted and fitted in Origin (magn_lens_scan.opj). For details of the data analysis refer to the archived data for Chapter 4.

Figure 2.17

Caption: Determination of overlap between laser pulse and electron pulse
File: time_zero_beam.pdf
Source data: time_zero/
Notes: The raw image data from the electron detector (not stored) was analyzed using the UED Evaluation Tools (LabVIEW). The reference image with the largest negative delay was subtracted from the subsequent images and the resulting images were assembled in Illustrator.

Figure 2.18

Caption: Determination of temporal overlap
File: time_zero.pdf
Source data: time_zero/
Notes: The processed raw data from Figure 2.17 was further analyzed using the UED Evaluation Tools: the squares of the pixel values in the difference images were summed (Absolute_difference_data.lvm) and the result was plotted in Origin (time_zero.opj).

Figure 2.19

Caption: Velocity matching between laser pulse and electron pulse
File: velocity_matching.pdf

Chapter 3

Figure 3.1

Caption: Microspectrometer, schematic
File: microspectrometer_setup2.pdf

Figure 3.2

Caption: Spectrum of deuterium tungsten halogen lamp
Source data: microspectrometer_lamp_spectrum/
Notes: Spectral data (13000.txt) from the knife-edge measurement (Fig. 3.4) was plotted in Origin (microspectrometer_lamp_spectrum.opj).

Figure 3.3

Caption: Focal spot of the microspectrometer
File: microspectrometer_focus_spot.pdf
Source data: microspectrometer_focus_spot/
Notes: Data from the beam camera was plotted using two MATLAB *.m scripts. See info.txt for details.

Figure 3.4

Caption: Knife-edge characterization
Files: microspectrometer_knifeedge_horizontal.pdf, microspectrometer_knife-edge_vertical.pdf
Source data: microspectrometer_knifeedge/
Notes: The spectral data for each knife-edge position was recorded. Analysis was performed using MATLAB (analysis.m) and the plots were also created using MATLAB (prettyPlot.m). See info.txt for details.

Figure 3.5

Caption: Interference effects at a thin film
File: microspectrometer_film_transmission.pdf

Figure 3.6

Caption: Transmission spectra of resin thin films
File: microspectrometer_resin_transmission.pdf
Source data: microspectrometer_resin_transmission/
Notes: The spectral data (*.dat) was fitted using a MATLAB script (thinFilm.m).

Figure 3.7

Caption: Fitted refractive index of resin
File: microspectrometer_resin_refractive_index.pdf
Notes: See Fig. 3.6 for information on source data and processing.

Figure 3.8

Caption: Fluorescence spectrum
File: microspectrometer_fluorescence.pdf
Source data: microspectrometer_fluorescence/
Notes: Spectral data was plotted using Origin (microspectrometer_fluorescence.opj).

Chapter 4

The source data on which this chapter is based has been archived in the context of the following article:
F. O. Kirchner, S. Lahme, F. Krausz and P. Baum:
Coherence of femtosecond single electrons exceeds biomolecular dimensions.
New Journal of Physics, **15**, 063021 (2013).

Figure 4.1

Caption: Experimental setup of the coherence experiment
File: coherence_setup.pdf

Figure 4.2

Caption: Global degree of coherence
File: coherence_global_degree.pdf

Figure 4.3

Caption: Magnetic lens scan
File: coherence_magn_lens_scan_font_fixed.pdf
Source data: coherence_magn_lens_scan/
Notes: Data was plotted using Origin (B-scan.opj).

Figure 4.4

Caption: Electron beam propagation
File: coherence_beam_propagation_font_fixed.pdf
Source data: coherence_beam_propagation/
Notes: Data was plotted using Origin (beams.opj).

Figure 4.5

Caption: Diffraction sample: N-(triphenylmethyl)-salicylidenimine
Files: coherence_MS1.pdf, coherence_mesh.pdf

Figure 4.6

Caption: Diffraction image from N-(triphenylmethyl)-salicylidenimine
File: coherence_diffraction.pdf

Chapter 5

The source data on which this chapter is based has been archived in the context of the following article:
F. O. Kirchner, A. Gliserin, F. Krausz and P. Baum:
Laser streaking of free electrons at 25 keV.
Nature Photonics, **8**, 52 (2014)

Figure 5.1

Caption: Orientation of $\vec{E}$-,$\vec{H}$- and $\vec{k}$-vectors at an interface
Files: surface_p-pol.pdf, surface_s-pol.pdf

Figure 5.2

Caption: Light at an interface between vacuum and an absorbing medium
File: surface_complex.pdf

Figure 5.3

Caption: Step-size dependence of simulation results
File: simulation_tau.pdf
Source data: simulation_tau/
Notes: The simulation results for different step sizes at a fixed delay time were plotted in Origin (streaking_simulation_rela_tau.opj).

Figure 5.4

Caption: Result of the simulation
File: simulation_streaking.pdf
Source data: simulation_streaking/
Notes: The numerical simulation was performed in MATLAB using a Runge-Kutta method. See info.txt for details.

Figure 5.5

Caption: Streaking experiment, experimental setup
File: streaking_setup.pdf

Figure 5.6

Caption: Spectrogram of streaked electrons at 25 keV
File: streaking_spectrogram.pdf

Figure 5.7

Caption: Power dependence of the cutoff energy
File: streaking_cutoff_power.pdf
Source data: streaking_cutoff_power/
Notes: Data was plotted using Origin (cutoff_analysis_matlab.opj).

Figure 5.8

Caption: Power dependence of the streaking orders
File: streaking_onset_power.pdf
Source data: streaking_onset_power/
Notes: Data was plotted using Origin (order_analysis_matlab.opj).

Figure 5.9

Caption: Polarization dependence of the cutoff energy
File: streaking_cutoff_polarization.pdf
Source data: streaking_cutoff_polarization/
Notes: Data was plotted using Origin (cutoff_analysis.opj).

Figure 5.10

Caption: Cross-correlation between electron pulse and laser pulse
File: streaking_pulse_width.pdf
Source data: streaking_pulse_width/
Notes: Data was plotted using Origin (Columnwise_integration_analysis.opj).

Figure 5.11

Caption: Streaking spectrograms for different numbers of electrons per pulse
File: streaking_electron_number.pdf

Acknowledgments

This work has only become possible because I received support from a lot of individuals. First of all, I would like to thank my supervisor, Prof. Dr. Ferenc Krausz, for giving me the opportunity to join his group and to work in a great team. Thank you for the fruitful and interesting discussions and giving us the freedom to pursue our projects. Likewise, I would like to thank Dr. Peter Baum who leads the electron diffraction activities at Coulombwall 1. Many thanks for your supervision, the countless discussions and the motivation you provided with your many creative ideas. I enjoyed learning from you and building on your experience. I would also like to thank the International Max Planck Research School for providing an interesting, interdisciplinary environment and broadening my field of view. I am particularly indebted to Monika Wild for making a lot of things possible and for giving me a good start in Munich.

Among my immediate colleagues, I am particularly grateful to Stefan Lahme. You have been an excellent partner for bouncing ideas back and forth during the creative processes involved in our work. We shared a lot of fun and frustration in the lab and in our office. Many thanks for all your help with work-related and non-work-related things.

Thank you, Monika Aidelsburger, for your great work on the generation of electrons with tunable ultraviolet light. Thank you, Alexander Gliserin, for our productive work on the streaking experiment and your help with Labview and electronics.

Some of my colleagues have also become great partners for all kinds of trips to the mountains. I am grateful for the many awesome hours we spent together. It has been a great pleasure to be on tour with Marina Hoheneder, Daniel Kreier, Fabian Lücking, Thomas Ganz, Nikolai Lilienfein and Alexander André. Thank you all for the good times at work and especially away from the lab. I miss being in the great outdoors with you!

My sincere thanks go to Dagmar Frischke, who provided countless samples for this work and performed the tedious work of mounting the metal films onto the transmission electron microscopy meshes. This work would not have been possible without you.

I would also like to thank Rolf Oehm for patiently discussing mechanical designs with me. You were a great help in the process of going from an idea to something that could actually be manufactured. Likewise, I am grateful to the whole team of the mechanical workshop for all their help, which was often informal and on short notice.

Michael Krüger did a lot of the proof-reading of the manuscript. Thank you so much for taking over this work on such a short notice. You have been a real blessing for me!

Last but not least, I am thankful for the support and love of my family. Thank you for your trust and the space you left me when I needed it.

This work would not have been possible without the support of my wife. Sandra, thank you so much for your help and patience particularly in the final months of my work. Thanks to all your hard work, I could concentrate fully on writing this thesis. I thank you for bearing with me!

Finally, my thanks go to my Heavenly Father. I thank you for always being there and never letting go.

Scientific publications

F. O. Kirchner, A. Gliserin, F. Krausz and P. Baum:
Laser streaking of free electrons at 25 keV.
Nature Photonics, **8**, 52 (2014)

F. O. Kirchner, S. Lahme, F. Krausz and P. Baum:
Coherence of femtosecond single electrons exceeds biomolecular dimensions.
New Journal of Physics, **15**, 063021 (2013)

M. Aidelsburger, F. O. Kirchner, F. Krausz and P. Baum:
Single-electron pulses for ultrafast diffraction.
Proceedings of the National Academy of Sciences, **107**, 19714 (2010)